

REPORT DOCUMENTATION PAGE					Form Approved OMB No. 0704-0188	
<p>The public reporting burden for this collection of information is estimated to average 1 hour per response, including the time for reviewing instructions, searching existing data sources, gathering and maintaining the data needed, and completing and reviewing the collection of information. Send comments regarding this burden estimate or any other aspect of this collection of information, including suggestions for reducing the burden, to the Department of Defense, Executive Service Directorate (0704-0188). Respondents should be aware that notwithstanding any other provision of law, no person shall be subject to any penalty for failing to comply with a collection of information if it does not display a currently valid OMB control number.</p> <p>PLEASE DO NOT RETURN YOUR FORM TO THE ABOVE ORGANIZATION.</p>						
1. REPORT DATE (DD-MM-YYYY) 10-2013		2. REPORT TYPE Final		3. DATES COVERED (From - To) June 2010-March 2013		
4. TITLE AND SUBTITLE Size and Composition Optimized Nanocatalysts for Propulsion Applications				5a. CONTRACT NUMBER		
				5b. GRANT NUMBER FA9550-08-1-0309		
				5c. PROGRAM ELEMENT NUMBER		
6. AUTHOR(S) Pfefferle, L. D. Maria Flytzani-Stephanopoulos, ChBE, Tufts University Raymond Gorte, ChE, University of Pennsylvania Gary Haller, Chem/ChE, Yale University Charles McEnally, ChE, Yale University Matthew Neurock, ChE, University of Virginia				5d. PROJECT NUMBER		
				5e. TASK NUMBER		
				5f. WORK UNIT NUMBER		
7. PERFORMING ORGANIZATION NAME(S) AND ADDRESS(ES) Department of Chemical Engineering, Yale University Mason Laboratory				8. PERFORMING ORGANIZATION REPORT NUMBER		
9. SPONSORING/MONITORING AGENCY NAME(S) AND ADDRESS(ES) Michael Berman Air Force Office of Scientific Research				10. SPONSOR/MONITOR'S ACRONYM(S) AFOSR		
				11. SPONSOR/MONITOR'S REPORT NUMBER(S)		
12. DISTRIBUTION/AVAILABILITY STATEMENT Approved for public release, Distribution is unlimited						
13. SUPPLEMENTARY NOTES						
14. ABSTRACT <p>In this research we have developed 5 different catalyst formats capable of accelerating the rate of combustion cracking, oxidation and dehydrogenation reactions of jet type fuels. These include: 1) metal nanoclusters covered with a porous nano-oxide; 2) a nanometallic layer on an oxide nanocluster; 3) metal decorated nanoscale oxide shapes; 4) acid functional groups on MWNT; 5) size-selected sub-nanometer size catalyst clusters on carbon-based supports. The practical catalyst formats can be made fuel soluble and most do not use precious metal components. A major accomplishment of this project is our linking the behavior of the model catalyst formats (size selected metal clusters on various substrates) with the practical catalyst analogs. The practical catalyst work was complemented by detailed theoretical and experimental studies on the reactivity of size-selected clusters including studies of support interactions. The links between theory, model catalyst and real catalyst tests are designed to provide a fundamental understanding to aid in the design of active and stable catalysts.</p>						
15. SUBJECT TERMS fuel soluble catalyst, nanomaterial, size selected cluster, molecular modeling						
16. SECURITY CLASSIFICATION OF:			17. LIMITATION OF ABSTRACT	18. NUMBER OF PAGES	19a. NAME OF RESPONSIBLE PERSON	
a. REPORT	b. ABSTRACT	c. THIS PAGE			Lisa D. Pfefferle	
U	U	U	UU	88	19b. TELEPHONE NUMBER (Include area code) 203-432-4377	

Final Report

Grant/Contract Title: (MURI 08) – NANOCATALYSTS FOR PROPULSION APPLICATIONS

Grant/Contract Number; FA9550-08-1-0309

Size and Composition Optimized Nanocatalysts for Propulsion Applications

Lead PI Lisa Pfefferle, Yale University, Department of Chemical and Environmental Engineering
9 Hillhouse Ave.

New Haven, CT

lisa.pfefferle@yale.edu

(203)-432-4377

Co-PIs:

Maria Flytzani-Stephanopoulos, ChBE, Tufts University

Raymond Gorte, ChE, University of Pennsylvania

Gary Haller, Chem/ChE, Yale University

Charles McEnally, ChE, Yale University

Matthew Neurock, ChE, University of Virginia

Stefan Vajda, Adjunct Professor, ChE, Yale University, (Argonne National Laboratory)

Final Project Report

I. Summary

In this research we have developed 5 different catalyst formats capable of accelerating the rate of combustion cracking, oxidation and dehydrogenation reactions including:

- 1) metal nanoclusters covered with a porous nano-oxide;
- 2) a nanometallic layer on an oxide nanocluster;
- 3) metal decorated nanoscale oxide shapes;
- 4) acid functional groups on MWNT;
- 5) size-selected sub-nanometer catalyst clusters on carbon-based supports.

All of these catalyst formats can be made fuel soluble and most do not use precious metal components.

A major accomplishment of this project is linking the behavior of the model catalyst format (size selected metal clusters on various substrates) with the practical catalyst analogs. This is illustrated most clearly in the papers such as Tyo et al. ACS Nano and the paper given in Appendix I and is very rare in the literature.

Our approach has been highly integrative between team members with catalyst fabrication and testing between labs. Dispersions of MWNT supported Co and Pt nanocatalysts, and soluble cobalt oxide nanoparticles have been functionalized and all remain dispersed for months. We have also developed several soluble catalyst formats that do *not use precious metal components*. These are based on sulfated zirconia and nano- Co, Ni and zirconia.

A list of major accomplishments is given below. A short summary of recent accomplishments follows here. First we characterized the covalent bonding between zirconia and a MWNT in a new cracking catalyst that is active at low temperatures. Theoretical calculations confirm the EXAFS results, which indicate that the ZrO_2 clusters form strong Zr-O-C bonds that anchor the nanoparticles of ZrO_2 to the surfaces of the carbon nanotube. Second we showed how pre-reaction of the fuel accelerates combustion. Third we showed that 1 nm and under cobalt oxide particles are not reduced beyond CoO even under extremely reducing conditions. Forth, we characterized both for real and model size selected catalysts of Pt on MWNT how catalyst size affects reactivity. The theoretical results are consistent with experimental findings.

We have used theory and simulation in order to examine the activation and conversion of propane and cyclohexane over: 1) Pt and Co metal clusters, 2) Pt and Co metal clusters supported on carbon nanotubes and 3) a bare cobalt oxide surface. We examine in detail the elementary steps involved in the dehydrogenation of propane to propylene and cyclohexane to cyclohexene. The initial C-H bond activation and removal of aromatic products were found to be rate-controlling steps. We use the initial C-H bond activation to screen different metal and metal oxide clusters and surfaces.

We have demonstrated a large number of different formats of soluble catalysts to be active for cracking, oxidation and dehydrogenation of hydrocarbon fuels. These catalysts have been analyzed for reactivity in pyrolysis reactors at ambient and elevated pressure and in combustion

environments.

II. Major Accomplishments

1. In the fall of 2011 and spring of 2012 we used X-ray absorption techniques to show that we can covalently bond the zirconia to the carbon in a MWNT. Related studies demonstrated increased electronic coupling between components that are covalently bonded. In addition this covalent bonding stabilizes the zirconia nanoparticles under reaction conditions. We also showed that these catalysts are active for hydrocarbon cracking, and, when doped with a precious metal catalyst component can significantly accelerate fuel lean combustion. The catalyst without precious metal exhibits excellent activity for cracking cyclohexane at temperatures consistent with fuel preheating and represents a new paradigm in catalyst design and is inexpensive to fabricate. We presented these ideas to UTRC (Pfefferle, Haller and Gorte).

2. Using an upstream pyrolysis reactor to a combustion reactor we have demonstrated how the endothermic cracking and dehydrogenation reactions that provide the cooling also change the chemical composition of the fuel and that this can either enhance or inhibit ignition of the fuel in the engine. Product profiles and conditions that most enhance ignition with a range of different catalysts has also been defined. This work involved catalysts from 3 PIs with 2 other PIs doing the experimental measurements. Some of the results are presented below.

3. We developed MWNT supported Pt/Co catalysts that greatly reduce the amount of precious metal required. These catalyst formats were examined in the reactor of Vajda, allowing *in-situ* analysis of reactivity and catalyst size/morphology. The Pt metal catalysts supported on MWNT have been examined under reaction conditions. Using in situ GISAXS, GIXAS and TPR_x we found that metallic Pt showed good stability maintaining their particle size during reaction. We also observed strongly size/support and pretreatment dependent selectivity in the dehydrogenation of cyclohexane. Accompanying theoretical work by Neurock provided fundamental insights into the particle size effect on the selectivity to different reaction products. The theoretical results are consistent with those observed in Vajda's experiments with quantitative particle size agreement. These results are presented as Appendix I.

4. Well defined, model catalyst systems were prepared by deposition of size selected subnanometer Co_{27±4} clusters on various metal oxide supports (Al₂O₃, ZnO and TiO₂ and MgO). The oxidation state and reactivity of the supported cobalt clusters were investigated by temperature programmed reaction (TPRx) and *in-situ* grazing incidence X-ray absorption (GIXAS). Our results show that the MgO supported cobalt catalysts were about a factor of three more active than the same clusters supported on alumina, titania or zinc-oxide. Moreover, the magnesia-supported clusters have a low light up temperature (~200 °C) and it maintains high reactivity at 300 °C. The change of the nature of the chemical state of cobalt on various oxide surfaces, along with the ability of subnanometer clusters to form fluxional, highly active nanostructures that adapt their morphology to offer the optimal reaction pathway, can represent key elements for high reactivity as well as selectivity. The most interesting aspect behind the high activity of MgO supported cobalt catalyst is the formation of a cluster-based nanoassembly during the culmination of the reaction, accompanied by significant change of the oxidation state of cobalt. The turnover rates can make such material compositions attractive as alternatives to precious metal based low-temperature dehydrogenation catalysts.

5. Well defined sub-nanometer cobalt and nickel clusters prepared by cluster ion beam deposition methods have been used to study size and support effects in the Fischer-Tropsch/methanation reaction. The chemical state of the nanoparticles and its changes occurring during reaction were investigated using *in situ* XANES at atmospheric pressure and temperature up to 225 °C. The results indicate that 1) performance of sub-nanometer particles can be controlled via the size of the clusters, 2) metal support interaction offers an additional key to control activity and selectivity in FT synthesis, and 3) new, carbon based supports could play important role in future production of fuels from syngas. Under applied reaction conditions, the 27-atom cobalt clusters are by more than order of magnitude more reactive than 4-atom clusters, while UNCD-supported 27-atom clusters are more than two times more active than alumina supported ones. XANES results suggest that controlling the electronic structure of sub-nanometer cobalt clusters via cluster-support interactions could lead to a fundamentally new level of understanding of the function of (sub)nanoscale materials, not observed at the nano- or microscale.

6. We have used theory and simulation in order to examine the activation and conversion of propane and cyclohexane over: 1) Pt and Co metal clusters, 2) Pt and Co metal clusters supported on carbon nanotubes and 3) a bare cobalt oxide surface. We examine in detail the elementary steps involved in the dehydrogenation of propane to propylene and cyclohexane to cyclohexene. The initial C-H bond activation and removal of aromatic products were found to be rate-controlling steps. We use the initial C-H bond activation to screen different metal and metal oxide clusters and surfaces. The cobalt oxide calculations are presented in section 6B below.

7. Modeling of the dehydrogenation of propane over Co oxide gave insights into mechanism and identified active sites. Our experimental results indicate that the Co clusters oxidize during reaction and that the Co oxide particles that form are active for dehydrogenation of alkanes. We have established the first theoretical results that show that different Co_3O_4 surfaces are active for alkane dehydrogenation and demonstrate the influence of surface structure on reactivity. We also showed that the active sites involve Co-O* site pairs where the barriers that control C-H bond activation are controlled by the basicity of the O* involved in carrying out a hydrogen abstraction from the alkane. The activation barriers as such correlate linearly with the hydrogen binding energy as well as the band gap of the oxide establishing the role of electron transfer from the C-H bond that is activated into the lowest unoccupied orbital on the oxide. This is consistent with C-H bond activation over reducible oxides such as vanadia and molybdena. The results are described below.

8. Theoretical calculations confirm the EXAFS results that indicate that the ZrO_2 clusters form strong Zr-O-C bonds that anchor the nanoparticles of ZrO_2 to the surfaces of the carbon nanotube. These interactions occur at the edges as well as at defect sites. The bonding between the closed non-defective CNTs is weak and as such is not likely to be important in the synthesis of active sites. First principle theoretical calculations indicate that the cracking proceeds via carbenium ion mechanism where a proton from a Brønsted acid site attacks the hydrocarbon backbone to activate the C-C bond. There appears to be a direct correlation between the activation barriers for cracking and the acidity of the site as measured by the deprotonation energy for different catalytic materials.

9. We extended the synthesis methods we had developed for Pd@ceria to Pt@zirconia and are working to prepare Ni@zirconia, since literature reports have shown that Pt/zirconia catalysts can exhibit acid-like behavior for reforming and oligomerization reactions and because Ni/zirconia is active for normal reforming.

10. We have demonstrated a large number of different practical formats of soluble catalysts to be active for cracking, oxidation and dehydrogenation of hydrocarbon fuels (Pfefferle, Haller, Gorte, Flytzani-Stephanopoulos). Many of these catalysts have been analyzed for reactivity in pyrolysis reactors at ambient and elevated pressure and in combustion environments.

11. Dispersions of MWNT supported Co and Pt nanocatalysts, and soluble cobalt oxide nanoparticles have been functionalized and all remain dispersed for months. We have developed several soluble catalyst formats that do *not use precious metal components*. These are based on sulfated zirconia and nano- Co, Ni and zirconia.

12. This work has provided insight into reactivity of carbon nanotubes as a function of chirality. In order to graft metal precursors to the nanotubes we carried out point of zero charge measurements on different cuts of tubes. We found significant variation as a function of type/diameter. The same trend was verified in calculations by Neurock (included below). The effect is being used to develop a new method for separating nanotubes by chirality using pH gradient liquid chromatography.

III. RESEARCH RESULTS

1. Dispersible Base Metal Oxide Catalysts

Maria Flytzani-Stephanopoulos, Tufts

The work conducted at Tufts University over the duration of the MURI program, has successfully demonstrated that base metal oxides at the nanoscale can be used to dehydrogenate jet fuels with high selectivity to olefins/aromatics even in the presence of large air/fuel ratios. The activity of oxides at the nanoscale, while not as high as that of metals (Pt, Co, etc.), is superior to that of microcrystalline oxides. Both cobalt and iron oxide nanoparticles are active for the oxidative dehydrogenation (ODH) of cyclohexane to benzene, the former much more active than the latter. In follow-on work, doping of the oxides was investigated. This has shown that the addition of gold as a minority component into iron oxide nanocrystals increases the selectivity of the reaction to benzene. Since a primary motivation for this work is the addition of catalysts in jet fuels to facilitate the dehydrogenation and cracking reactions preceding their combustion, a low-cost, sacrificial catalyst is sought after. Accordingly, in the last two years of the project, we focused on the effects of mixing base metal oxides containing no precious metals.

Using a simple surfactant-free hydrothermal synthesis method, iron oxide nanoparticles were doped with varying amounts of cobalt to examine the effect of cobalt content and oxidation state on the selectivity and activity of the iron oxide for the ODH of cyclohexane. The choice of the cobalt oxide as additive was justified from some preliminary promising work with cobalt ferrites that we had performed at Argonne, where we found them to be more stable than neat CoO_x under *in situ* reaction conditions monitored by GISAXS. We have shown previously that small ($\sim 5\text{nm}$) cobalt oxide nanoparticles favor the production of benzene over the partial dehydrogenation products cyclohexene and cyclohexadiene, or the complete oxidation product carbon dioxide. However, these turn into good combustion catalysts above $\sim 325^\circ\text{C}$. This naturally led us to consider whether the ferrite compositions would stabilize the ODH-active form of cobalt and extend the use of ferrites to high temperatures where their activity would also be higher. Indeed, a great improvement

of selectivity to benzene was found in the mixed phase catalysts containing 10-30% Co. For example, benzene selectivity > 90% at 370 °C was found for cobalt ferrite, while at the same temperature, iron-free CoO_x lost almost all of its dehydrogenation activity, producing > 90% CO₂. By detailed XPS analysis, the selectivity to benzene was correlated with the amount of octahedrally coordinated Co (II) atoms in the various catalyst compositions.

Cobalt-doped iron nanoparticles were prepared by a surfactant-free hydrothermal co-precipitation technique that enabled a high degree of composition and size control. The samples were characterized via Transmission Electron Microscopy (TEM), powder X-Ray Diffraction (XRD), X-Ray Photoelectron Spectroscopy (XPS), BET N₂ Physisorption, and CO Temperature Programmed Reduction (CO-TPR). These characterizations helped us to correlate the selectivity and activity data for each catalyst and shed light into the role of the surface species. It was found that iron oxide nanoparticles doped with 2-10 at.% cobalt formed a stable surface phase, enriched in Co (20 at.%), independent of the bulk concentration. XPS measurements identified that this phase is rich in octahedral Co²⁺ cations. The selectivity to benzene was much higher in the Co-promoted iron oxide samples. Addition of cobalt also promoted the activity of the iron oxide nanoparticles, and stabilized them against particle growth under the reaction conditions. Reactions were run dynamically in ramping up and down the temperature up to 370 °C, and in steady-state measurements at several points along the way, in a mixture of 0.4% cyclohexane and 4% oxygen, for a total of several hours on-stream.

Frequent use of the synchrotron facilities at Argonne National Lab was made through the course of the project. Kinetic information obtained in temperature-programmed reaction (TPRx) conditions at Argonne, and in a packed-bed reactor facility at Tufts was compared and found similar. The theoretical support (Virginia) and the actual testing of our suspended catalyst samples at the furnace facility (Yale) have helped the research direction taken along the way. Exciting new findings in the ODH by oxides is the outcome of our collaborative work in this MURI project, and these have been reported in two papers published in ACS Catalysis, and included in two additional papers under review and preparation at the time of this report. Several other outcomes of the project are noted, including the completion of two M.S. theses, partial contribution in seven more published papers, and oral presentations in national and international meetings.

1.1 Synthesis methods

There are many synthesis techniques reported in the literature for the synthesis of cobalt and iron oxide nanoparticles. These include surfactant-free hydrothermal co-precipitation¹, thermal decomposition²⁻⁴, and surfactant-assisted hydrothermal co-precipitation⁵. The precipitation method proposed by Dong et al.¹ for the synthesis of size-controlled Co₃O₄ nanoparticles was modified in this work to prepare cobalt-iron oxides of varying compositions. This technique is advantageous over the others for several reasons. While thermal decomposition yields adequate size control and allows for excellent shape control, the technique is arduous due to the number of steps in the synthesis, and thus not conducive to producing materials of varying compositions. In contrast, the synthesis used herein is a simple two-step procedure, which by its nature allows for precise composition control as well as broad size control. A pitfall of the surfactant-assisted methods is the need for the removal of a surfactant prior to reaction testing. This method circumvents both of these issues. Additionally, this synthesis offers a means to control the sizes of the resultant nanoparticles. Dong *et al.* altered the nanoparticle sizes by changing the ethanol:water ratio during the heating step of the procedure. Higher concentrations of ethanol lead to smaller

particles, while lower concentrations increase the size. It also controls the particle size by altering the metal precursor concentration. In this work, the total metal ion concentration was fixed at $7.3 \times 10^{-5} \text{ M}$. Increasing this concentration was found to increase particle size. Fig.1.1 shows a rather narrow particle size distribution for cobalt ferrite prepared in our work ⁶.

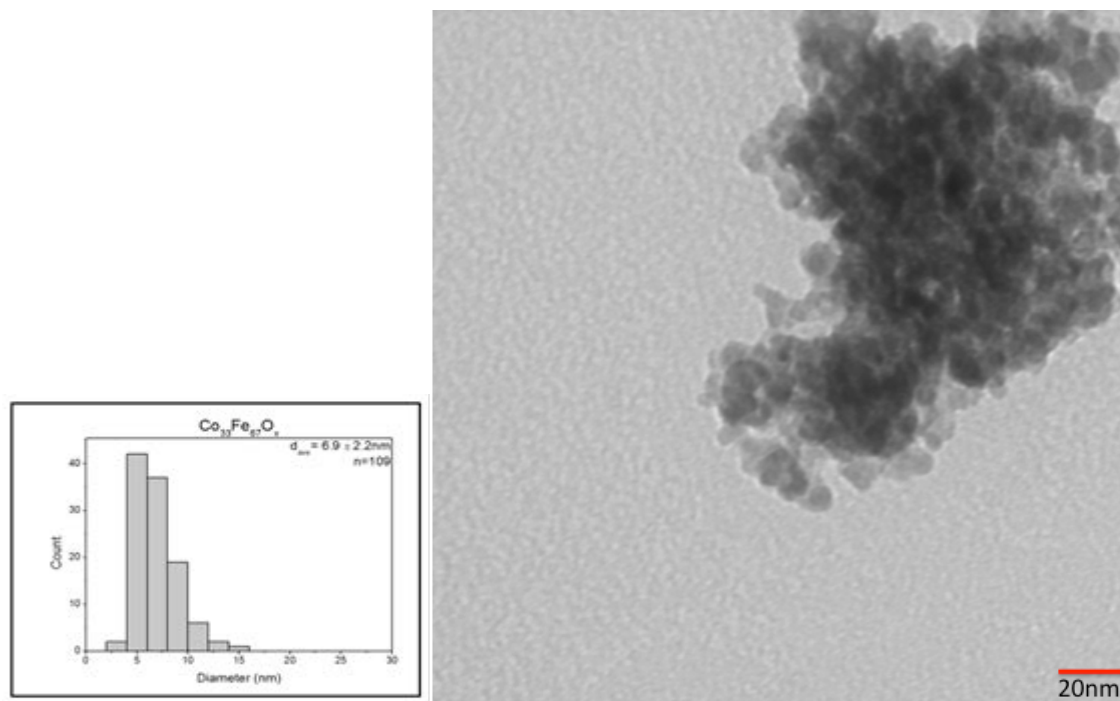


Fig. 1.1. TEM image and particle size distribution of fresh $\text{Co}_{33}\text{Fe}_{67}\text{O}_x$ ⁶

1.2 Catalyst Characterization

The techniques used in this work allow us to infer what species and at what chemical state they are most probably present on the surface. From these analyses and with the aid of reaction data, we can select compositions that are most suitable for the oxidative dehydrogenation of cyclohexane. The (111) and (110) facets of Co_3O_4 were recently compared by DFT calculations for the oxidative dehydrogenation of propane. The (111) surface of Co_3O_4 presents tetrahedral Co^{2+} cations as the outermost layer, while the {110} surface exposes Co^{2+} , Co^{3+} , and O^{2-} . ⁷ In the same paper, it was shown that the most likely mechanism for dehydrogenation is homolytic hydrogen abstraction over a metal-oxygen site. ⁷ It was also proposed that the most favorable surface for this to occur on is the (110) terraced surface, and that specifically, the active site is the weakly held surface oxygen. Detailed XPS analyses of the samples prepared and tested in this work allows the identification of the ODH-relevant cobalt species. As shown in Fig. 1.2, the XP spectra of samples with cobalt loadings greater than 33% show a significant amount of cobalt in all 3 oxidation states; octahedral 2+ and 3+, as well as tetrahedral 2+, however the samples with cobalt loadings less than 33% contain cobalt almost entirely in its octahedral 2+ state. As we will see below, these were the most selective catalysts in the ODH of cyclohexane to benzene.

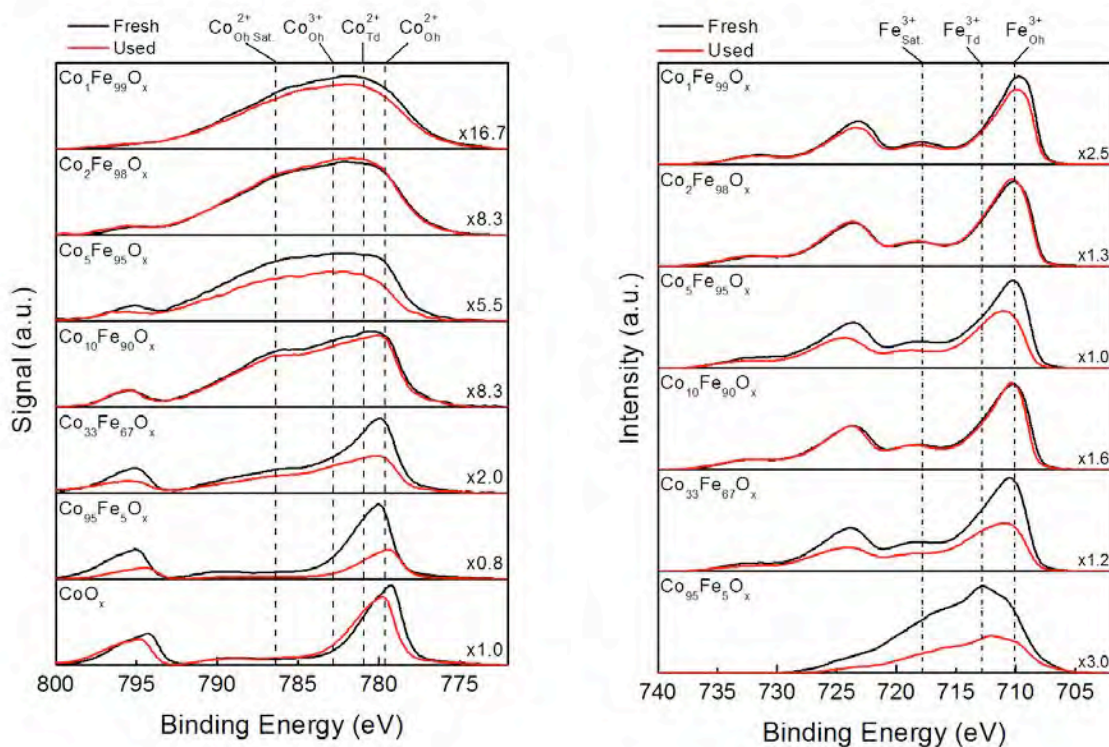


Fig. 1.2. Fresh and Used Cobalt 2p and Iron 2p XP Spectra

1.3 Catalyst activity and selectivity

Steady-state reaction rates are shown in an Arrhenius-type plot in Fig. 1.3. These rate data have been plotted alongside the reaction rates reported by our group previously as well as data collected from the literature.^{7,8} The samples prepared in this work are much more active for the ODH of cyclohexane than the iron oxide catalysts prepared in previous work of our group, including FeO_x cubes and octahedra, either doped with gold or without.⁸ These catalysts also greatly surpass the activity and selectivity of 12nm CoO_x particles prepared previously.⁷ However, the rates over the high cobalt-content catalysts prepared in this work are nearly equivalent to the rates reported for 5nm CoO_x particles.⁶ Overall, the addition of cobalt into iron oxide was found to greatly increase activity, and the apparent activation energies were all similar, indicating the same (Co-based) species were the active catalyst sites. However there is a tradeoff; namely, samples with cobalt loadings greater than Co₁₀Fe₉₀O_x exhibited much lower selectivity to benzene, especially at elevated temperatures.

Up to the Co₁₀Fe₉₀O_x composition, all Co-based catalysts exhibit similar reaction rates, albeit slightly lower than that of the cobalt ferrite composition, and they all exhibit high selectivity to benzene. The similar activity can be explained by the ~20 at.% cobalt content on the surface of all these catalysts as determined by XPS. The XP spectra shown in Fig. 1.2 show that the surface states of all four catalysts are similar. On the other-hand, the high cobalt-content samples exhibit higher overall benzene production, but they completely oxidize a significant portion of the feed to CO₂. In comparison, samples Co₅Fe₉₅O_x and Co₁₀Fe₉₀O_x maintain >90% selectivity to benzene at high conversions (90%) even at the highest reaction temperature tested, i.e. 370 °C. The good stability of

these catalysts was verified by repeating the steady state reaction program and comparing the conversion of cyclohexane during each cycle.

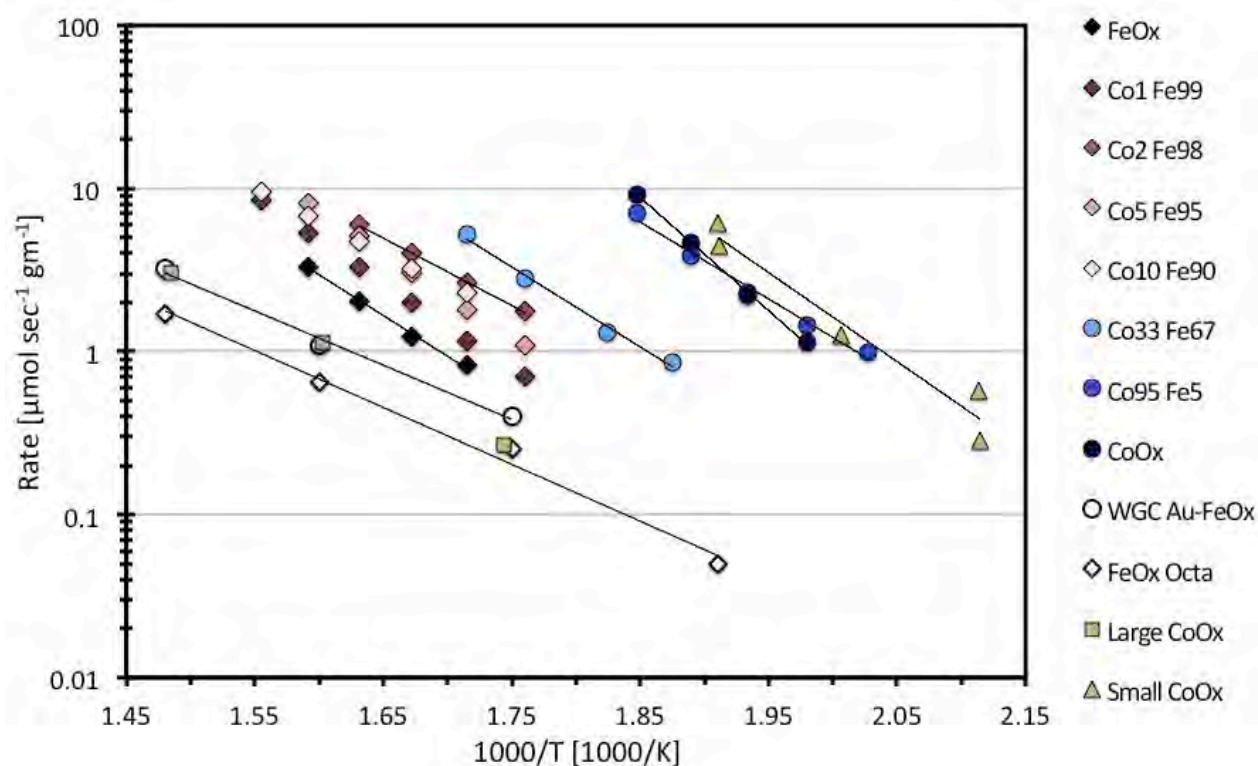


Fig. 1.3. Reaction Rates as a function of Co-content.^{7,8}

The effect of cobalt doping is most clearly shown when analyzing the selectivity as a function of temperature and $\text{Co}^{2+}_{\text{Oh}}$ satellite area. Fig. 1.4 clearly shows the ability of octahedral Co^{2+} to stabilize the surface of these materials and ensure that selectivity to benzene remains very high, even at the highest temperatures tested. At low temperatures, there is minimal effect of increased octahedral Co^{2+} ; and selectivity remains high for all compositions. However as temperature is increased, the samples with low relative amounts of octahedral Co^{2+} experience drastic reductions in selectivity to benzene. This is clearly contrasted by the ability of the samples with high relative octahedral Co^{2+} to maintain high selectivity.

In conclusion, our work has shown that the addition of cobalt into iron oxide nanoparticles has a strong promotional effect on the rate of the ODH reaction, and that octahedrally coordinated Co^{2+} cations are responsible for inducing and maintaining high selectivity towards dehydrogenated reaction products, while inhibiting the formation of either complete or partial oxidation products, i.e. CO or CO_2 .

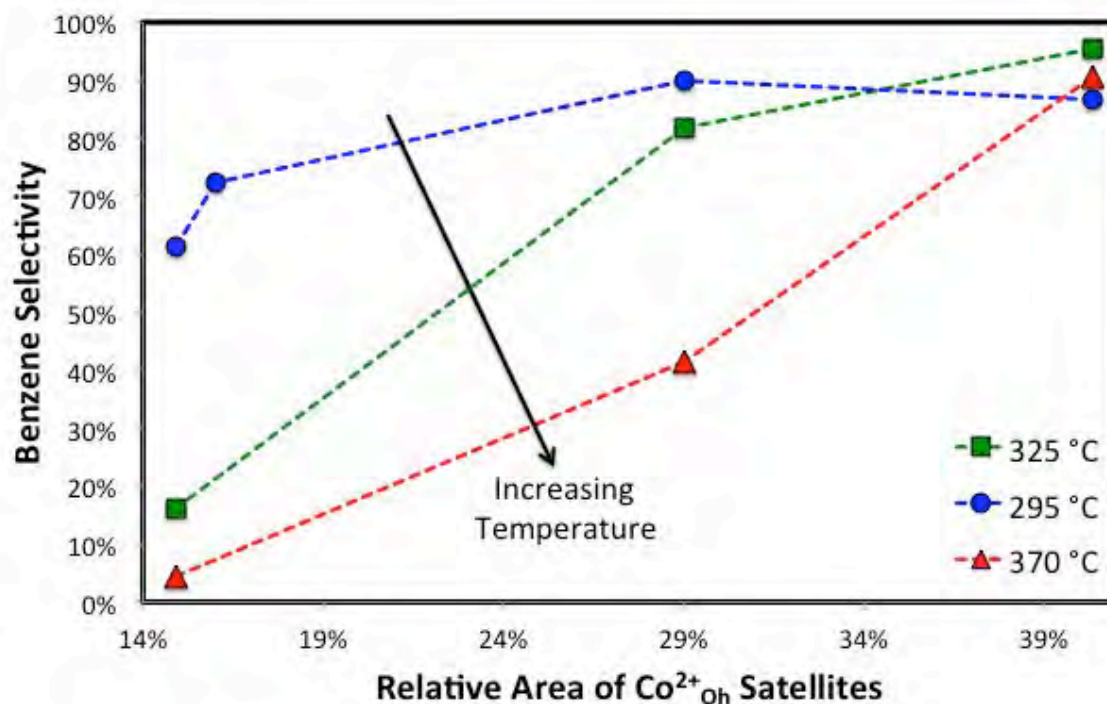


Fig. 1.4. Selectivity to Benzene as a Function of Temperature and Co²⁺_{oh} Area.⁶

2. Oxide coated Dispersible Nanoparticles

Ray Gorte, University of Pennsylvania

The initial goals of work at Penn were to produce core-shell, Pd@ceria nanoparticles that were soluble in hexane and decane solutions. The idea behind this goal was to make fuel-soluble catalysts that take advantage of the promoting effect that ceria has on catalytic metals for reforming and total oxidation. This work was successfully completed by preparing 2-nm Pd particles with alkanethiol ligands, exchanging the alkanethiols with thiols having carboxylic end groups, and reacting the carboxyl end groups with cerium alkoxides.

We extended this work, first by demonstrating that we could also prepare similar core-shell materials with Pt at the core and either zirconia or titania as the shell. The method for preparing these materials was again based on self assembly but the procedure for preparing Pt nanoparticles required a stronger reducing agent. Transmission Electron Microscopy (TEM) of these nanostructures confirmed the formation of distinct metal cores, ~2-nm in diameter, surrounded by amorphous oxide shells. Functional catalysts were prepared by dispersing the nanostructures onto an alumina support; and vibrational spectra of adsorbed CO, together with adsorption uptakes, were used to demonstrate the accessibility of metal core to CO and thus the porous nature of the oxide shell.

We can deposit these particles in monolayer form onto functionalized supports. The monolayer form of these catalysts has phenomenal activity for hydrocarbon combustion, with

Pd@ceria/alumina catalysts exhibiting rates that are a factor of more than 40 higher than the best Pd/ceria catalyst we could produce. Furthermore, these catalysts were found to be stable at 850°C, apparently due to the core-shell structure.

Using similar approaches, we prepared nanocomposites in which Multi-Walled Carbon NanoTubes (MWCNTs) were embedded inside mesoporous layers of oxides (TiO_2 , ZrO_2 or CeO_2), which in turn contained dispersed metal nanoparticles (Pd or Pt). We showed that the MWCNTs induce the crystallization of the oxide layer at room temperature and that the mesoporous oxide shell allows the particles to be accessible for catalytic reactions. In contrast to samples prepared in the absence of MWCNTs, both the activity and the stability of core-shell catalysts is greatly enhanced, resulting in nanocomposites with remarkable performance for the water-gas-shift reaction (WGSR), photocatalytic reforming of methanol, and Suzuki coupling. The modular approach shown here demonstrates that high-performance catalytic materials can be obtained through the precise organization of nanoscale building blocks.

In addition to catalyst synthesis, we have developed a high-pressure, micro-reactor in order to simulate the conditions required by catalysts in the scram-jet engine application. This reactor consists of an HPLC pump, a small tubular reactor, and a GC-Mass Spec for product determination.

In the initial proposal, we had focused on using soluble metal catalysts with optimized metal-support interactions to promote reforming. Although reaction measurements in our high-pressure reactor did not demonstrate that this approach was likely to be successful, we did complete these studies with an examination of the metal-crystallite size and support effects for CO oxidation. In this work, interactions between ceria (CeO_2) and supported metals were investigated using catalysts in which the metal (Ni, Pd, and Pt) particle sizes were highly monodispersed. Rate measurements on these samples demonstrated unambiguously that CO oxidation in ceria-based catalysts is greatly enhanced at the ceria-metal interface sites for a range of group VIII metal catalysts, clarifying the pivotal role played by the support. Also, the use of monodisperse nanocrystals was shown to be a powerful tool for characterizing the role of the metal-support interface in ceria-based systems and explaining their remarkable activity. This work has been accepted for publication in Science.

A promising route for endothermic reforming applications involves the use of acidic zeolites. In our first studies of hydrocarbon cracking under supercritical conditions, we examined n-hexane cracking over H-ZSM-5 at pressures from 0.03 to 137 bar, between 558 and 633 K. The rates showed the effects of saturated adsorption for n-hexane in the zeolite, with the reaction being first-order at low pressures and zeroth-order at high pressures. The activation energy also changed with increasing pressure by an amount equal to the heat of adsorption of n-hexane in ZSM-5, going from 170 kJ/mol to 90 kJ/mol. The selectivity for C-7+ products varied only with temperature and conversion. The catalyst was also remarkably stable with time.

Preliminary measurements on other zeolite structures, H-Y, H-MOR, and H-BETA, suggest that the conclusions from H-ZSM-5 cannot be extrapolated to other zeolite structures. H-Y is a large-pore zeolite, commonly used in Fluid Catalytic Cracking (FCC) in refineries. As-synthesized, Y zeolites have low Si:Al ratios that are unstable upon heating but the material can be stabilized by exchange with rare-earth cations (e.g. La^{+3}) or by careful steaming to produce materials with higher Si/ Al_2 ratios that are commonly referred to as ultra-stable Y (USY) zeolites. H-BETA is another large-pore zeolite with the advantage that it can be produced in high-silica forms directly. BETA finds

application as a hydrocarbon adsorbent in automotive emissions-control systems. MOR is a one-dimensional, high-silica zeolite that finds application in hydrocracking.

In recently acquired data at Penn, four major differences were observed in n-hexane cracking over H-Y, H-BETA, and H-MOR compared to what was observed on H-ZSM-5, suggesting that there are major mechanistic differences on the large-pore zeolites. First, even though n-hexane cracking rates at 400°C and ambient pressures are similar on each of the three zeolites, rates do not increase dramatically with pressure on H-Y and H-BETA, so that TOF for H-ZSM-5 are typically a factor of 30 higher at 400°C and 137 bar. This is shown in Figure 2.1. Second, the measured activation energies at high pressures are much lower on the large-pore zeolite. This means that the differences between H-ZSM-5 and the large-pore zeolites, which are already significant at 400°C, will be much greater as the temperature increases. Third, at higher pressures on the large-pore zeolites, we observe an induction period that can be as long as 20 minutes. The induction period is a strong function of pressure and is observed only at lower temperatures. Under conditions where it is observed, the rates start out very low, then increase dramatically at some point in time. Fourth, we observe relatively rapid deactivation due to coking on H-Y, H-MOR, and H-BETA at high pressures. As expected, the rate of deactivation increases with temperature but is significant even below 400°C. Reaction rates could be restored by oxidation of the catalysts, demonstrating that deactivation is not associated with destruction of the zeolite catalyst.

Each of these four observations suggests that bimolecular reaction mechanism likely dominates in the large-pore zeolites. Because the bimolecular reaction is associated with the presence of a surface carbenium ion (essentially a strongly adsorbed, protonated olefin), high pressures of the alkane are not important for establishing high surface coverages, so that the reaction will be much less pressure dependent. The activation energies for the bimolecular reaction are known to be much lower than those observed for the monomolecular reaction because the rate limiting steps are different and the energy barriers for hydride-transfer reactions tend to be much lower than that for protonation of an alkane. (When the hydride-transfer reaction is operational, the presence of an adsorbed carbenium ion on the Brønsted sites effectively blocks the monomolecular process, so that the two processes cannot simply operate in parallel.) Also consistent with the bimolecular mechanism is the observation of an induction period at low temperatures. The induction period is associated with the initial formation of olefins products, which then adsorb on the acid sites and are responsible for the higher rates. Finally, coking in zeolites is usually associated with formation of carbonaceous deposits that form when too much hydrogen is removed by hydride transfer processes.

What is perhaps most important is that the bimolecular reactions found in large pore zeolites should be suppressed so effectively in the medium-pore zeolite, H-ZSM-5. This is probably due to spatial constraints that minimize the importance of biomolecular processes. The absence of bimolecular processes is likely the reason for the high stability observed with H-ZSM-5 in our study, which is of critical importance for endothermic reforming applications. Obviously, understanding this chemistry is a crucial if we are to control these reactions and take advantage of zeolite

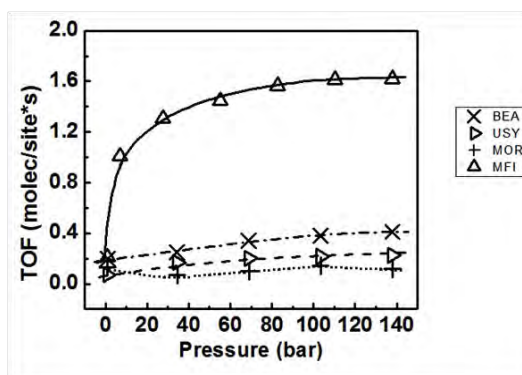


Fig. 1 TOF VS. pressure at 633K

cracking chemistry to perform endothermic reforming. This work is presently being written up for publication.

3.0 Soluble Carbon Nanotube Supported Catalysts

3.1 Sulfated Zirconium Oxide Covalently Bonded Nanoparticles on Multi-walled Carbon Nanotubes as Catalysts and Catalyst Supports, Gary L. Haller, Lisa Pfefferle

Department of Chemical and Environmental Engineering, Yale University

Multi-walled carbon nanotubes (MWCNT) have been a focus of our work for catalyst supports. We have shown that they are robust and can lead to a stable high dispersion of the catalytically active component. They can also aid in reaction selectivity by allowing hydrogen or other reactants or intermediates to spill over on to the carbon support. Much of our recent work on MWCNT focuses on grafting metals or zirconia to the MWCNT support. The MWCNT Pt and Co catalysts have been described in earlier reports and in our papers so here we focus on the sulfated zirconia catalysts.

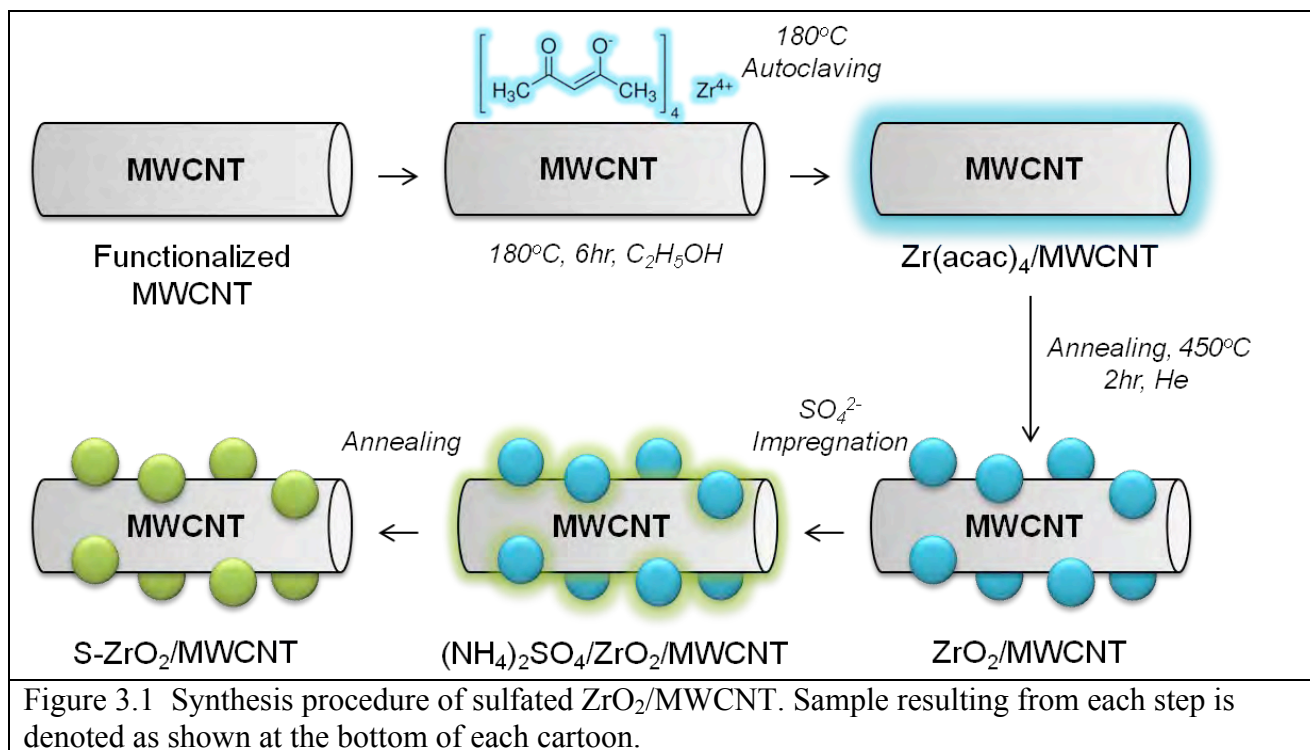
No previous study to ours demonstrated the synthesis of zirconia precursors to ZrO_2 particles that would covalently bond to the MWCNT. In our studies the Zr precursor was zirconium acetyl acetate, grafted to MWCNT in ethanol, dried and annealed (crystallized). The dried mixture was heated in an inert atmosphere to 450°C which resulted in covalent bonding between the ZrO_2 particles and the MWCNT surface. Zirconium oxide nanoparticles covalently bonded to multi-walled carbon nanotubes (MWCNT) were synthesized. X-ray absorption at the C and O K-edges was used to confirm the covalent bonding between ZrO_2 nanoparticles and MWCNT via Zr-O-C bonds. The ZrO_2 /MWCNT have been characterized by (scanning) transmission electron microscopy ((S)TEM), X-ray diffraction (XRD), in situ small-angle X-ray scattering (SAXS), in situ wide-angle X-ray scattering (WAXS), and near edge X-ray fine structure (NEXAFS) for the purpose of a comprehensive analysis of the ZrO_2 particle size and particle size stability. This is discussed in detail in our paper Liu et al. (2012a) in the publication list of this report. The MWCNT support stabilizes the particle size of the zirconia under high temperature conditions. At moderate concentrations the zirconia (e.g. 15wt%) the particle size stays between 2-3nm up to annealing temperatures of 750°C .

Sulfated zirconium oxide (S-ZrO_2) is a well-known solid acid that has potential applications for fuel cell electrodes and biomass processing when supported on MWCNT, which gave us the inspiration of compositing them into the composite solid acid catalyst system, $\text{S-ZrO}_2/\text{MWCNT}$. The nature of the acid sites formed by sulfate anion interaction with the zirconium oxide was probed by C, O, S and Zr K-edge X-ray absorption. Binding energies determined from the K-edge shifts, indicate a net shift of electronic charge from Zr to S, consistent with various models for the acid sites, not previously studied by X-ray absorption. The acid sites were also analyzed using the probe reactions of cyclohexane dehydrogenation/cracking and butane dehydrogenation.

To prepare the $\text{S-ZrO}_2/\text{MWCNT}$ catalyst, the $\text{ZrO}_2/\text{MWCNT}$ composite was impregnated with aqueous $(\text{NH}_4)_2\text{SO}_4$ (with molar ratio of $\text{S/Zr} = 2$ if all S was retained) and thermally treated again in order to form sulfated $\text{ZrO}_2/\text{MWCNT}$ ($\text{S-ZrO}_2/\text{MWCNT}$). This thermal treatment was performed either (1) in flowing He at 450°C for 2 hr or (2) in flowing mixture of 0.5% O_2/He for 10 min (4%

O₂/He mixed gas balanced with ultrahigh purity He, both purchased from Airgas). A full description is given in Liu et al. (2012b) in the publication list of this proposal.

A schematic of the process for making the MWCNT supported sulfated zirconia is shown below in figure 3.1

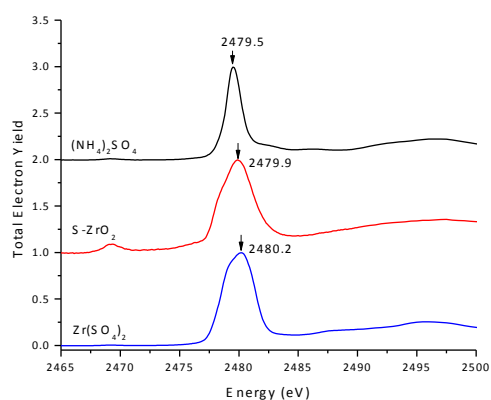


Using synchrotron radiation, the S K-edge X-ray absorption near-edge spectroscopy (XANES) can be used as a fingerprint of the oxidation states of the S species in that the absorption edge shifts 10 ~ 12 eV to higher energy as the oxidation state increases. Moreover, a third-derivative analysis method of the S XANES has been developed to discriminate the number and kind of sulfur species interacting with the zirconia.

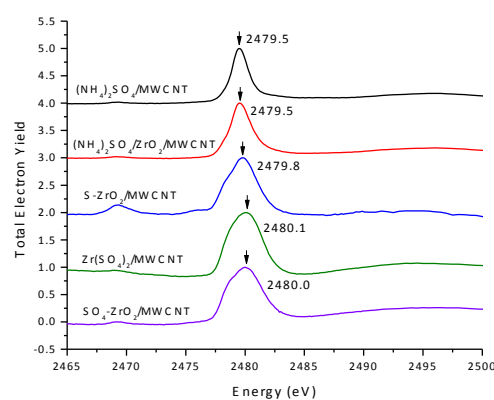
In our catalyst system, however, the S K-edge (2472 eV) is bracketed by the three Zr L-edges (L_I 2532 eV, L_{II} 2307 eV, L_{III} 2223 eV), which complicates the S XANES analysis but at the same time gives us the advantages of looking at the two elements simultaneously. This has been made possible by beamline X15B at the National Synchrotron Light Source at Brookhaven National Laboratory. Here, we report a XAS analysis of the S-ZrO₂ solid acid catalyst system with the analysis of Zr and S XANES (XANES that spans all three Zr L-edges and S K-edge), in combination with conventional S XANES, first-derivative and third-derivative analysis. To our knowledge, this is the first multiple-edge analysis of XANES on a sulfated ZrO₂ catalyst system, apart from our previous reported work on this S-ZrO₂/MWCNT. Traditionally, at the low energy range of Zr L-edges and S K-edge, it is very difficult to continuously collect data that extends over 400 eV with a stable beam and clean peak features, which marks the significance of our combination of Zr and S XANES spectra.

In order to further probe the $\text{SO}_4^{2-}/\text{ZrO}_2$ species and test our hypothesis, we used S XANES and performed first-derivative and third-derivative analyses on the spectra. The results are summarized in Figure 3.2. In the left column, three reference compounds are compared - $(\text{NH}_4)_2\text{SO}_4$ pure compound (black), commercial S-ZrO₂ catalyst (red), and $\text{Zr}(\text{SO}_4)_2$ hydrate (blue). The XANES signals were measured in the total electron yield mode. In Figure 3.2 (a), the intensity of all three peaks is normalized to 1. The peak position shifts to higher energy and the peaks for S-ZrO₂ and $\text{Zr}(\text{SO}_4)_2$ are much broader than that of $(\text{NH}_4)_2\text{SO}_4$. In Figure 3.2 (b), more distinctive differences are present in the first-derivative of these spectra. The first y-maximum of the first-derivative marks the edge position – 2479.1 eV for $(\text{NH}_4)_2\text{SO}_4$, 2477.8 eV for S-ZrO₂, and 2478.6 eV for $\text{Zr}(\text{SO}_4)_2$. In this range of S K-edge energy, the S species is sulfate (S^{6+}), that is, a species with S in the +6 oxidation state, but due to the fact that the sulfate has a different chemical environment, the edge position exhibits minor shifts. The first-derivative of S-ZrO₂ has two peaks, at 2477.8 eV (edge position) and at 2479.1 eV (same as the edge position of $(\text{NH}_4)_2\text{SO}_4$). For the $\text{Zr}(\text{SO}_4)_2$, the fine structures are not fully resolved. In Figure 3.2 (c), third-derivative was taken of the XANES, and two doublets are resolved in $\text{Zr}(\text{SO}_4)_2$. The third-derivative of S-ZrO₂ resembles that of $\text{Zr}(\text{SO}_4)_2$, but the peak positions are different. Moreover, since the S content in S-ZrO₂ is much lower than that in the pure compounds, the S/N ratio of S-ZrO₂ is much lower too. Because of this, the peak at 2469 eV, an artifact intrinsic in the beamline, is more apparent in S-ZrO₂ than the other two references.

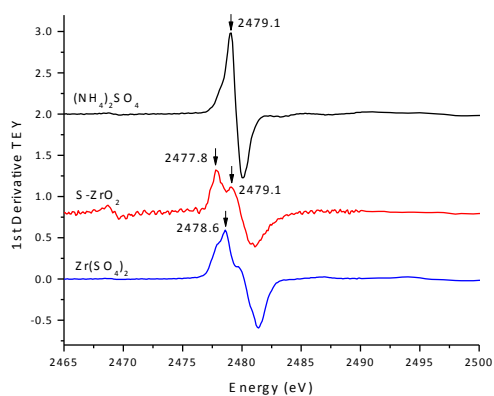
Analysis of this data and additional runs has been very useful in identifying the number and type of sulfur species interacting with zirconia after various treatments. After impregnation, sulfate is associated with both ZrO₂ and MWCNT, the more thermally stable $\text{SO}_4^{2-}/\text{ZrO}_2$ (sulfate interacting with Zr), and the less thermally stable $\text{SO}_4^{2-}/\text{C}$ (sulfate interacting with carbon). We further applied first-derivative and third-derivative analyses to study the $\text{SO}_4^{2-}/\text{ZrO}_2$ interaction. This identified two S species, both with oxidation state of +6, but the one formed on thermal annealing has a lower binding energy of the order of 1 eV. While higher annealing temperature removes more S, about 0.5 wt% S is still retained after 2 hr annealing in He at 450°C. Even though such S is still present after being annealing at 550°C, the S species is different as indicated by the O NEXAFS. Longer annealing time removes more S, as indicated by ZrS-XANES, but it does not change the $\text{SO}_4^{2-}/\text{ZrO}_2$ species. Carrier gas with varied O₂ percentages balanced with He was also used during the annealing and they do not affect the final $\text{SO}_4^{2-}/\text{ZrO}_2$ species either.



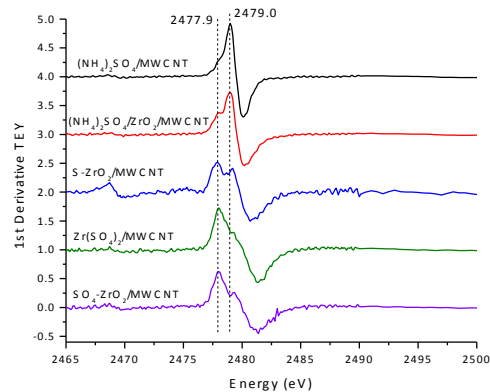
(a)



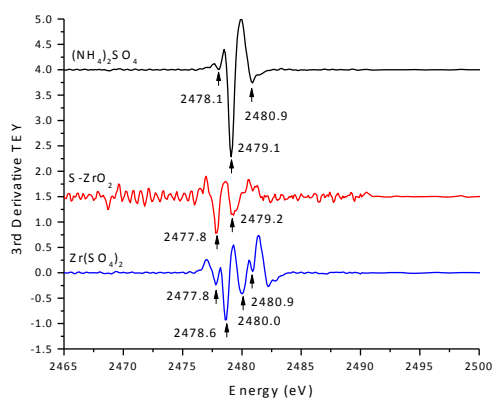
(d)



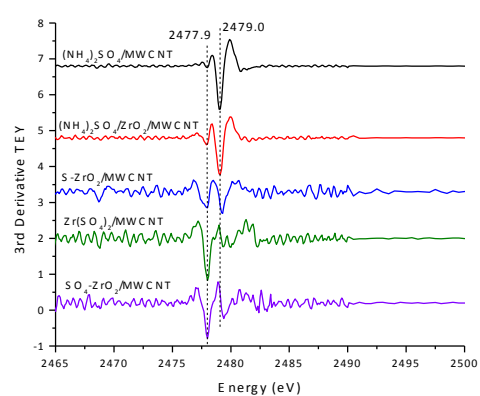
(b)



(e)



(c)



(f)

Figure 3.2. LEFT column: (a), (b), (c) are the raw data, first-derivative and third-derivative of S-XANES TEY signal of 3 references – $(\text{NH}_4)_2\text{SO}_4$, commercial S-ZrO₂ catalyst, and $\text{Zr}(\text{SO}_4)_2$ (hydrate). RIGHT column: (d), (e), (f) are the raw data, first-derivative and third-derivative of S-XANES TEY signal of 5 samples – $(\text{NH}_4)_2\text{SO}_4/\text{MWCNT}$, $(\text{NH}_4)_2\text{SO}_4/\text{ZrO}_2/\text{MWCNT}$, S-ZrO₂/MWCNT, $\text{Zr}(\text{SO}_4)_2/\text{MWCNT}$ (MWCNT reacted or deposited under the same condition used for grafting of ZrO₂/MWCNT but with $\text{Zr}(\text{SO}_4)_2$ precursor), and $\text{SO}_4\text{-ZrO}_2/\text{MWCNT}$ (MWCNT

reacted or deposited with $\text{Zr}(\text{SO}_4)_2$ precursor and annealed). The annealing condition for both $\text{S-ZrO}_2/\text{MWCNT}$ and $\text{SO}_4\text{-ZrO}_2/\text{MWCNT}$ is 450°C in He for 2hr. In (a) and (d), all S K-edge peaks are normalized to 1. In (a), (b), (c), (d), peak positions are marked with arrows. In (e) and (f), peak positions are aligned with dash lines to indicate shifts.

A test for acid catalysis has been performed using the dehydrogenation and cracking of cyclohexane as the probe reaction. The reaction was carried out in the gas phase at atmospheric pressure at a space velocity of 1240 mL (STP) cyclohexane per gram of catalyst per hour. Under these conditions, there was measurable conversion ($\sim 2\%$) at 500°C for the $\text{S-ZrO}_2/\text{MWCNT}$ catalyst thermally treated at 450°C in He (~ 0.5 wt % S); on the same catalyst thermally treated at 450°C in $0.5\% \text{O}_2/\text{He}$, the 500°C conversion was about 20% and the 450°C conversion was about 5% (but immeasurable for the catalyst thermally treated in an inert atmosphere), as shown in Figure 3.3. The increased activity can be mostly attributed to the fact that the $0.5\% \text{O}_2/\text{He}$ treated catalysts retain 4 times as much S as the He treated ones.

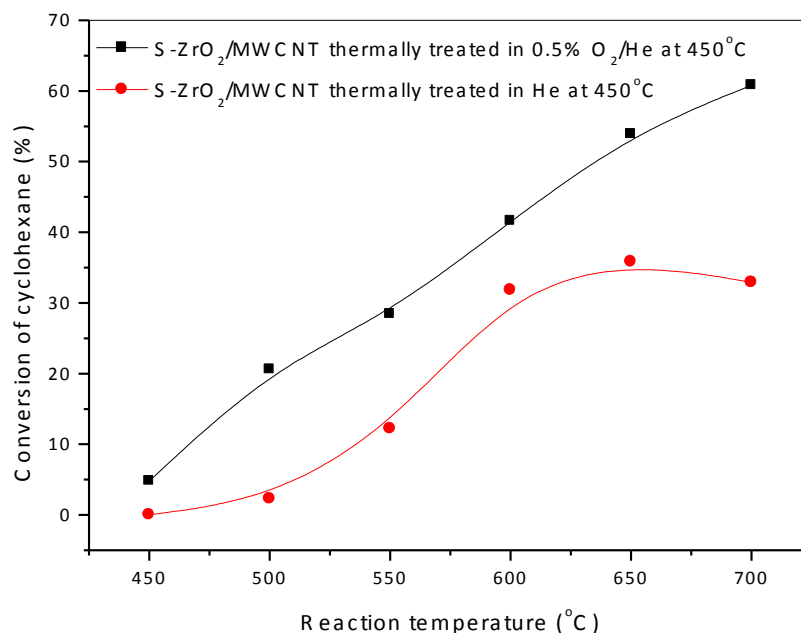


Figure 3.3: Activity of the sulfated zirconia catalyst for cyclohexane dehydrogenation and cracking with catalysts annealed in an O_2/He or He environment.

We took the $\text{S-ZrO}_2/\text{MWCNT}$ catalysts that have been annealed for different times (10 min, 30 min, 1 hr and 2 hr) and probed their activity in the *n*-butane dehydrogenation reaction. These catalysts only differ in the S content. The reaction temperature was ramped to 700°C , and blank experiments using functionalized MWCNT and $\text{ZrO}_2/\text{MWCNT}$ were carried out as a control and these showed no reactivity as expected. All of these $\text{S-ZrO}_2/\text{MWCNT}$ catalysts are active for dehydrogenation to butene. The formation of butene took place in two temperature ranges: (1) at $500 \sim 600^\circ\text{C}$ with production of H_2S ; and (2) at 700°C with production of H_2 . The measured mole

fractions of H_2S and H_2 during each period are correlated with the annealing time of the catalysts during their preparation, and the results are shown in Figure 3.4. As the annealing time increases, less H_2S is produced and more hydrogen is released as molecular H_2 . Therefore, the *n*-butane dehydrogenation reaction is another probe of the S content in the catalysts and is consistent with the Zr and S XANES results. Note that the production of H_2S shown in Figure 3.4 (a) mirrors the residue S.

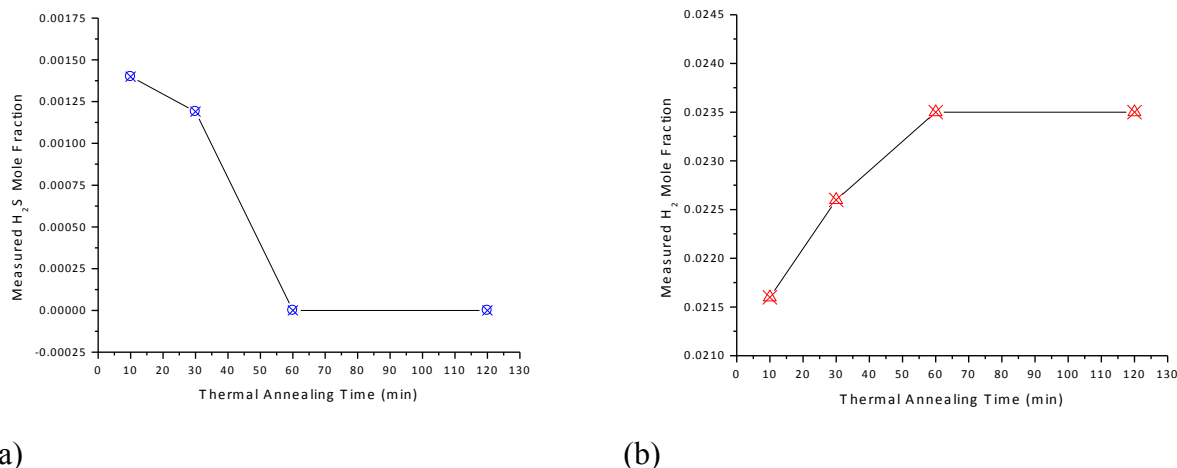


Figure 3.4. Results of *n*-butane dehydrogenation using the S-ZrO₂/MWCNT catalysts annealed for different times – 10 min, 30 min, 1 hr, and 2 hr. (a) Measured H_2S mole fraction during 500~600°C of the reaction vs. annealing time; (b) measured H_2 mole fraction during 700°C of the reaction vs. annealing time.

3.2 Dispersing Carbon Supported Catalysts

We have developed techniques for dispersing carbon supported catalysts in hydrocarbon fuels. Due to oxygen containing groups on defective sites many carbon-based nanomaterials are not directly dispersible in hydrocarbon fuels. To circumvent this problem we have developed a functionalization that produces dispersions that are stable for months.

The first step in the process is to create more oxygen functionalities. This was originally accomplished using nitric acid treatment but because that is not compatible with metal nanoparticle components we are now using ozonation. After oxygen containing groups are in place the carbons can then be made dispersible by reacting hydroxyl groups on the carbon with long chain alcohols. One method of accomplishing this is solution phase sonication. Octanol works to solubilize MWCNT in hexane for months, for jet fuels a larger alcohol such as dodecanol is necessary. These solution techniques have been developed that allow carbon nanomaterials to be dispersed in hydrocarbon fuels. These dispersions are stable for months.

Dispersing the zirconia functionalized MWCNT is more difficult than the other carbon-based nanostructures. This is because the zirconia is grafted to the oxygen containing groups that we use to bind with the alcohol. Once the zirconia is attached to the MWCNT acid cannot be used to add oxygen functional groups. Ozonation, however, is milder and can be used for adding oxygen functional groups to the decorated MWCNT.

4. CATALYTIC OXIDATION OF THERMALLY CRACKED JET FUELS

Charles S. McEnally, William R. Schwartz, Lisa D. Pfefferle*
Department of Chemical Engineering and Center for Combustion Studies,
Yale University,

Aircraft based on scramjet engines would revolutionize air and space travel. Scramjets operate at speeds up to Mach 15 so they would dramatically reduce long distance travel times. Since they use atmospheric air as their oxidizer, they offer greater efficiencies for orbital payloads than rockets. Several severe technical challenges must be overcome to make scramjet airplanes feasible. One of these is structural damage from excessive heating due to friction at the leading edges and engine surfaces. Another issue is that the residence times in the engine are too brief to allow the fuel to burn via conventional combustion.

Fuel-soluble catalysts may solve both of these problems. In current designs the fuel is circulated through the leading edges and engine liners; by promoting endothermic cracking and dehydrogenation reactions, catalysts could greatly increase the heat load absorbed by the fuel. Once the fuel is injected into the engine, the catalyst can promote ignition and thereby reduce the residence time necessary for complete combustion.

The objective of the experiments described in this section was to explore the interaction between these two purposes of the catalyst. The endothermic cracking and dehydrogenation reactions that provide the cooling also change the chemical composition of the fuel; how does this affect ignition of the fuel in the engine? To address this question at the laboratory-scale, we have coupled two model reactors in series, one that simulates the extremely fuel-rich environment of the cooling passages, and one that simulates the fuel-lean environment of the combustor. The product gases from the second reactor were measured with on-line mass spectrometry as functions of the temperatures of the two reactors. Separate or combined with the first effect is the action of a catalyst in the combustion zone itself.

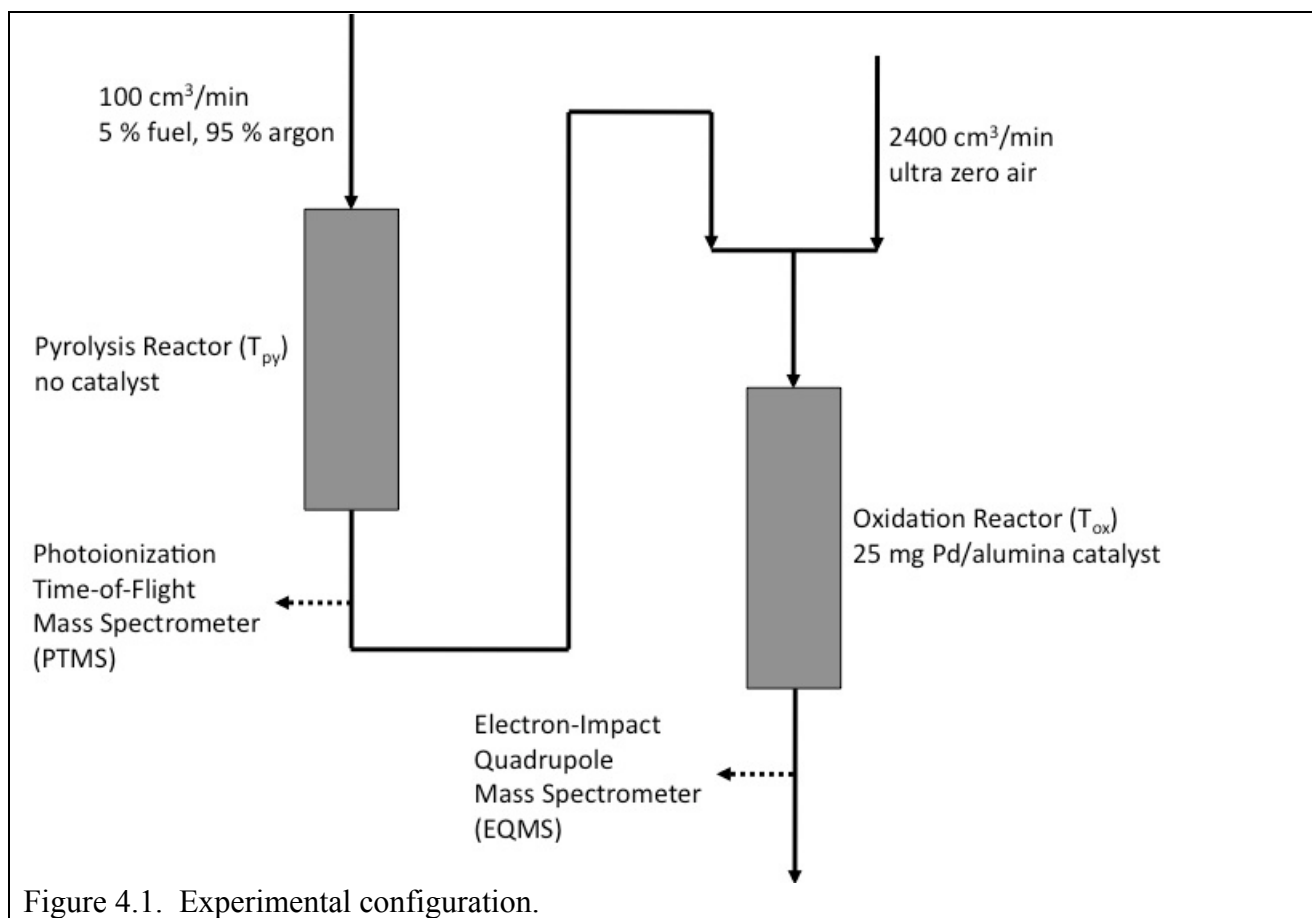


Figure 4.1. Experimental configuration.

4.1 Experimental Methods

The experiment consisted of a pyrolysis reactor and an oxidation reactor coupled in series (see Figure 4.1). In most of the experiments the fuel entering the pyrolysis reactor was n-butane diluted to a mole fraction of 0.05 with argon. N-butane facilitated high-quality data since it is a gas at room temperature, but several liquid fuels were also tested. Leaks in the reactor and its supply lines were identified by helium leak-testing and removed until the oxygen concentration was much less than 100 ppm. The products exiting the pyrolysis reactor were mixed with a large flow of air such that the n-butane mole fraction was reduced to 0.2 %. Ultra zero grade air was used to minimize the carbon dioxide background in the oxidation products. The fuel-air equivalence ratio – defined as the air flowrate necessary for stoichiometric oxidation divided by the actual air flowrate – was >50 in the pyrolysis reactor and 0.009 in the oxidation reactor. The flowrates of gaseous reactants were governed by electronic mass flow controllers, calibrated with soap-bubble meters, while liquid fuels were metered with a syringe pump.

The reactor temperatures were monitored with type K thermocouples and adjusted with annular resistive radiant heaters (Omega Engineering CRFC) under the control of PID temperature controllers (Cole Parmer Digi-Sense). Tests showed that the temperature controllers could maintain the reactor temperatures to within 5 K of the setpoint as long as the PID parameters were properly tuned and temperatures were ramped at less than 20 K/min. A thermocouple at the entrance to the oxidation reactor verified that the temperature of the pyrolysis products entering it was independent of the pyrolysis reactor temperature; thus any changes in oxidation activity are due to changes in the

chemical composition of the initial fuel mixture, not thermal effects. The focus of these studies is to determine the effect of composition of the fuel mixture from the pyrolysis reactor on reactivity in the oxidation zone.

The product gases from each reactor were sampled directly after each reactor and analyzed with on-line mass spectrometry. The pyrolysis reactor products were monitored with a custom-made photoionization/time-of-flight mass spectrometer (PTMS). This instrument uses 118.2 nm (10.5 eV) photons to ionize target gases, which allows it to measure most C3 and larger hydrocarbons. Ion fragmentation is negligible, which makes it ideal for analyzing complex hydrocarbon mixtures such as the effluent from a fuel-rich reactor. The oxidation reactor products were monitored with an electron-impact/quadrupole mass spectrometer (EQMS). This instrument uses 70 eV electrons to ionize target gases, and is ideal for measuring oxidation products such as carbon dioxide and water.

For many of the experiments reported here the oxidation reactor was loaded with 25 mg of a palladium/alumina catalyst. The catalyst was 3 % palladium metal by weight. It was prepared by incipient wetness impregnation from a $\text{Pd}(\text{NO}_3)_2 \cdot 2\text{H}_2\text{O}$ precursor. Additional experiments were performed with several other catalysts as discussed below.

Preliminary tests showed that while certain catalysts (e.g., sulfated-zirconia on carbon nanotubes) were active for pyrolysis, their activity was unsteady due to coking of the catalyst surface. At sufficiently high temperatures (650 to 950 C) thermal reactions were able to crack and dehydrogenate the fuel. Although these reactions also produced coke on the walls of the reactor, this did not affect the product concentrations.

4.2 Results and Discussion

Four sets of experiments are discussed here. In the first set, butane was the fuel, Pd/alumina was used as the oxidation catalyst, and the results were EQMS measurements of products from the oxidation reactor. The second set of experiments used the same reactor conditions, but the diagnostic focus was on PTMS measurements of products from the pyrolysis reactor. The third and fourth sets explored fuels other than butane and oxidation catalysts other than Pd/alumina.

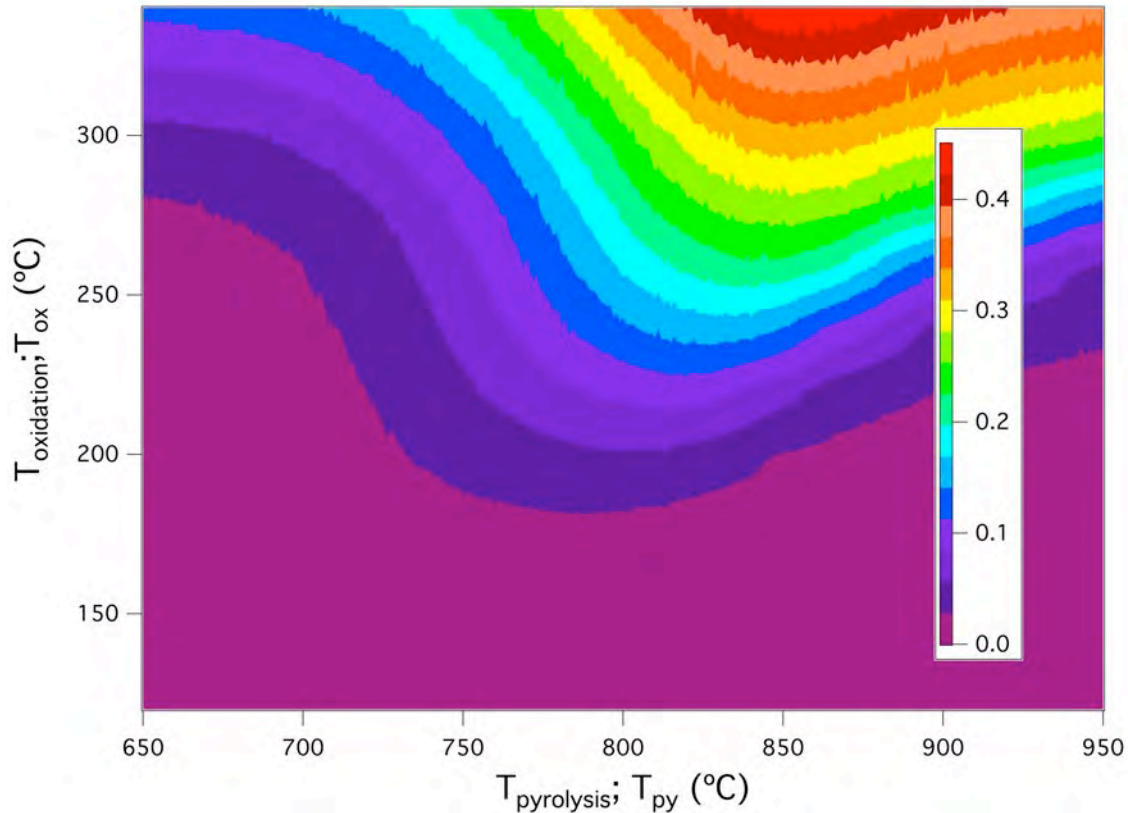


Figure 4.2. Carbon dioxide concentrations measured with n-butane as the fuel. The color scale represents the fraction of the carbon atoms added as fuel that are in the form of CO_2 . The x axis is the temperature in the upstream pyrolysis reactor.

Figure 4.2 shows a contour plot of the carbon dioxide concentrations measured in the oxidation reactor products during the first set of experiments. The concentration units are the fraction of the initial carbon atoms in the form of carbon dioxide; i.e., $Y_{\text{CO}_2} / (4 * 0.002)$ where Y_{CO_2} is the mole fraction of CO_2 in the products, 4 is the number of carbon atoms in each butane molecule, and 0.002 is the concentration of butane in the oxidation products in the absence of reaction. The horizontal axis is the temperature in the pyrolysis reactor (T_{py}) and the vertical axis is the temperature in the oxidation reactor (T_{ox}). The measurements were performed by ramping T_{py} from 650 to 950 C at a series of $T_{\text{ox}} = 120, 140, \dots, 340$ C.

The left side of the graph corresponds to increasing the oxidation reactor temperature under conditions where no reaction is occurring in the pyrolysis reactor. Carbon dioxide begins to appear due to oxidation of butane at about $T_{\text{ox}} = 280$ C. As the pyrolysis reactor temperature increases and the butane begins to react endothermically, the carbon dioxide contours curve to lower values of T_{ox} . This observation shows that the two reactors do interact, and that the interaction is synergistic; i.e., endothermic reactions of the fuel can promote oxidation. Quantitatively, pyrolysis of the fuel reduces the oxidation temperature necessary to achieve a given carbon dioxide concentration by about 100 C. These results indicate that in scramjets, the use of fuel-soluble catalysts that promote endothermic reactions will not only increase the heat load absorbed by the fuel, but also increase the oxidation rate of the fuel in the engine.

Oxidation occurs most readily at about $T_{py} = 775$ C. As the temperature continues to increase in the pyrolysis reactor the oxidation activity begins to decrease.

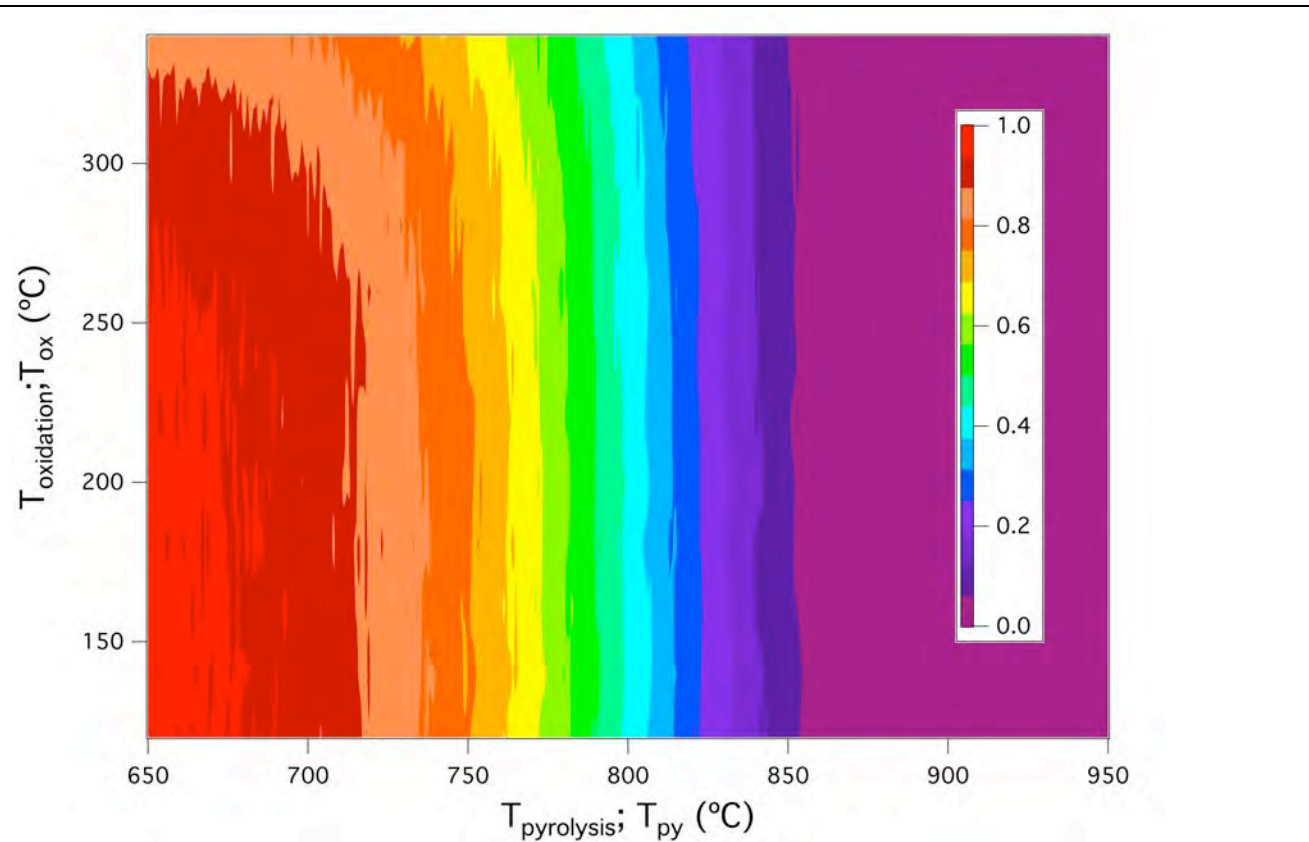


Figure 4.3. Butane concentrations measured with n-butane as the fuel. The color scale represents the fraction of the carbon atoms added as fuel that are in the form of C_4H_{10} . The x axis is the temperature in the upstream pyrolysis reactor.

Figure 4.3 shows concentrations of butane measured in the oxidation reactor products. At the bottom left corner, where both reactors are relatively cold, about 100 % of the carbon is in the form of unreacted butane. As the oxidation reactor temperature increases, the butane concentration stays constant until about $T_{ox} = 280$ C, the same temperature where carbon dioxide begins to increase on the lefthand side of Figure 4.2. As the pyrolysis reactor temperature increases, butane begins to react around 675 C, and is completely consumed by 860 C.

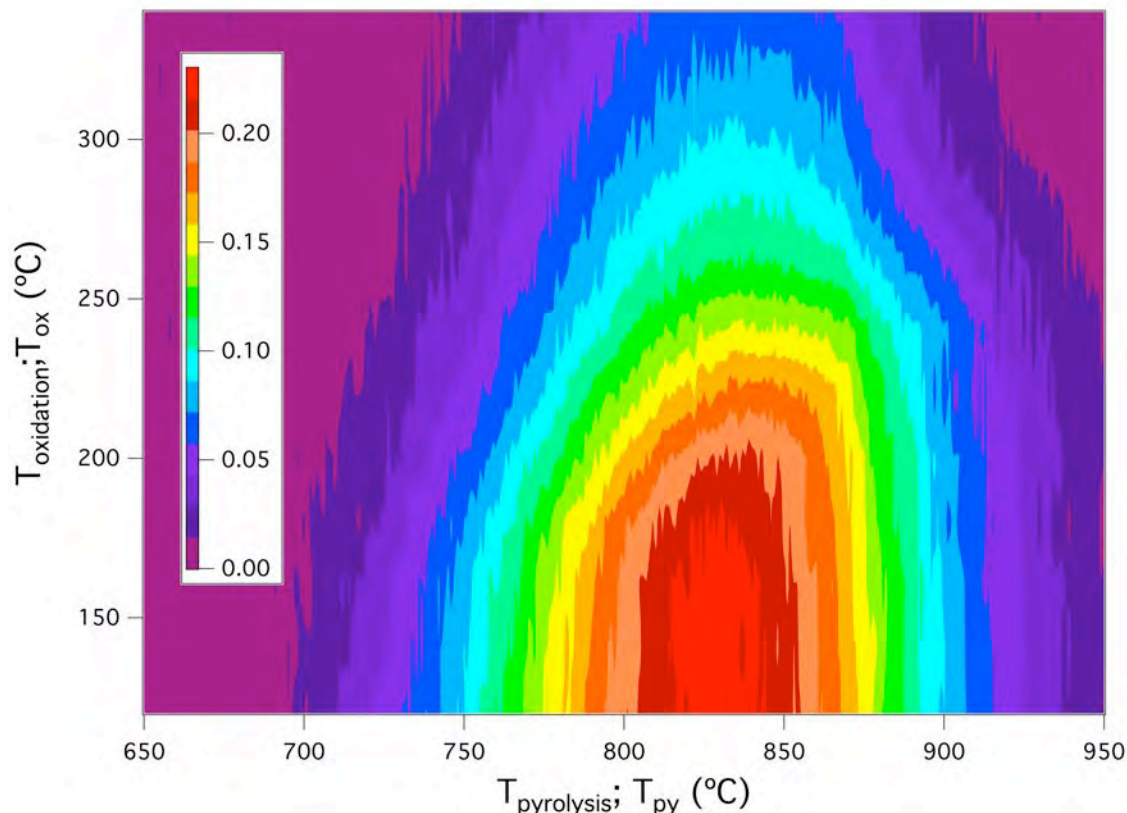


Figure 4.4. Propene concentrations measured with n-butane as the fuel. The color scale represents the fraction of the carbon atoms added as fuel that are in the form of C_3H_6 . The x axis is the temperature in the upstream pyrolysis reactor.

Figure 4.4 shows propene concentrations measured in the oxidation reactor products. Propene is a cracking product of butane that is produced in the pyrolysis reactor but a fuel that is consumed in the oxidation reactor. Thus its concentration is negligible in the bottom left corner when both reactors are relatively cold, increases as the pyrolysis reactor temperature increases, and is consumed when it is present as the oxidation reactor temperature increases. The peak propene concentration occurs at around $T_{py} = 825$ C, which is roughly where carbon dioxide is formed most readily. At this point, about one-quarter of the fuel carbon is in the form of propene. Propene oxidation begins around $T_{ox} = 160$ C, which is much lower than butane (see Figure 4.3). This observation shows that conversion of butane to propene in the pyrolysis reactor will increase the oxidation by converting butane, a relatively difficult fuel to oxidize, into propene which is much easier to oxidize.

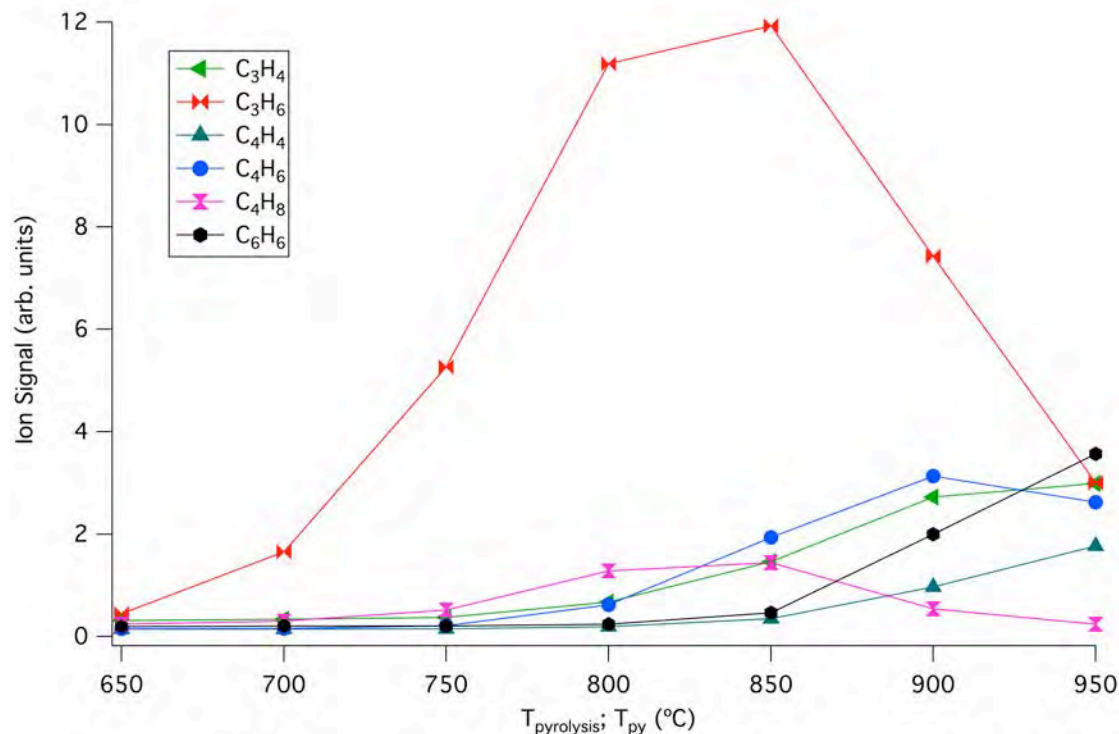


Figure 4.5. Selected products from the pyrolysis reactor measured with the PTMS. The x axis is the temperature in the pyrolysis reactor.

The second set of experiments focused on photoionization measurements of the pyrolysis reactor products in order to gain a greater understanding of how the product distribution changed with temperature. Figure 4.5 shows results for several selected species. Below 800 C the main products are alkenes such as propene and butene. Above 850 C the product distribution shifts towards less saturated species such as C₃H₄ (propyne, propadiene), C₄H₆ (butynes, butadienes), C₄H₄ (vinylacetylene), and C₆H₆ (benzene). Numerous other molecular growth products were detected such as phenylacetylene, naphthalene, etc. Comparison of these results with the carbon dioxide concentrations in Figure 2 shows that as butane is converted into alkenes, the fuel mixture becomes easier to oxidize, but pyrolysis to even less saturated species reduces the oxidation rate to values that are lower than for the alkenes but still faster than for butane. Thus carbon dioxide is produced at the lowest oxidation temperature for an intermediate value of pyrolysis temperature.

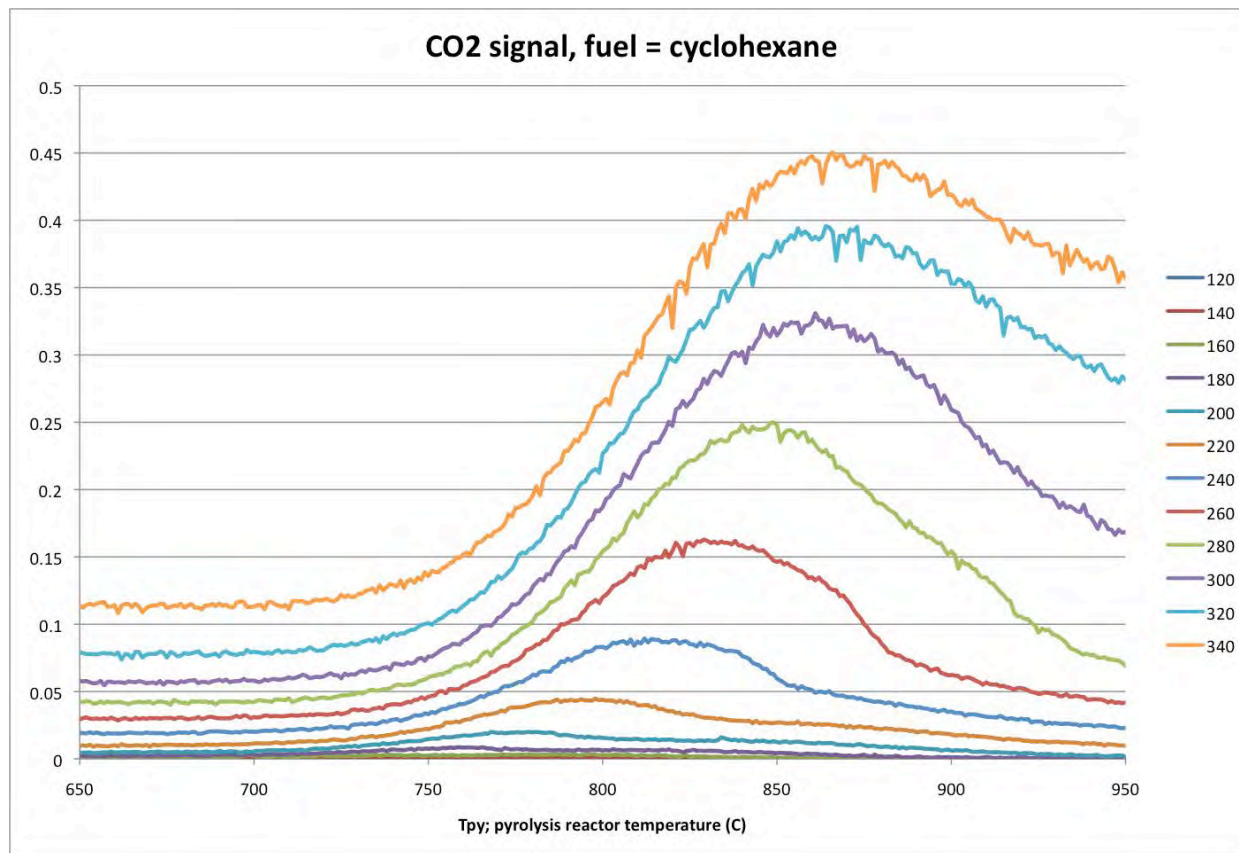


Figure 4.6. Carbon dioxide concentrations measured with cyclohexane as the fuel. The vertical axis represents the fraction of the carbon atoms added as fuel that are in the form of CO₂. The x axis is the temperature in the upstream pyrolysis reactor.

The third set of experiments varied the fuel. In general results similar to those for butane were similar to those observed for a wide range of alkyl fuels. Figure 4.6 shows results for cyclohexane: as the pyrolysis reactor temperature increases, the carbon dioxide concentration at a given oxidation temperature increases. Similar results were observed for n-hexane, 2,3-dimethylbutane, methyl tert-butyl ether, and ethanol. This suggests that endothermic reactions will increase the oxidation rate for all of the types of compounds found in aviation fuels. Another interesting observation is that there is an optimal product mix to accelerate oxidation in the combustion zone.

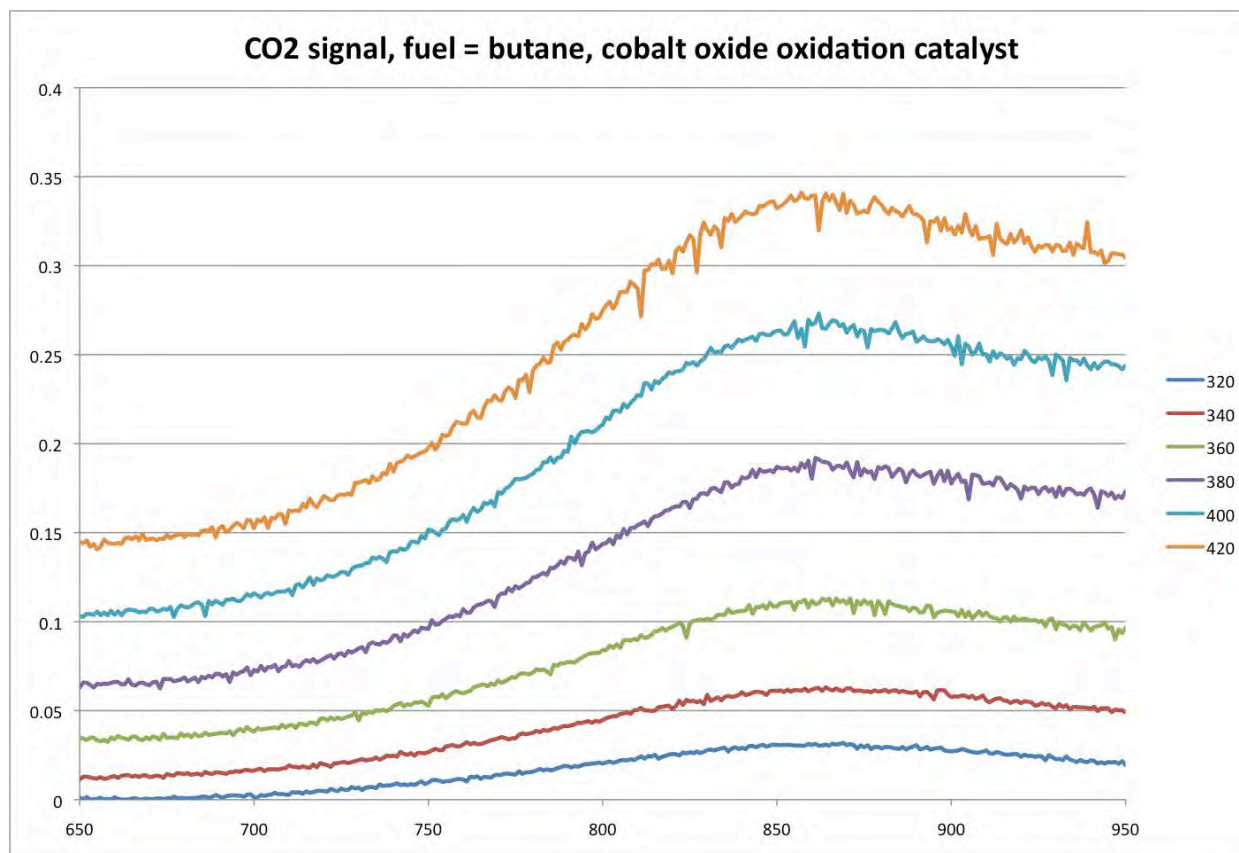


Figure 4.7. The x axis is the temperature in the pyrolysis reactor. Carbon dioxide concentrations measured with butane as the fuel and a cobalt oxide/alumina catalyst in the oxidation reactor. The vertical axis represents the fraction of the carbon atoms added as fuel that are in the form of CO₂ at different oxidation temperatures shown to the right for each curve. The horizontal axis is the pyrolysis temperature in the upstream reactor.

Finally, the fourth set of experiments varied the catalyst in the oxidation reactor. Results similar to those for the Pd/alumina catalyst were observed for a variety of catalysts, including a cobalt oxide/alumina catalyst (Figure 4.7), a rhodium/alumina catalyst, an iron oxide/alumina catalyst, and a catalyst with sulfated-zirconia and palladium supported on carbon nanotubes.

5. Combining practical catalysts with model catalyst and in-situ analysis

Stefan Vajda (lead PI), and the entire team

5.1. Size and Support-Dependent Reactivity of Subnanometer Cobalt Catalysts with CO and H₂: A combined GIXAS, GISAXS and TPRx Study

The thermal stability and changes in the oxidation state during the Fischer Tropsch (FT) reaction was investigated on subnanometer size-selected cobalt clusters deposited on oxide and carbon-based supports. The model catalyst systems were prepared by deposition of size selected cobalt clusters on various metal oxides (Al₂O₃, MgO) and ultra-nanocrystalline diamond (UNCD) supports. The size, oxidation state and reactivity of the supported cobalt clusters were investigated by temperature programmed reaction (TPRx) combined with *in-situ* grazing-incidence X-ray absorption and scattering (GIXAS and GISAXS).

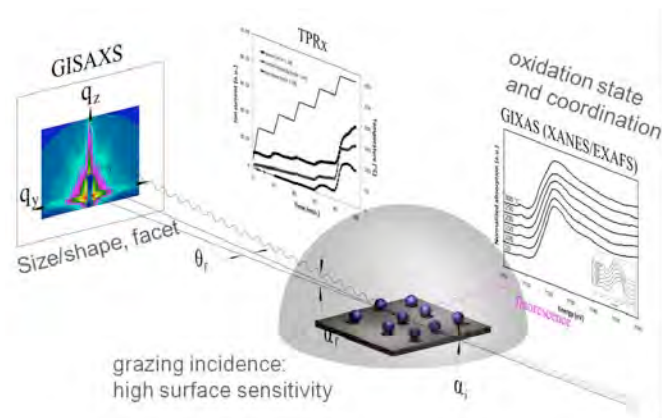


Figure 5.1. Schematics of the combined GISAXS/GIXAS/TPRx experiment.

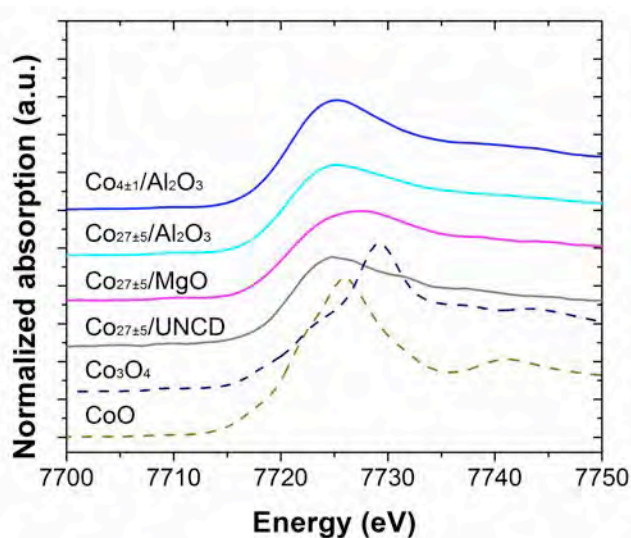


Figure 5.2 XANES of Co_{27±5} clusters deposited on various supports. Reference spectra of bulk CoO and Co₃O₄ are also shown for comparison.

5.1.1 Experimental

As a support material for the catalysts, we used ~1 nm thick amorphous alumina and MgO, films prepared by atomic layer deposition (ALD) on the top of a naturally oxidized silicon wafer ($\text{SiO}_2/\text{Si}(100)$). The UNCD support was purchased from Advance Diamond Technologies (25 Aqua DoSi) and used as received. The size-selected cluster-based cobalt catalysts were prepared by depositing a narrow size-distribution of cobalt clusters generated in a laser vaporization cluster source. After deposition, the samples were exposed to air for an extended period of time, which lead to the formation of cobalt-oxide species, as determined by GIXAS. The experiments were performed in a home build *in situ* GISAXS/GIXAS/TPRx reaction cell at the 12-ID-C beam-line of the Advanced Photon Source (see schematics in figure 5.1.) scattering. Reactivity, X-ray scattering and X-ray absorption data were collected as a function of reaction temperature and time. The concentration of CO and hydrogen in the feed was 1 and 2 % respectively, seeded in helium. The reaction cell was operated in a continuous flow mode at 800 torr pressure and 30 sccm (standard cubic centimeters per minute, $\text{cm}^3/\text{min.}$) of gas flow. The catalyst tests were carried out at temperatures from 25 to 225 °C and the products monitored using a differentially pumped mass-spectrometer (Pfeiffer Prisma).

5.1.2 Results and discussion.

No change in cluster size, as monitored by GISAXS, was observed under reaction conditions in reaction times of up to 4 hours, which confirmed that the sub-nanometer cobalt clusters were resistant to sintering on all supports used in this study which was also demonstrated in dehydrogenation reactions.

Figure 5.2 summarizes GIXAS spectra of the as prepared cobalt cluster-based catalysts collected under vacuum at room temperature and spectra of bulk CoO and Co_3O_4 reference materials. From comparison with reference spectra, we conclude that the XANES of as synthesized cobalt clusters closely resembles the CoO phase. Presumably, the main fraction of cobalt species in the samples is present as a CoO dominant phase, mixed with a fraction of Co_3O_4 phase influenced by the size of the clusters and composition of the support. A slight shift of the spectra and broadening changes of the XANES area feature were observed during the *in-situ* experiment, which may reflect a development of a more complex oxide system. In passing we note that potential charge transfer between the clusters and the support and/or structural changes in clusters caused by the binding of ligands and temperature may be reflected in the spectra as well.

Figure 5.3 shows *in situ* GIXAS results obtained for $\text{Co}_{4\pm1}$ clusters supported on alumina (Fig. 5.3a) and for set of three samples of $\text{Co}_{27\pm5}$ clusters supported on alumina (Fig. 5.3b), magnesia (Fig. 5.3c) and UNCD support (Fig. 5.3d) as a function of temperature during the reaction. First, it is evident that at 25 °C the clusters maintain their average oxidation state very close to that observed under vacuum conditions for as prepared cluster samples (cf Figure 5.2). Second, in the case of the $\text{Co}_{27\pm5}$ clusters, XANES obtained at 225 °C exhibited a slight white line shift toward higher energy, accompanied by a line broadening, observed in the spectra of all three samples. Among the spectra of $\text{Co}_{27\pm5}$ clusters, the spectra of UNCD supported clusters exhibited a more significant shift toward lower energy during the reaction, which most likely indicates a partial reduction of the clusters under working conditions. Third, the most dramatic change in the XANES feature was observed for alumina supported $\text{Co}_{4\pm1}$ clusters - at 225 °C the spectrum of $\text{Co}_{4\pm1}$

becomes alike the spectrum of $\text{Co}_{27\pm5}$ clusters (see Fig. 5.3a and 5.3b), thus indicating high similarity in the chemical state of the most active species at this temperature.

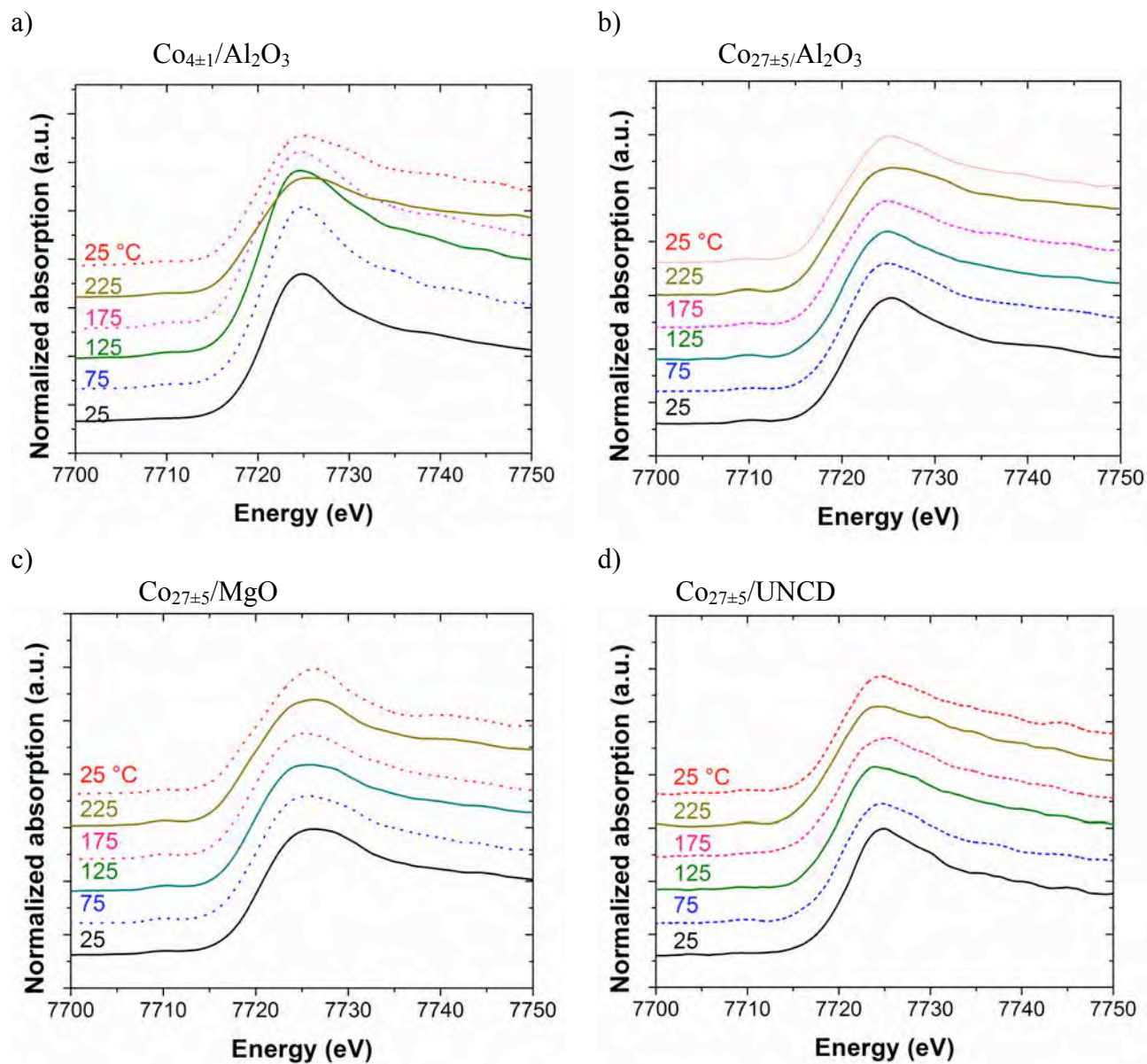
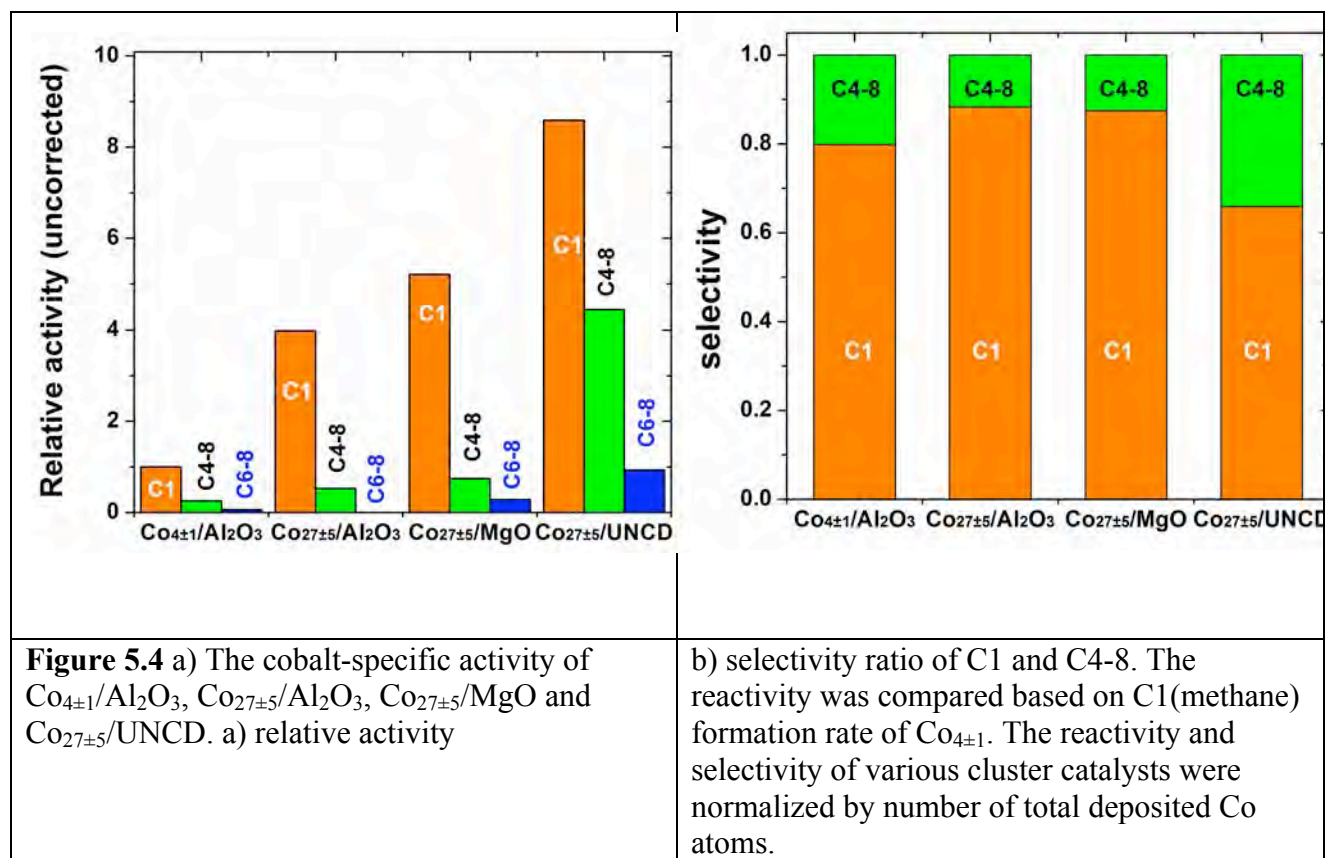


Figure 5.3. *in situ* XANES of a) $\text{Co}_{4\pm1}$ clusters on Al_2O_3 , and $\text{Co}_{27\pm5}$ clusters on b) Al_2O_3 , c) MgO and d) UNCD at, from bottom to top, 25 (at start), 75, 125, 175, 225 and 25 °C (after reaction). 30 sccm of mixed gas (H_2 : CO : He = 1 : 0.5 : 98.5) was continuously flowed during the reaction.



A comparison of the activity and selectivity obtained at 225 °C, for the cluster-based samples with identical metal loading are shown in Figure 5.4a and Figure 5.4b, respectively, as a function of clusters size and support. The overall activity increases from Co_{4±1}/Al₂O₃ to Co_{27±5}/Al₂O₃, Co_{27±5}/MgO and Co_{27±5}/UNCD. Alumina supported Co_{27±5} catalyst exhibits the highest relative methane yield, with a methane selectivity of ~90 % and a C₄₊ selectivity of ~10 %, while not producing a detectable amount of C₅₊ products.. The highest fraction, approximately 35% of C₄₊ chain was grown on UNCD-supported Co_{27±5} clusters, which underlines the role of support in the performance of the subnanometer size catalysts. The formation of methane and C₂₊ products indicates an efficient dissociation of hydrogen on the subnanometer cobalt clusters. The higher selectivity to methane under the applied reaction conditions might also indicate a lower abundance of the sites active in chain growth (such as low density of sites for co-adsorption of a higher number of CO molecules with respect to hydrogen), resulting in more carbon species at the surface that become fully hydrogenated to methane. This hypothesis is illustrated by the comparison of the effect of cluster size on the fraction of methane produced on alumina-supported Co_{4±1} and Co_{27±5} clusters. The smaller cobalt clusters Co_{4±1} showed much lower activity compared to their bigger counterparts, however produced a higher fraction of C₂₊ products than Co_{27±5}. The lower activity of Co_{4±1} clusters can be caused by limited adsorption sites for both H₂ and CO molecules and/or strong binding of reactant and reaction intermediate on the smaller clusters, which may inhibit the reaction.. This means that only small (if any) portion of the Co_{4±1} clusters might be sintered to form nanoparticles at higher temperature. It is important to note that the experimental setup in this study used relatively low pressure and short contact time compared to real catalytic system, which could be in part responsible for the higher selectivity toward low molecular weight hydrocarbons. In the case of nanometer size cobalt particles, the lower reactivity and higher methane selectivity of small

Co particles compared to larger ones in the FT reaction is mainly attributed to the strongly bonded CO molecules and higher coverage with hydrogen, such as in a previously reported study of carbon fiber supported cobalt catalysts.

The probability of chain growth (α) on sub-nanometer cobalt clusters was calculated from the mass fragment pattern analysis based on the ASF distribution model, and yielded values within a range of $\alpha = 0.3 - 0.45$. The reactivity and selectivity of the $\text{Co}_{27\pm5}$ clusters vary strongly with the composition of the support. The reactivity orders as $\text{UNCD} > \text{MgO} > \text{Al}_2\text{O}_3$. In addition to be the most active catalysts, the UNCD supported $\text{Co}_{27\pm5}$ clusters also exhibit the highest selectivity toward high molecular weight hydrocarbons. On the other hand, alumina supported $\text{Co}_{27\pm5}$ clusters exhibit the lowest reactivity among all $\text{Co}_{27\pm5}$ samples studied, as well as the lowest selectivity selectivity towards higher molecular weight hydrocarbons. It was surprising to observe a lower selectivity of alumina supported cobalt clusters since it is known that nanosized cobalt is a good FTS catalyst in commercial applications. The lower selectivity towards higher hydrocarbons of sub-nanometer size clusters observed in the present study may have various origins: 1) strongly size-dependent FT properties of cobalt (oxides), 2) differences in pressure and flow conditions, and 3) pronounced support effect in this quantum regime. Atomic clusters are known to be very sensitive to metal-support interactions. Therefore, the observed higher reactivity and high C_{4+} selectivity of UNCD supported $\text{Co}_{27\pm5}$ clusters indicate that the performance of sub-nanometer FT catalysts can be fine-tuned by the proper choice of the composition of the support material. Weaker cluster-support interactions may result in less methane formation and to an increased yield in the production of higher hydrocarbons.

5.1.3 Conclusion

Well defined sub-nanometer cobalt clusters prepared by cluster ion beam deposition methods have been used to study size and support effects in the Fischer-Tropsch/methanation reaction. The chemical state of the nanoparticles and its changes occurring during reaction were investigated using *in situ* XANES at atmospheric pressure and temperature up to 225 °C. The results indicate that 1) performance of sub-nanometer particles can be controlled via the size of the clusters, 2) metal support interaction offers an additional key to control activity and selectivity in FT synthesis, and 3) new, carbon based supports could play important role in future production of fuels from syngas. Under applied reaction conditions, the 27-atom cobalt clusters are by more than order of magnitude more reactive than 4-atom clusters, while UNCD-supported 27-atom clusters are more than two times more active than alumina supported ones. XANES results suggest that controlling the electronic structure of sub-nanometer cobalt clusters via cluster-support interactions could lead to a fundamentally new level of understanding of the function of (sub)nanoscale materials, not observed at the nano- or microscale. This is being written up for publication (see draft list below).

5.2. Oxidative Dehydrogenation of Cyclohexene on Size Selected Subnanometer Cobalt Clusters: Improved Catalytic Performance via Structural Fluxionality of Cluster-Assembled Nanostructures.

The rate determining step in the dehydrogenation of cyclohexane to benzene appears to be the dehydrogenation of the cyclohexene intermediate, which requires specific orientation of the adsorbed cyclohexene relative to the catalyst surface. Model catalyst systems were prepared by deposition of size selected subnanometer $\text{Co}_{27\pm4}$ clusters on various metal oxide supports (Al_2O_3 , ZnO and TiO_2 and MgO). The oxidation state and reactivity of the supported cobalt clusters were

investigated by temperature programmed reaction (TPRx) and *in-situ* grazing incidence X-ray absorption (GIXAS) during oxidative dehydrogenation of cyclohexene, while the sintering resistance monitored with grazing incidence small angle X-ray scattering (GISAXS). The gas reactants used were 4000 ppm cyclohexene in helium and 99.9 % oxygen, and the ratio for cyclohexene and O₂ was kept 1:10 by preparing the mixture.

5.2.1 Results and discussion

The normalized XANES spectra (Co-K edge) of Co clusters supported on MgO and Al₂O₃ are presented in Figure 5.5 as a function of reaction

temperature. The sample was measured in helium background at room temperature and then in cyclohexene and oxygen mixture at indicated temperatures. The XANES spectra (Co-K) of as the as prepared sample and the spectra in reaction gas environment up to 200 °C are practically similar to each other and show a broad XAS feature. Presumably, the main part of cobalt species in the samples is present as a CoO dominant mixed phase of CoO and Co₃O₄ under applied reaction conditions. A sudden change occurs at 250 °C in the

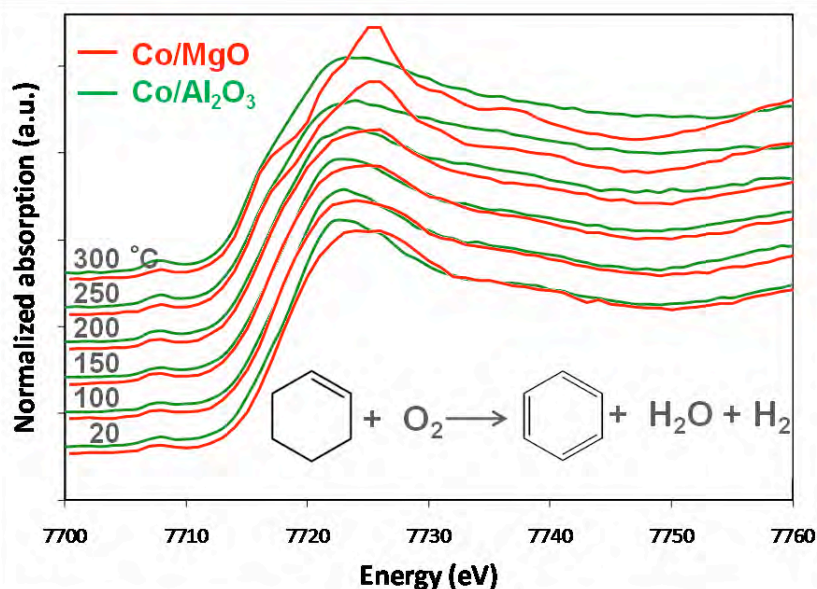


Figure 5.5. Co K-edge XANES spectra of Co/MgO (red) and Co/Al₂O₃ (green) from up to bottom in the order of reaction temperatures, 20, 100, 150, 200, 250 and 300 °C, respectively. Cyclohexene and oxygen in He buffer at total pressure of 800 torr.

Co/MgO sample, which includes forming a sharper peak at 7727 eV and distinct two shoulder feature at lower energy. The changes are more pronounced at 300 °C, and no further change were observed with 30 min extended time, which indicates this form is stable at the temperature. The well developed new features were clearly observed in Co/MgO sample starting at 250 °C, while the Al₂O₃ supported cobalt shows only a broadening in white line feature and slight change near the edge region, which further develops with increasing temperature. The change in Co/MgO sample indicates transformation to high oxidation state, Co₃O₄, or surface alloy like Co_xMg_{1-x}O with the MgO support. Presumably, at high temperature cobalt and MgO form a mixed oxide which drives oxidation state and structural changes. MgO is known to be a non-reducible oxide, and our concurrent study shows that ZnO, TiO₂, and Al₂O₃ supported cobalt catalysts do not show similar change in cobalt oxidation state under identical reaction conditions. A subtle change occurs during the cooling ramp, lower energy shoulder feature diminished, and the cobalt feature returns close to Co₃O₄, which indicates that Co_xMg_{1-x}O formed at 300 °C may be stable only at high temperature. The Co-K edge feature of Co_xMg_{1-x}O has been reported to be very sensitive to the stoichiometry in Co_xMg_{1-x}O. Quantitative measurements of each mixed oxide

state is greatly complicated since CoO, Co₃O₄ and Co can coexist, and the bulk reference spectra do not necessarily represent subnanometer clusters due to: a) intrinsic electronic structure difference between nanoclusters and bulk state and b) strong interaction between small clusters and support oxides.

In situ GISAXS (see figure 5.6) shows clear difference between the evolution of the samples prepared on various supports. Cobalt clusters on Al₂O₃, TiO₂ and ZnO do not reveal any significant changes in particle size under the reaction condition, thus providing evidence about the sintering-resistance of the cobalt clusters during two hours of reaction. Figure 5.6b shows temperature dependent line cut (horizontal) profiles and typical 2D-GISAXS image of Co/MgO sample. At room temperature, GISAXS represent dominant substrate scattering with a little contribution from cobalt nanoparticles, which indicates that the clusters are in subnanometer size range of their as-prepared state. A slight change in the GISAXS pattern is noticeable in the small q range ($\sim 1 \text{ nm}^{-1}$) at 250 °C.

However, the most significant change is observed at 300 °C, which indicates formation of nanostructure with very sharp size distribution. The 2-D linecut data has been fitted to particle size and distribution as shown in Figure 5.6c. For the GISAXS data fitting, supported island model with log normal distribution has been used with FitGISAXS program. At 300 °C, the nanoclusters transform into $\sim 2.5 \text{ nm}$ size nanostructures with a narrow size distribution. More interesting features appeared when the sample was cooled down to room temperature. The average particle size changed to 1.8 nm with a broad size distribution. This sequence of changes cannot be simply interpreted by thermal sintering because of reversible change during the cooling cycle and unique feature development only on Co-MgO system. Since the MgO is a non-reducible support, there is no strong electronic effect between cobalt and MgO, which could facilitate chemical transformation from CoO to other form of oxides.

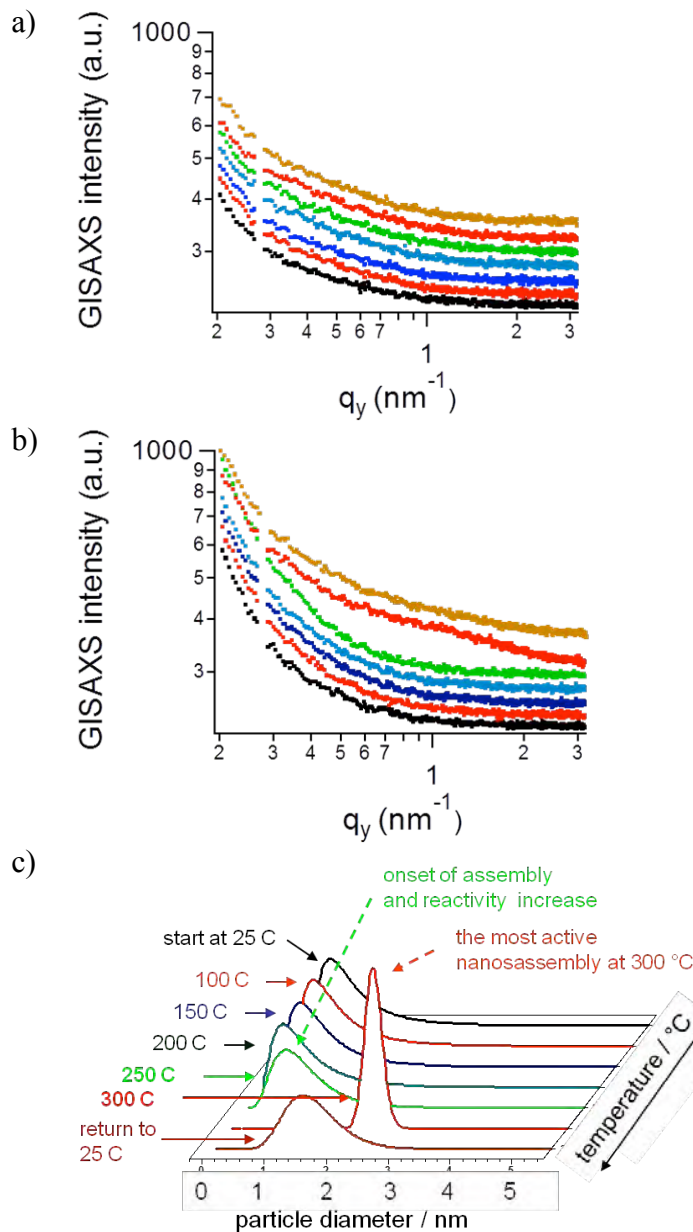


Figure 5.6. GISAXS intensity (horizontal line cut) change during the heating cycle, from the bottom 20, 100, 150, 200, 250, 300 and 20 °C (after reaction) respectively for (a) alumina-supported and (b) magnesia-supported cobalt clusters; the spectra are offset for clarity. (c) evolution of particle/nanoassembly size distribution of the magnesia-supported clusters during the reaction.

Presumably, well dispersed subnano sized cobalt clusters can be transformed to Co-Mg-O solid solution rather easily in oxidation environment at high temperature and the preformed metastable solid solution can be reversibly transformed to CoOx-MgO system at low temperature. It is essential to provide proper two or three fold binding sites, for cyclohexene to transform to benzene. Unlike the other metal oxides supported clusters, Co/MgO has a highly fluxional structure and forms 2-3 nm size particles at 300 °C during the reaction, which presumably adapts to provide flat binding sites for cyclohexene and other reaction intermediates during dehydrogenation to benzene. Size effect on cyclohexene dehydrogenation on Pt nanoparticles has been reported with various particle sizes. It shows that the rate of dehydrogenation of cyclohexene to benzene decreases monotonically over the particle size range from 1 to 9 nm. It clearly shows that the size is critical for the reaction rate while the optimum size and structure of the active site could be strongly dependent on the system.

Per cobalt atom temperature-dependent turnover rates of benzene formation on Co/MgO, Co/Al₂O₃, Co/TiO₂ and Co/ZnO are shown in Figure 5.7. Activity increased significantly at 250 °C which corresponds to the onset of the change of the XANES feature shown in Figure 5.5, thus providing a direct correlation between the change in the nature of the catalysts and its reactivity

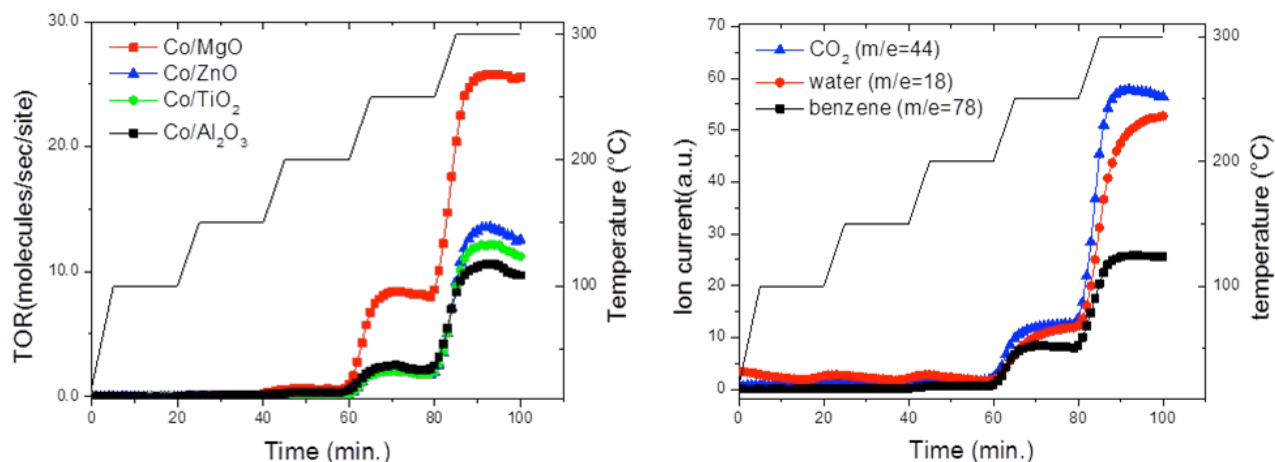


Figure 5.7. a) TPRx results of cyclohexene oxidative dehydrogenation on Co/MgO, Co/ZnO, Co/TiO₂, and Co/Al₂O₃. The straight line shows the temperature profile ramping from 20 to 300 °C, stepwise. Evolution of benzene is shown as turnover rate per cobalt atom. b) TPRx profile of benzene, water and carbon dioxide evolution on Co/MgO sample during the oxidative dehydrogenation of cyclohexene. Cyclohexene and oxygen in He buffer at total pressure of 800 torr.

Overall turnover rates of benzene formation on nanocluster catalysts are in the range between 10 to 25, which is comparable to non-oxidative cyclohexene dehydrogenation on Pt catalysts. The reactivity of Co/MgO is about 2- 3 times higher than that of other supported cluster catalysts at 300 °C. Also, it is worth to note that the activity of Co/MgO shows higher stability during the isothermal conditions than Co/Al₂O₃ at 300 °C. Production of water and carbon dioxide was also observed. The relative ratio between CO₂ and benzene is 3 to 1. There are no KA oil related products observed during the reaction in any of the subnanometer cobalt cluster based catalysts. Most of side products are CO₂ and water by total oxidation of cyclohexene. In addition to main reaction products (benzene, CO₂ and water), a trace amount of cyclohexadiene is also observed at ~250 °C, but disappears at higher temperatures at which benzene formation becomes more

dominant. Presumably, electronically localized nature of small size cobalt cluster suppresses formation of radical intermediates for oxidation of cyclohexene. Also, a relatively stable adsorption complex which is formed between cyclohexene and cobalt catalyst may be less favorable for radical formation than one from cyclohexane and cobalt. Oxidative dehydrogenation studies on cyclohexene are scarce. Recently published results based on TiO₂ supported Au, Pd and Au-Pd catalyst show high activity at relatively low temperatures; ~ 99% benzene selectivity and 100% conversion at 150 °C. On the contrary, under the same conditions over Co-ZSM5, the cyclohexane conversion becomes significant above 700K and increases by increasing of temperature to 45% at 880 K. The main products at low conversion are CO_x whereas at higher temperature benzene becomes the most important product.” Vanadia based catalyst has been reported for ODH of cyclohexane with relatively high reaction temperature (> 400 °C). It is well known that Co-Mg-O solid solution can be formed relatively low temperature (< 100 °C) and its higher concentration of suprafacial oxygen or weakly chemisorbed oxygen species result in Co-Mg-O solid solution as a good catalyst for hydrolysis of glycerol, N₂O catalytic decomposition, CO₂ reforming of CH₄ and ethanol steam reforming although the reducibility of cobalt oxides was greatly decreased in the Co₃O₄/MgO precursor.

5.2.2 Conclusions

Our results show that the MgO supported cobalt catalyst has a low light up temperature (> ~200 °C) and it maintains high reactivity at 300 °C. The change of the nature of on various oxide surfaces, along with their ability of subnanometer clusters to form fluxional, highly active nanostructures that adapt their morphology to offer the optimal reaction pathway, can represent key elements for high reactivity as well as selectivity. The most interesting aspect behind the high activity of MgO supported cobalt catalyst is the formation of a cluster-based nanoassembly during the culmination of the reaction, accompanied by significant change of the oxidation state of cobalt. The turnover rates can make such materials compositions as attractive alternatives to precious metal based dehydrogenation catalysts. The Co₃O₄- and solid oxide like mixture formation on MgO support, accompanied with the assembly of subnanometer clusters were observed. The assembly yielded a highly fluxional nanostructure, with 1) morphology of the nanoassembly and 2) chemical state of cobalt optimally adapted to promote the dehydrogenation path.

Earlier work on the effect of Pt particle size on the selectivity of cyclohexane dehydrogenation comparing both size selected clusters with practical nano Pt supported on SWNT catalysts. This work also included first principles calculations. Good agreement was observed between the cluster, practical catalyst and modeling results for reaction selectivity as a function of catalyst size. This work is described in a paper draft included here as Appendix I.

6. Computational Studies Matthew Neurock

Department of Chemical Engineering, University of Virginia

A. Catalytic Dehydrogenation of Model Alkane Intermediates over Nanometer Supported Metal (Pt and Co) Cluster Catalysts (Qiang Qian and Matthew Neurock)

Over this past year we have extend our theory and simulation efforts in modeling the catalytic dehydrogenation over nanometer Pt and Co clusters carried out in direct collaboration with Stephan Vajda (Argonne), Lisa Pfefferle (Yale), Gary Haller (Yale), and Maria Flytzani-Stephanopoulos (Tufts). Previously we showed that for metal nanoparticles between 1-5 nm the catalytic activity and selectivity can be markedly influenced by the nature of the support and the methods of

synthesis as they influence the particle size.⁹ The particle size effects on the rates and selectivities for these particles (1 nm-5 nm) were found to be solely due to the differences in the number of terrace, edge and corner sites. In this past year we have extended these studies to subnanometer particles, i.e. clusters, where the band-structure of the metal disappears and one needs to worry about quantum size effects. Previous experimental studies of gas phase reactivity of methane over neutral Pt_n ($n \leq 24$) clusters in a fast flow reactor showed a decrease in the reactivity of methane with increasing cluster size, with a dramatic drop in reactivity at Pt_6 and a jump at Pt_{11-12} .¹⁰ Similar studies were carried out for the dissociative adsorption of D_2 as D-D bond is thought to behave similarly to C-H bond, over a range of different Co clusters up to 28 atoms up (Co_n ($n \leq 28$)) in a fast-flow reactor. The results showed a minimum reactivity for Co_6 and a maximum reactivity for Co_{16} with a nearly monotonic increase between $n=6$ to $n=13$.¹¹

First principle density functional theory (DFT) calculations were used to examine the activation of the secondary C-H bond of propane at different sites of Pt_n ($n=4-9, 13$) and Co_n ($n=4-10, 12-14$) subnanometer clusters. Within the size range of our study, we found that C-H bond activation barriers were lower at the coordinatively-less saturated metal sites. For Pt_n clusters with metal sizes of 4 to 9 atoms (see figure 6.1a), the C-H bond activation barrier increased with increased size of the cluster, which is consistent to the experimental results carried out with methane as a feed, which showed a decrease in activity with increased Pt cluster size¹⁰. For Co_n clusters with sizes that range from 6 to 13 atoms (see figure 6.2a), the C-H bond activation barrier decreased monotonically with the increase in size, which is also in agreement with experimental results for D_2 activation over Co_n clusters¹¹. The differences between Pt_n and Co_n , are intriguing and we are currently carrying out simulations to help understand why they change in opposite ways with cluster size.

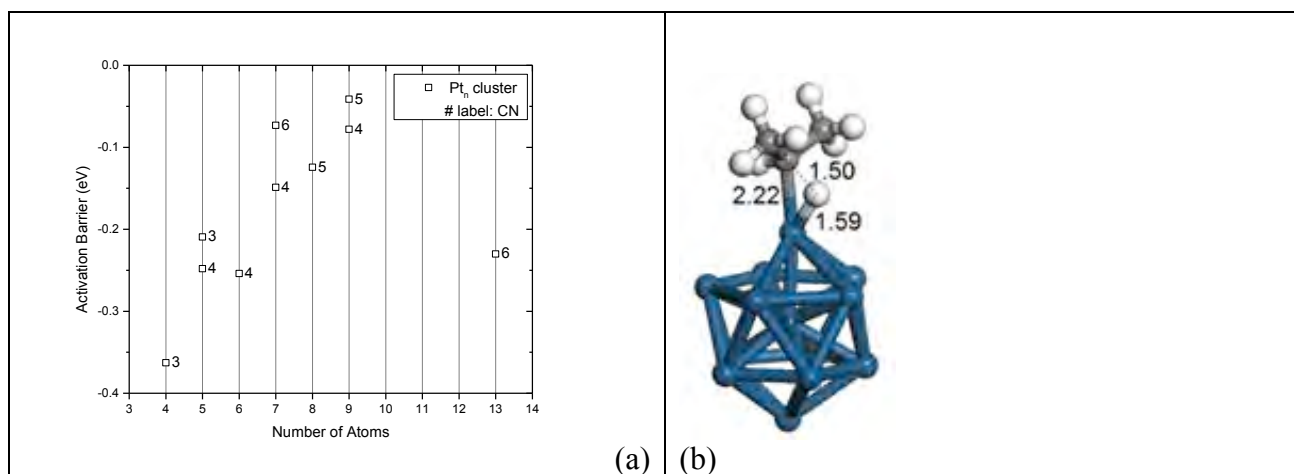


Figure 6.1. (a) DFT calculated apparent activation barriers for secondary C-H bond activation of propane at specific metal sites with different coordination numbers (labeled besides each square) on Pt_n(n=4~9,13) clusters. (b) Transition state of propane first C-H bond activation on Pt₁₃.

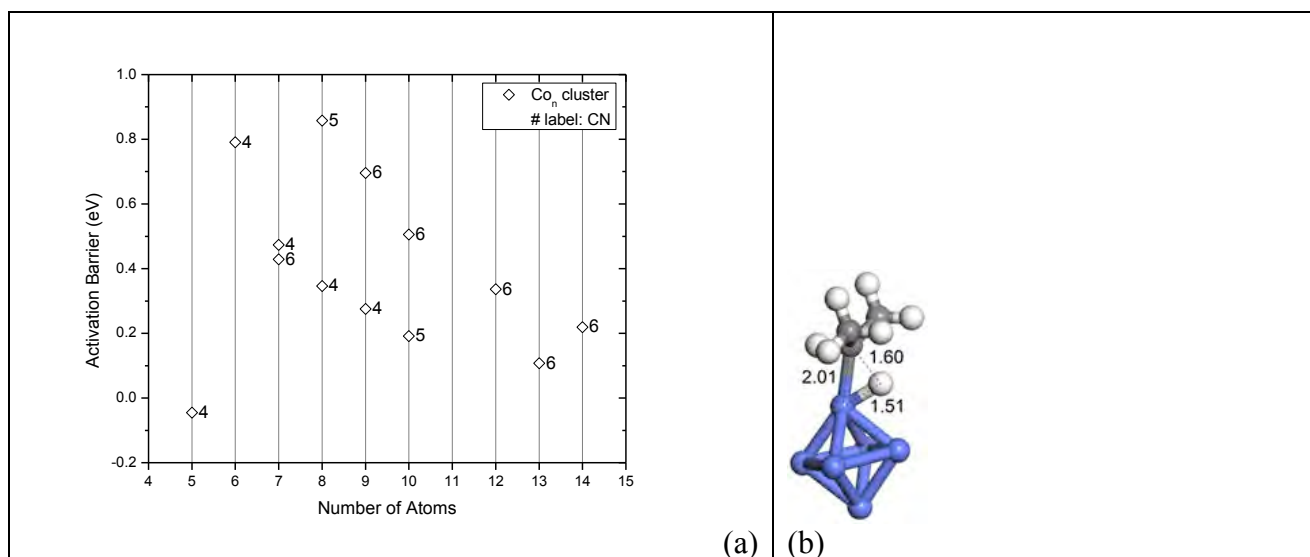


Figure 6.2. (a) DFT calculated apparent activation barriers for the secondary C-H bond activation of propane at specific metal sites reaction centers with different coordination number (labeled besides each square) on Co_n(n=4~10,12~14) clusters. (b) Transition state of propane first C-H bond activation on Co₆.

B. Propane and Cyclohexane Oxidative Dehydrogenation over Au Supported on Cobalt Oxide Surfaces

In previous collaborative studies with Vajda (Argonne) and Flytzani-Stephanopoulos (Tufts), we showed the unique activity of Co₃O₄ derives from its weakly held O* surface sites that readily carry out hydrogen abstraction reactions.¹² In more recent studies, Vajda and Flytzani-Stephanopoulos showed that doping Au into Co₃O₄ significantly improved its catalytic activity for carrying out the oxidative dehydrogenation of cyclohexane. In addition, they showed that while 12 nm Co₃O₄ particles alone deactivate over time, there is appreciable deactivation over the Au doped Co₃O₄ particles.

We carried out a number of density functional theory calculations in order to examine the influence of Au on Co_3O_4 in the oxidative dehydrogenation of propane and cyclohexane. The Au particles were modeled with a 3×3 Au nanorod as shown in Fig. 6.3. Such models have been used successfully in the past to model the Au/ TiO_2 interfaces. As illustrated in 6.3, the Au nano-rod can transfer electrons to the Co_3O_4 support upon adsorption giving rise to charge localized near the gold-oxide interface. The increased electron density in the interfacial Co^{octa} cation weakens the Co-O bond and thus increases the O sites affinity for H. This increase in the H-affinity at the interfacial O site results in a lower activation barrier for the initial C-H bond activation of cyclohexane at Au- Co_3O_4 interface (see 6.4a,b). The partially reduced Co^{octa} cation at the interfacial O vacancy also aids in the adsorption and activation of O_2 at this site and the formation of reactive mono-oxygen surface species. (see 6.4c,d) The weakly bound O_2 and O species that form at the interface can subsequently readily activate the C-H bonds of propane. The results allow us to establish a more fundamental understanding of the experimentally observed reactivity increase that occurs with the addition of Au to Co_3O_4 .

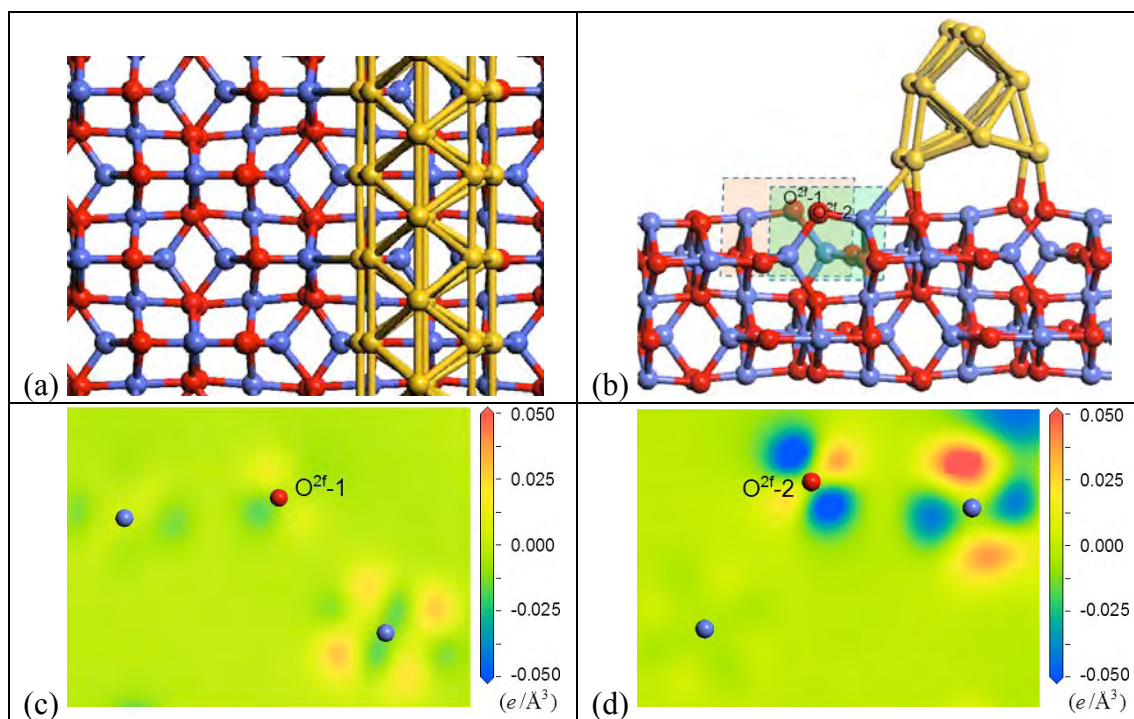


Figure 6.3. (a) Top view of the Au/ Co_3O_4 (110) model, (b) side view of the Au/ Co_3O_4 (110) model, and local charge density difference map of the Co_3O_4 support before and after Au deposition. The charge density difference maps for the (c) the red slice in (b), and (d) the green slice in (b). Blue region denotes accumulation of negative charge (electron) densities.

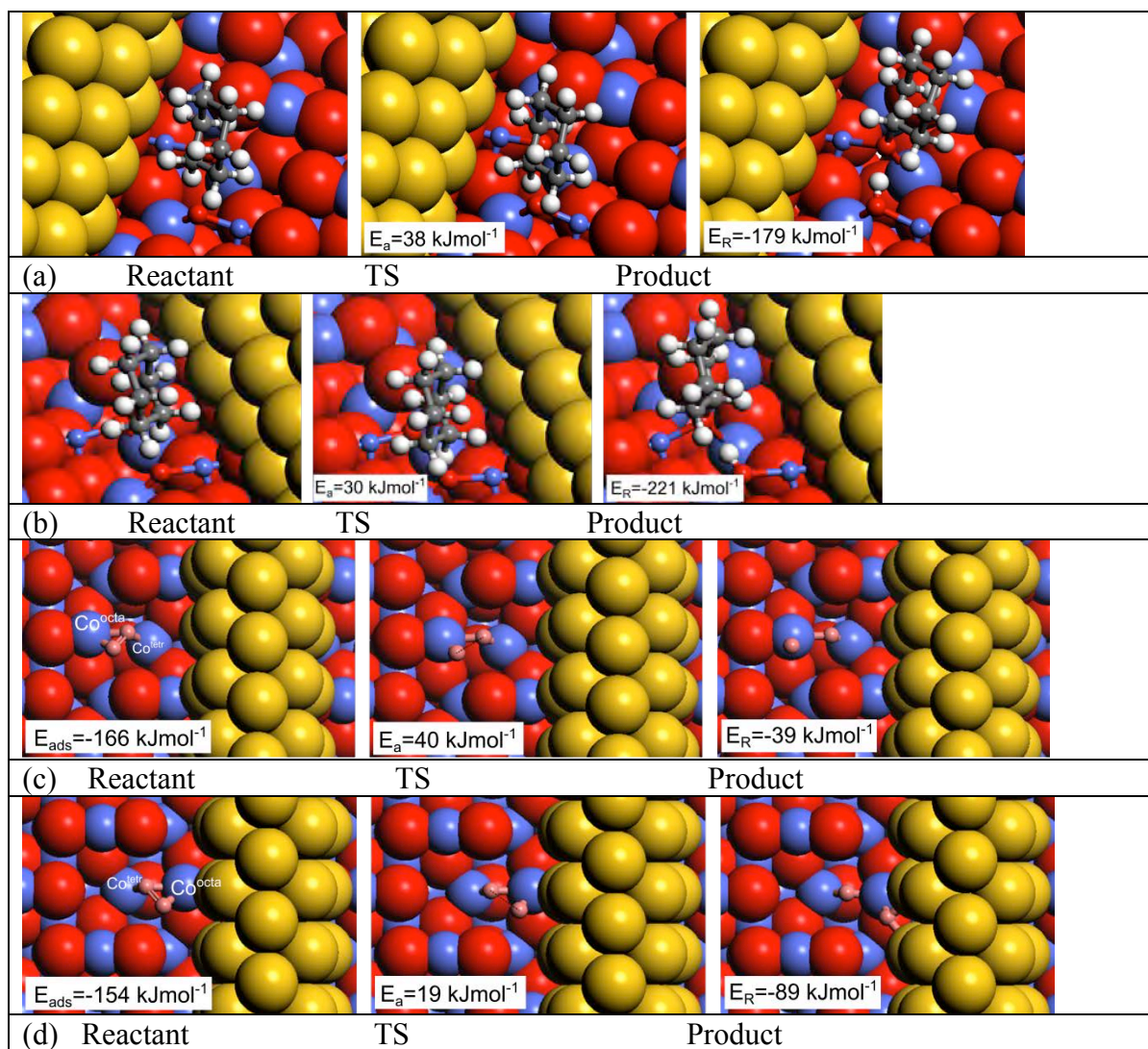


Figure 6.4. Initial C-H activation of cyclohexane at (a) non-interfacial O_{2f} site on the Au/ Co_3O_4 surface, and (b) O_{2f} site near the Au/ Co_3O_4 interface; O_2 dissociation at (c) non-interfacial O_{2f} vacancy, and (d) interfacial O_{2f} vacancy

C. Catalytic cracking over Solid Acid Catalysts

Catalytic cracking is an alternative endothermic reaction (vs. dehydrogenation) that can be used to increase the chemical heat sink of jet fuels. In this past year, we examined in some detail the mechanism associated with C-C bond activation that occurs over acid catalysts. One of the most widely accepted mechanisms involves the insertion of the proton from a Brønsted acid site of solid acid catalyst into the C-C bond to form a carbenium ion intermediate. Density functional theory calculations were performed to study the cracking of butane over tungstated zirconia (WO_x - ZrO_2) and Keggin-type tungsten heteropoly acid (W-HPA). Tungstate zirconia models include a series of small tungsten oxide clusters (W_nO_x , $n=1,2,3,5$) deposited on oxygen terminated (101) surfaces of tetragonal zirconia in order to examine the role of structure, composition and acidity on reactivity. W-HPA models have tungsten atoms that form the metal-oxide shell but have contain different central heteroatoms (Al, Zr, Si, P). Several reaction pathways were investigated to understand

where on the butane the proton attacks, including the proton attacking at the primary carbon, the secondary carbon, and the C-C bond to form carbonium ions. The activation barrier of this initiation step was correlated to the proton affinity (deprotonation energy, DPE) of the active surface site for the WO_x/ZrO_2 (Fig. 6.5) and HPA structures (Fig. 6.6). Our analyses show stronger Brønsted acidity (weaker proton affinity) results in lower activation energy barrier for catalytic cracking of butane. The catalytic cracking occurs easier at the secondary carbon and the primary carbon. Branching at the carbon can also lower the activation barrier, which can be understood as the delocalization of the positive charge stabilizes the carbenium ion.

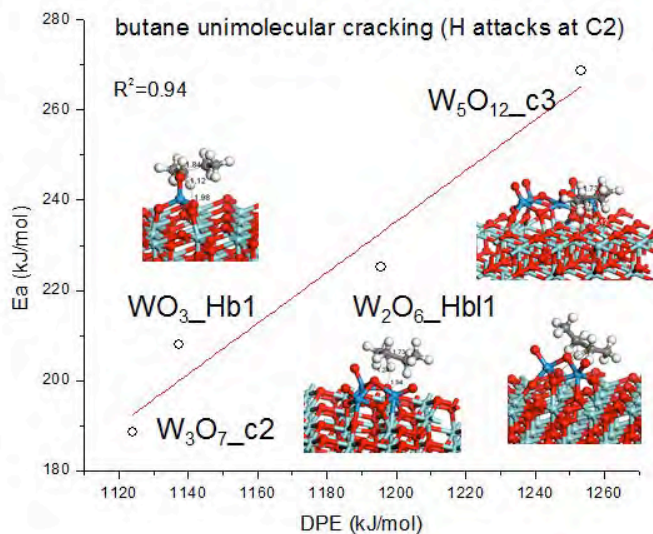


Figure 6.5. DFT-calculated activation energies for the catalytic cracking of butane over monomer, dimer and trimer WO_x clusters on ZrO_2 surfaces.

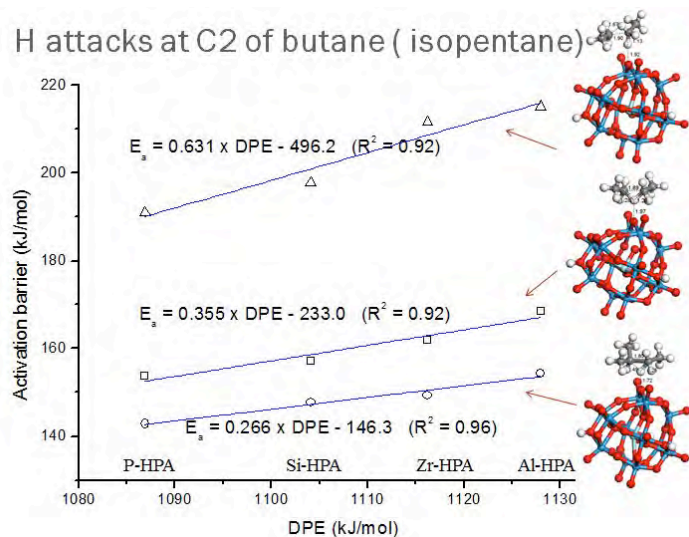


Figure 6.6. DFT-calculated activation energies for the catalytic cracking of butane over different heteropolyacids. Correlation between their reactivity as measured by their activation energy and their acid site strength which is measured by the deprotonation energy of the MO-H site.

We extended these mechanistic studies to include a wide range of different solid acid materials including the heteropolyacids, the supported WO_x supported on ZrO_2 , zeolites, and sulfated zirconia. The activation barriers for the unimolecular cracking of butane were found to be linearly correlated with the solid acidity as measured by ammonia adsorption strength (see figure 6.7) over a range of different Brønsted acids. The results show that the activity increases in moving from the 2D domains of WO_x -supported on ZrO_2 , to the zeolites, sulfated zirconia and HPAs. While these other structures are intrinsically more active, they tend to be less stable and may not be able to survive the harsh operating conditions.

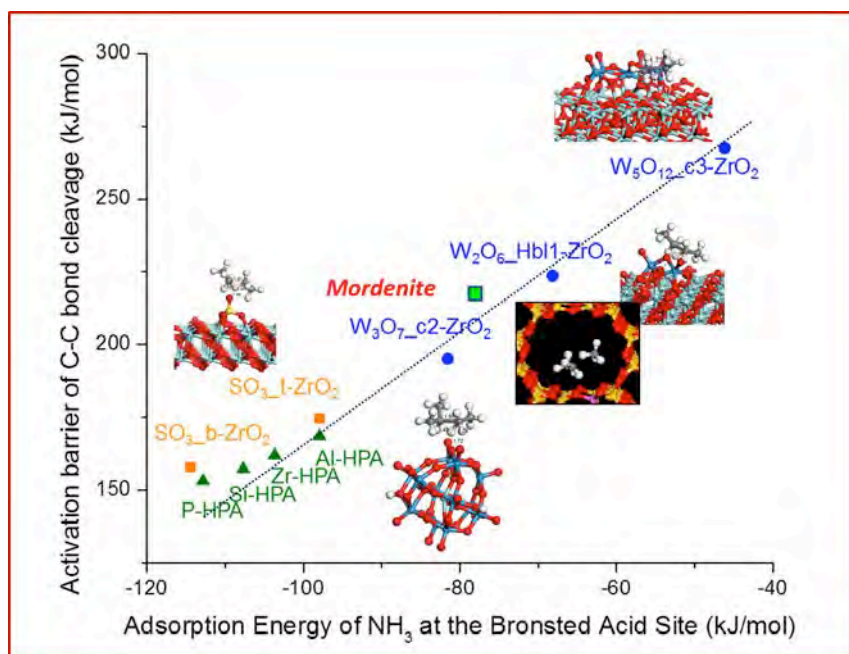
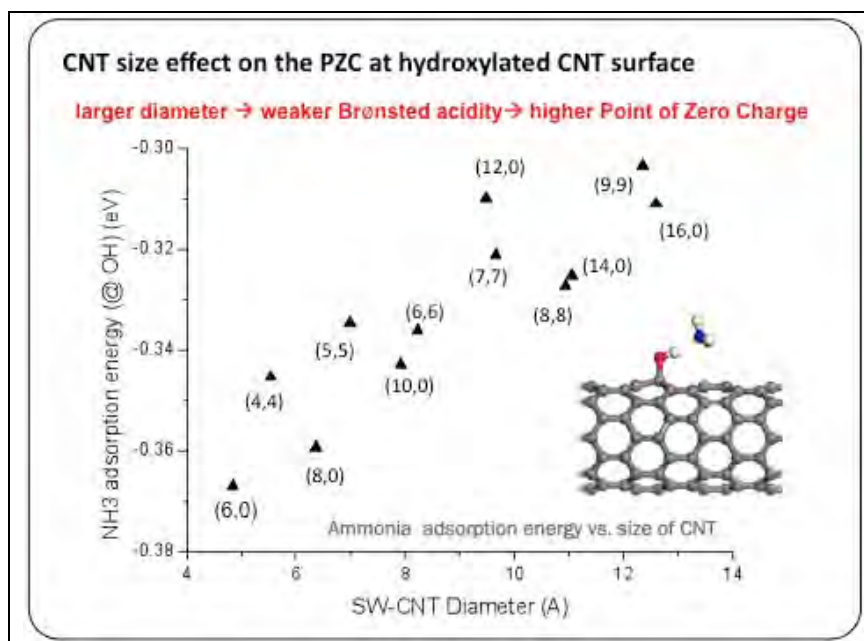


Figure 6.7. Correlations of the C-C bond activation barrier of n-butane with the acidity effect represented by ammonia adsorption energy over different solid acid model systems, including ■ sulfated zirconia; ● tungstated zirconia ; ▲ HPAs. (proton attacks C2-C3 bond) and ■ mordenite.

7. New Insights on SWNT Separation gained from this Project (Pfefferle and Neurock)

In order to carry out ion-exchange processes to decorate SWNT and MWNT Haller and Pfefferle carried out point of zero charge measurements of the nanotubes after a range of post-synthesis treatments. Then Pfefferle synthesized different size classes of SWNT and found that as the diameter increased the tubes became more basic. To follow this up Neurock calculated the ammonia adsorption energy as a function of nanotube identity. Interestingly this was consistent with the PZC data of Pfefferle. This data was used as the basis for an NSF proposal on a new technique for bulk separation of carbon nanotubes by their chiral identity.



An important question we addressed was the character of the SWNT support surface as a function of CNT diameter and chiral angle. The figure to the left shows the ammonia adsorption energy as a function of CNT diameter. The larger the diameter the weaker the Bronsted acid acidity and the higher the point of zero charge.

8. Overall Project Summary

In this project significant work on fundamental aspects of the operation of fuel soluble nano catalysts has been carried out and fundamental links between model and practical catalysts illuminated. Our approach was highly integrative between team members with catalyst fabrication and testing between labs.

We have developed alkane/cycloalkane-soluble Pd, Pt, Ni, Co, Fe, Co-Fe and Co-Pt nanoparticles, ranging from 1-10 nm in diameter, with a variety of different ligands. Pd, Pt, Pt-Co, Co, Ni supported on MWNT, activated carbon and SWNT supports have been developed. Practical catalyst formats were compared with model catalyst prepared using controlled cluster sizes. Size-selected sub-nanometer clusters were deposited on oxide and nanostructured carbon (nanocrystalline diamond) supports to compare with practical nanocatalyst systems and obtain size/mechanism information. We developed acid functionality catalysts based on MWNT- nano-sulfided zirconia and showed that these can be used for low temperature cracking and as an inexpensive nonprecious metal catalyst. For the new acid catalysts grafting allows almost atomic level dispersion and synthesizing the materials with different contact geometries.

We have demonstrated how the endothermic cracking and dehydrogenation reactions that provide the cooling also change the chemical composition of the fuel and that this can either enhance or inhibit ignition of the fuel in the engine.

Our practical work on catalyst synthesis and fuel chemistry was complemented by detailed theoretical and experimental studies on the reactivity of size-selected clusters including studies of support interactions. The links between theory, model catalyst and real catalyst tests were designed to elucidate the behavior of the nanoparticles, establish the study of support-catalyst interactions on a fundamental level to aid in the design of active and stable catalysts. This is clearly shown in our publications and the work described in Appendix I of this report.

References

1. L. Hu, Q. Peng and Y. Li, Selective synthesis of Co_3O_4 nanocrystal with different shape and crystal plane effect on catalytic property for methane combustion, *J. Am. Chem. Soc.*, 130 (2008) 16136-16137.
2. Y. Dong, K. He, L. Yin and A. Zhang, A facile route to controlled synthesis of Co_3O_4 nanoparticles and their environmental catalytic properties, *Nanotech.* 18 (2007) 435602.
3. Z. Chen, A. Xu, Y. Zhang, N. Gu, Preparation of NiO and CoO nanoparticles using M^{2+} -oleate ($\text{M} = \text{Ni}, \text{Co}$) as precursor, *Curr. Appl. Phys.* 10 (2010) 967-970.
4. A. Shavel, B. Rodriguez-Gonzales, J. Pacifico, M. Spasova, M. Farle and L.M. Liz-Marzan, Shape Control in Iron Oxide Nanocrystal Synthesis, Induced by Triocylammonium Ions, *Chem. Mater.* 21 (2009) 1326.
5. M.V. Kovalenko, M.I. Bodnarchuk, R.T. Lechner, G. Hesser, F. Schäffler and W. Heiss, Fatty Acid Salts as Stabilizers in Size- and Shape-Controlled Nanocrystal Synthesis: The Case of Inverse Spinel Iron Oxide, *J. Am. Chem. Soc.* 129 (2007) 6352.
- (6) M. Boucher, S. Goergen, N. Yi and M. Flytzani-Stephanopoulos, "Shape effects" in metal oxide supported nanoscale gold catalysts, *Phys. Chem. Chem. Phys.* 13 (2011) 2517- 2527.
- (7) S. Goergen, C. Yin, B. Lee, S. Lee, C. Wang, M. B. Boucher, G. Kwon, S. Seifert, P. Wu, R. E. Winans, S. Vajda and M. Flytzani-Stephanopoulos, Structure Sensitivity of Oxidative Dehydrogenation of Cyclohexane over FeO_x and Au-FeO_x Nanocrystals, *J. Catal.*, submitted.
- (8) Bolin, T. B. Direct determination of pyrite content in Argonne premium coals by the use of sulfur X-ray near edge absorption spectroscopy (S-XANES). *Energy Fuels*, **2010**, 24, 5479–5482.
- (9) Marcel Di Vece, Qiang Qian, Sungsik Lee, Chunrong Yin, Xiaoming Wang, Byeongdu Lee, Sönke Seifert, Randall E. Winans, Gary L. Haller, Lisa D. Pfefferle, Matthew Neurock, and Stefan Vajda, "Highly Stable Multiwall Nanotube Supported Pt Nanocatalysts for the Dehydrogenation of Cyclohexane: The Effect of Pretreatment of the Support on Catalyst Size and its Performance" *Ang. Chem.* (to be submitted, attached as Appendix I.)

(10) Trevor, D.J., D.M. Cox, and A. Kaldor, *Methane activation on unsupported platinum clusters*. Journal of the American Chemical Society, 1990. **112**(10): p. 3742-3749.

(11) Morse, M.D., M.E. Geusic, J.R. Heath, and R.E. Smalley, *Surface reactions of metal clusters. II. Reactivity surveys with D₂, N₂, and CO*. The Journal of Chemical Physics, 1985. **83**(5): p. 2293-2304.

(12) Tyo, E.C., C. Yin, M. Di Vece, Q. Qian, S. Lee, B. Lee, S. Seifert, R. E. Winans, R. Si, B. Ricks, S. Goergen, M. Flytzani-Stephanopoulos, Z. Wang, R. E. Palmer, M. Neurock, and S. Vajda, "Oxidative Dehydrogenation of Cyclohexane on Cobalt Oxide (Co₃O₄) Nanoparticles: The Effect of Particle Size on Activity and Selectivity", ACS Catal., 2. 11, 2409-2423, 2012.

Personnel - MURI project (all or partially spent time on this project)

Raymond J. Gorte, Partial support of the following: Noah Weider, Biquan Su, Chen Chen (Weider graduated this year with his PhD) (University of Pennsylvania)

Lisa Pfefferle, Gary Haller, Sungchul Lee, Charles McEnally, Xioaming Wang, Magdalena Majewska, Nan Li, Gayatri Keskar, Nan Yi, Chang Chang Liu (Yale University)
Stefan Vajda (Argonne/Yale)

Matt Neurock, Qiang Qian and Corneliu (University of Virginia)

Maria Stephanopoulos, B. Ricks, partial Simone Goergen, Matthew Boucher, Chonyang Wang (Tufts University)

List of publications citing this grant

“Control of Metal Nanocrystal Size Reveals Metal-Support Interface Role for Ceria Catalysts”, M. Cargnello, V. Doan-Nguyen, T. R. Gordon, T. Paik, R. E. Diaz, E. A. Stach, R. J. Gorte, P. Fornasiero, and C. B. Murray, *Science*, 341 (2013) 771-3.

“High pressure cracking of n-hexane over H-ZSM-5”, Jing Luo and R. J. Gorte, *Catalysis Letters*, 143 (2013) 313-316.

"Structure Sensitivity of Oxidative Dehydrogenation of Cyclohexane over FeO_x and $\text{Au/Fe}_3\text{O}_4$ Nanocrystals", S. Goergen, C. Yin, M. Yang, B. Lee, Sungsik Lee, C. Wang, P. Wu, M. Boucher, G. Kwon, S. Seifert, R. Winans, S. Vajda, and M. Flytzani-Stephanopoulos, *ACS Catal.*, 3 (2013) 529–539.

"Atomically Dispersed $\text{Au}-(\text{OH})_x$ Species Bound on Titania Catalyze the Low-temperature Water-Gas Shift Reaction", M. Yang, L. F. Allard, and M. Flytzani-Stephanopoulos, *J. Am. Chem. Soc.*, 135 (2013) 3768–3771.

"Silica-encapsulated platinum catalysts for the low-temperature water-gas shift reaction", Y. Wang, Y. Zhai, D. Pierre, and M. Flytzani-Stephanopoulos *Appl. Cat. B*, 127 (2012) 342-350.

"Core-Shell-Type Materials Based on Ceria", M. Cargnello, R. J. Gorte, and P. Fornasiero, to be published in revised edition of "Catalysis by Ceria and Related Materials", A. Trovarelli, editor, Imperial College Press, 2013.

Metal nanoparticles inside multi-walled carbon nanotubes: A simple method of preparation and of microscopic image analysis X. Wang, N. Li, L. Pfefferle, G. L. Haller, *Microporous and Mesoporous Materials*, vol.176 pg:139 -144, (2013).

“Gold Doped Cobalt Oxide Nanocatalysts: An in-situ Investigation Using Synchrotron Radiation” E. C. Tyo, C. Yin, M. Di Vece, Q. Qian, R. Si, M. Flytzani-Stephanopoulos, S. Lee, B. Lee, S. Seifert, R. E. Winans, Z. Wei Wang, R. E. Palmer, M. Neurock, and S. Vajda, Preprints, Energy and Fuels Division, American Chemical Society, 245, 2013.

“Subnanometer to Nanometer Size Catalysts for C-H Bond Activation from Precious Metals to Alternatives” S. Vajda, S. Lee, M. Di Vece, B. Lee, S. Seifert, R. Winans, L. Pfefferle, G. Haller, G. Ferguson, J. Greeley, L. Curtiss, Q. Qian, M. Neurock, Preprints, Energy and Fuels Division, American Chemical Society, 245, 2013.

“Dispersible core-shell $\text{Pd}@$ ceria structures as supramolecular building blocks for high performance methane combustion catalysts”, M. Cargnello, J. J. Delgado Jaén, J. C. Hernández Garrido, K. Bakhmutsky, T. Montini, J. J. Calvino Gamez, R. J. Gorte and P. Fornasiero, *Science*, 337 (2012) 713-717.

“Controlling the Particle Size of ZrO_2 Nanoparticles in Hydrothermally Stable $\text{ZrO}_2/\text{MWCNT}$ Composites”, Liu, Changchang; Lee, Sungchul; Su, Dong; B. Lee, S. Lee. R. Winans, C. Yin, S. Vajda, Pfefferle, Lisa; G.L. Haller, *Langmuir*, vol. 28(49), pp. 17159-17167, (2012a).

"One-step synthesis of a Pt–Co–SWCNT hybrid material from a Pt–Co–MCM-41 catalyst X. Wang, N. Li, X. Zhang, C. Liu L. Pfefferle, G.L. Haller, *Journal of materials chemistry*, vol. 22(48), pp 25083-25092, (2012).

"Multi-Walled Carbon Nanotubes drive the activity of metal@oxide core-shell catalysts in modular nanocomposites", M. Cargnello, M. Grzelczak, J.B. Rodríguez-González, Z. Syrgiannis, K. Bakhmutsky, V. La Parola, L. Liz-Marzán, R.J. Gorte, M. Prato, and P. Fornasiero, *Journal of the American Chemical Society*, 134 (2012) 11760-66.

Synthesis and Characterization of Nano-composites with Strong Interfacial Interaction: Sulfated ZrO₂ Nanoparticles Supported on Multi-walled Carbon Nanotubes, C. Liu, S. Lee, D. Su, Dong; L. Pfefferle, GL Haller, *J. Phys. Chem. C*, vol. 116(41), pp 21742-21752, (2012).

"A Versatile Route to Core-Shell Catalysts: Synthesis of Dispersible M@Oxide (M = Pd, Pt; Oxide = TiO₂, ZrO₂) Nanostructures by Self-Assembly", Kevin Bakhmutsky, Noah L. Wieder, Matteo Cargnello, Benjamin Galloway, Paolo Fornasiero, and Raymond J. Gorte, *ChemSusChem*, 5 (2012) 140-8.

High yield hydrogen production from aqueous phase reforming over single-walled carbon nanotube supported catalysts, X. Wang, N. Li, X. Zhang, C. Wang, L. Pfefferle, G.L. Haller, *ACS Catal.*, (2012) 2, 1480-1486.

"Oxidative Dehydrogenation of Cyclohexane on Cobalt Oxide (Co₃O₄) Nanoparticles: The Effect of Particle Size on Activity and Selectivity", E. C. Tyo, C. Yin, M. Di Vece, Q. Qian, S. Lee, B. Lee, S. Seifert, R. E. Winans, R. Si, B. Ricks, S. Goergen, B. Zugic, M. Rutter, M. Flytzani-Stephanopoulos, Z. Wang, R. E. Palmer, M. Neurock, and S. Vajda, *ACS Catal.* 2 (2012), 2409–2423, *invited paper*.

"Size-and composition optimized sub-nanometer and nm size catalysts for low-temperature jet-fuel activation", S. Vajda, S. Lee, M. Di Vece, B. Lee, S. Seifert, R. E. Winans, G. A. Ferguson, L. A. Curtiss, J. P. Greeley, Q. Qian, M. Neurock, S. Goergen, R. Si, M. Flytzani-Stephanopoulos, X. Wang, G. L. Haller and L. A. Pfefferle, *Prepr. Am. Chem. Soc., Div. Pet. Chem.*, 2011, 56 (1), 384-385, CODEN: PSADFZ, ISSN: 1521-4648, , Accession Number 2011:317971, CAN 155:332336, CAPLUS

Simultaneous Measurement of X-ray Small Angle Scattering, Absorption, and Reactivity: A Continuous Flow Catalysis Reactor", S. Lee, B. Lee, S. Seifert, S. Vajda and R. E. Winans *Nucl. Instr. and Meth. A*, **649**. 200-203 (2011).

"Expeditious synthesis of thiol-protected COOH functionalized Pd nanoparticles and their activity and recyclability for Suzuki coupling reactions", M. Cargnello, N. L. Wieder, P. Canton, T. Montini, A. Benedetti, R. J. Gorte, and P. Fornasiero, *Chemistry of Materials*, 23 (2011) 3961–3969.

"Highly Active and Thermally Stable Core-Shell Catalysts for Solid Oxide Fuel Cells", J.-S. Kim, N. L. Wieder, A. J. Abraham, M. Cargnello, P. Fornasiero, R. J. Gorte, and J. M. Vohs, *Journal of the Electrochemical Society*, 158 (2011) B596-600.

“A Study of the Water-Gas-Shift Reaction on Pd@CeO₂/Al₂O₃ Core-Shell Catalysts”, N. L. Wieder, M. Cargnello, T. Montini, P. Fornasiero, and R. J. Gorte, *Journal of Physical Chemistry C*, 115 (2011) 915-19.

In-situ Real Time GIXAS/GISAXS Study of Oxidative Dehydrogenation of Cyclohexene on Size Selected Sub-nanometer Cobalt Cluster Catalysts", S. Lee, B. Lee, S. Seifert, R. E. Winans, M. Di Vece and S. Vajda, *Prepr. Am. Chem. Soc., Div. Pet. Chem.*, 2011, **56** (1), 408-409, CODEN: PSADFZ, ISSN: 1521-4648, Accession Number 2011:318074, CAN 155:332336, CAPLUS.

“Shape Effects' in Metal Oxide Supported Nanoscale Gold Catalysts”, M. B. Boucher, S. Goergen, N. Yi, and M. Flytzani-Stephanopoulos, *Phys. Chem. Chem Phys.*, 13 (2011) 2517-2527.

“Hydrogen Production from Methanol over Gold Supported on ZnO and CeO₂ Nanoshapes”, M. B. Boucher, N. Yi, F. Gittleson, B. Zugic, H. Saltsburg, and M. Flytzani-Stephanopoulos, *J. Phys. Chem. C*, 115 (2011) 1261-1268.

Characterization of multi-walled carbon nanotubes catalyst supports by point of zero charge Catalysis today [0920-5861] S. Lee, Z. Zhang, X. Wang L. D. Pfefferle and G. L. Haller (2011) vol:164 iss:1 pg:68 -73

Effect of surface oxygen containing groups on the catalytic activity of multi-walled carbon nanotube supported Pt catalyst Xiaoming Wang, Nan Li, Jeffrey A. Webb, Lisa D. Pfefferle and Gary L. Haller, *Applied Catalysis, B, Env.*, vol., 101(1-2), 2010, 21-30.

Pt-Co bimetallic catalyst supported on single-walled carbon nanotubes: Effect of alloy formation, Wang XM, Li N, Pfefferle LD and Haller G.L., *J. Phys. Chem. C*, Vol. 114 (40), 2010, 16996-17002.

“Synthesis of dispersible Pd@CeO₂ nanostructures by self-assembly”, M. Cargnello, N. Wieder, T. Montini, R. J. Gorte, and P. Fornasiero, *Journal of the American Chemical Society*, 132 (2010) 1402-9.

“Novel Embedded Pd@CeO₂ Catalysts: A Way to Active and Stable Catalysts”, M. Cargnello, T. Montini, S. Polizzi, N. Wieder, R. J. Gorte, M. Graziani, and P. Fornasiero, *Dalton Transactions*, 39 (2010) 2122.

"Active gold species on cerium oxide nanoshapes for methanol steam reforming and the water gas shift reactions," N. Yi, R. Si, H. Saltsburg and M. Flytzani-Stephanopoulos, *Energy Environ. Sci.*, 3 (2010) 831 - 837.

"Steam reforming of methanol over ceria and gold-ceria nanoshapes", N. Yi, R. Si, H. Saltsburg, and M. Flytzani-Stephanopoulos. *Appl. Catal. B*, 95 (2010) 87-92.

Papers Submitted for Publication

“Oxidative Dehydrogenation of Cyclohexene on Size Selected Subnanometer Cobalt Clusters: Improved Catalytic Performance via Structural Fluxionality of Cluster-Assembled Nanostructures: An *in Situ* GISAXS/GIXAS/TPRx Study”, S. Lee, M. Di Vece, B. Lee, S. Seifert, R. E. Winans and S. Vajda, *Submitted Phys. Chem. Chem. Phys.*

“Size and Support-Dependent Reactivity of Subnanometer Cobalt Catalysts with CO and H₂: A combined GIXAS, GISAXS and TPRx Study” S. Lee, B. Lee, S. Seifert, R. E. Winans, and S. Vajda *submitted to Phys. Chem. Chem. Phys.*

Papers is Draft Available from * author

“Oxidative Dehydrogenation of Cyclohexane on CoOx and Au/CoOx Nanocrystals”, E.C. Tyo, M. Di Vece, S. Goergen, R. Si, Z. Wang, R. E. Palmer, R.E. Winans, M. Neurock, M. Flytzani-Stephanopoulos, and S. Vajda*, *to be submitted*.

“Increased Activity of Co₃O₄ Nanocubes by Sub-nm Au Clusters in the Oxidative and Non-Oxidative Dehydrogenation of Cyclohexane: A joint Experimental and Theoretical Study” Marcel Di Vece, Qiang Qian, Z. Wang, Sungsik Lee, Byeongdu Lee, Soenke Seifert, Rui Si, Brian Ricks, Maria Flytzani-Stephanopoulos, Randall Winans, Richard Palmer, Mathew Neurock*, Stefan Vajda*

“Highly Stable Multiwall Nanotube Supported Pt Nanocatalysts for the Dehydrogenation of Cyclohexane: The Effect of Pretreatment of the Support on Catalyst Size and its Performance” Marcel Di Vece, Qiang Qian, Sungsik Lee, Chunrong Yin, Xiaoming Wang, Byeongdu Lee, Sönke Seifert, Randall E. Winans, Gary L. Haller, Lisa D. Pfefferle, Matthew Neurock*, and Stefan Vajda* (*included here as appendix I*)

“Effects of Acidity on the Catalytic Cracking of Alkanes Fuels”, Qiang Qian and Matthew Neurock*

“The Electronic Structure or Charge Delocalization on of Sulfated Zirconia (Supported on Multi-Walled Carbon Nanotubes): Acid Sites Probed by X-Ray Absorption Spectroscopy.” C. Liu, L. D. Pfefferle and G. L. Haller*, *Topics in Catalysis*, to be submitted.

“Novel Combined Zr and S XANES Analysis on S-ZrO₂/MWCNT Solid Acid Catalyst,” C. Liu, T. Bolin, P. Northrup, S. Lee, C. McEnally, P. Kelleher, L. D. Pfefferle and G. L. Haller, *Appl. Catal.*, to be submitted.

New discoveries, inventions, or patent disclosures. (If none, report None.)

A patent is being filed on the new acid functionalized MWNT catalysts. Two versions have been fabricated and tested. Tungstated zirconia catalysts have slightly lower activity than the sulfated produced last project year but are very high temperature stable.

Appendix #1 is given below. It is a draft of our paper on experiment and modeling of the size effect of Pt on SWNT on cyclohexane dehydrogenation selectivity.

Particle Size Dependent Control of Catalytic Selectivity in the Dehydrogenation of Cyclohexane over Stable Multiwall Nanotube Supported Pt Particles.

Marcel Di Vece^{1,ε,@}, Qiang Qian^{2,ε}, Sungsik Lee^{3,ε}, Chunrong Yin^{4,ε,#}, Xiaoming Wang^{1,ε,&},
Byeongdu Lee³, Sönke Seifert³, Randall E. Winans³, Gary L. Haller¹, Lisa D. Pfefferle¹, Matthew
Neurock^{3§}, and Stefan Vajda^{1,4,5*}

¹*Department of Chemical Engineering, School of Engineering & Applied Science,
Yale University, Hillhouse Avenue, New Haven, CT 06520, USA*

²*Department of Chemical Engineering, University of Virginia,
102 Engineers' Way,
Charlottesville, VA 22904, USA*

³*X-Ray Sciences Division, Argonne National Laboratory,
9700 South Cass Avenue,
Argonne, IL 60439, USA*

⁴*Materials Science Division, Argonne National Laboratory,
9700 South Cass Avenue,
Argonne, IL 60439, USA*

⁵*Nanoscience and Technology Division, Argonne National Laboratory,
9700 South Cass Avenue, Argonne, IL 60439, USA*

^ε Equally contributing (first) authors

[@] Present address: Faculty of Science, Debye Institute for Nanomaterials Science Utrecht University,
P.O. Box 80.000, NL-3508 TA Utrecht, The Netherlands

[&] Present address (XW): BASF Corporation, 25 Middlesex/Essex Turnpike, Iselin, NJ 08830, USA

[#] Present address: Department of Chemical Engineering, Carnegie Mellon University, 5000 Forbes
Avenue Pittsburgh, PA 15213, USA

[§] Corresponding author: mn4n@virginia.edu (MN)

^{*} Also corresponding author: vajda@anl.gov (SV)

One-sentence summary: In-situ characterization, kinetic analyses and first-principle theoretical simulations are used to demonstrate the changes in the kinetics and selectivity for the conversion of cyclohexane to cyclohexene and benzene over highly stable well-controlled nm-sized Pt particles synthesized on multi-wall carbon nanotubes.

Abstract:

Carbon nanotubes are very attractive catalyst supports as they have high surface areas and can be readily functionalized in order to anchor metal nanoparticles and fine-tune their catalytic properties. More specifically we examine the kinetics and selectivity of platinum nanoparticle-decorated multi-walled carbon nanotubes for the gas-phase. The results reveal that Pt particles which are ≤ 1 nm contain $> 85\%$ coordinatively unsaturated edge and corner sites which preferentially activate C-H bonds and convert cyclohexane to benzene as the barriers for the subsequent C-H bond activation steps are much less than the barriers for cyclohexene and cyclohexadiene intermediates to desorb. Pt clusters that are > 2 nm, on the other hand, have $> 50\%$ coordinatively-saturated 111 terrace sites which result in higher barriers for C-H activation and lower barriers for desorption. Larger particles thus lead to increased rates of cyclohexene desorption over the formation of benzene. There appears to be a distinct cross-over in product selectivities where particles that were less than 2 nm result in higher selectivities to benzene whereas particles greater than 2 nm yield in cyclohexene and cyclohexadiene. The results suggest that by proper functionalization and creation of defects on the surface of the carbon nanotubes, the catalytic performance of very small nanocatalysts can be effectively controlled.

Introduction

The addition of soluble or dispersible catalysts into jet fuels (1) can significantly accelerate combustion and increase the heat sink capacity of the fuel. The design of catalysts for such systems presents considerable challenges as the materials must be highly active, selective, fuel-soluble, and resistant to sintering and coking at high temperatures and harsh oxidizing conditions. Some of these requirements can be met by anchoring catalytic nanoparticles onto inert, fuel-soluble or dispersible high surface area supports. Carbon nanotubes (CNT) may be excellent candidates for such applications. A second major advantage of using carbon nanotubes as supports is that they can be readily disintegrated during the combustion process; this must, however, preclude the formation of large metal and metal oxide aggregates which could cause damage to the engine. In addition to the changes in metal and potential promoters, the modification of the surface of the CNT provides an important lever to optimize the properties of the anchored nanoparticles (2). Catalytically reactive small metal nanoparticles (with diameter from less than 1 nm to few nm) provide not only a high surface-area-to-volume ratio; but also a high fraction of coordinatively unsaturated sites. The size and shape of catalytic metal nanoparticles control the distribution of different surface sites and their corresponding coordination numbers which ultimately dictates the surface reaction rate (3) and the mobility of surface species (4), influencing in turn the overall activity and selectivity for a particular catalytic reaction.

Cycloalkanes form a considerable portion of most fuels (5) and their catalytic dehydrogenation pathways offers insights into improved catalytic dehydrogenation of actual fuels toward the lower temperature activation and improved heat sink capacity. It was reported that the dehydrogenation of cyclohexane to benzene on Pt(111) occurs already at low temperatures with a maximum turnover rate at about 100° C (6). Dehydrogenation of cyclohexane is a structure sensitive reaction, Pt steps and small Pt particles were found to enhance the catalytic activity (7) (8). A recent study (9) on silica-supported monodisperse platinum nano-particles (1.7 – 7.1 nm) showed small particles had lower activation barriers for cyclohexene dehydrogenation than large particles.

In this work, cyclohexane was used as surrogate for jet fuel, and its dehydrogenation over Pt nanoparticles formed on pretreated and untreated multi walled carbon nanotubes (MWNT) studied experimentally as well as theoretically. The size and density of the particles and their interaction with the support are important parameters in controlling the properties of the catalyst (10). As received MWNT, as well as differently pretreated MWNTs were used in an effort to examine the effect of pretreatment of the support on the properties and performance of the supported Pt nanoparticles. During pretreatment of the MWNTs,

the MWNT surface was functionalized with oxygen containing groups by refluxing in nitric acid for 4 hr. A fraction of the functionalized MWNT's was subsequently annealed at 1273K. As the last synthesis step, the MWNTs were decorated by Pt nanoparticles. The catalysts obtained on untreated MWNTs, nitric acid-treated and annealed MWNTs are labeled herein as Pt-MWNT, Pt-MWNT-HNO and Pt-MWNT-HNO-hT, respectively. In all these catalysts, the Pt loading was 8 wt%. The particle sizes determined from extended X-ray absorption fine structure (EXAFS) for Pt-MWNT, Pt-MWNT-HNO and Pt-MWNT-HNO-hT were calculated to be 2.2 +/-1.2 nm, 1.1 nm +/-0.3 nm and 1.3 nm +/-0.4 nm respectively, in good accord with the mean particle size determined by transmission electron microscopy (TEM), 2.3 +/- 1.4 nm, 1.1 +/- 0.6 nm and 1.2 +/- 0.7 nm. (11) The difference in Pt-particle size between the samples is likely the result of the introduction of functional groups (such as -COOH, C=O) during pretreatment with nitric acid and the removal of these groups after annealing. No Pt-O bonding was detected in the Pt nanoparticles by EXAFS analysis. TEM showed that the untreated MWNT have closed ends while the treated ones have open ends. (12) In contrast to the closed end MWNT, the open ends allow for the deposition of some Pt particles inside the MWNT as well. (12) The Pt particles formed inside the nanotubes are likely smaller than those on the surface of the MWNT. The fraction of these Pt particles (and atoms) residing inside the MWNT may additionally affect the average particle size determined from EXAFS, while at the same time their participation in the reaction will be very limited due hindered access to the reactants.

Decorating such functionalized CNTs has been demonstrated for various catalytic reactions (13) (14) (15). Since the dehydrogenation reaction is performed at elevated temperatures, the stability of the Pt catalyst and its MWNT support are prerequisites for sustained catalytic reaction over the expected lifetime of the catalyst. Sintering of nano-sized Pt particles at elevated temperatures is a well-known phenomenon (16) which can alter or hinder catalytic activity(17) and affect selectivity.

In order to investigate the stability of the small MWNT-supported Pt particles morphological and compositional properties of the system were analyzed *in situ* during the course of reaction. Temperature controlled reaction (TPRx) combined with *in situ* grazing incidence small angle scattering (GISAXS) and X-ray absorption (GIXAS) (18) (19) (20). GISAXS was used to investigate size and shape changes, while GIXAS, and more specifically grazing incidence X-ray absorption near edge spectroscopy (GIXANES) was used to elucidate the electronic properties, i.e. the oxidation state of platinum. Additional characterization of the size of the Pt nanoparticles was carried out using transmission small-angle X-rays scattering (SAXS). Mass spectra were recorded to monitor product formation and the reactant depletion.

Based on the analysis of the mass spectra, cyclohexene, cyclohexadiene, benzene and hydrogen were identified as dominant reaction products in the dehydrogenation of cyclohexane. The reference blank MWNT samples which were measured for the determination of the background signals resulted in responses to cyclohexane that were orders of magnitude smaller than those under identical reaction conditions. Thus, the origin of the observed reactivity can be unambiguously attributed to the Pt nanoparticles. During reactions up to 225 °C, no sintering of Pt particles or change of the MWNT size was observed by GISAXS (see Fig. S1), nor by SAXS when heated under helium (see Fig. S2). Analysis of GIXANES spectra during the reactions revealed that there were no changes to the Pt metal during the course of reaction, i.e. oxidation state or carbide formation. In general, the measured product levels remained constant within about 10% over several hours of reaction, suggesting that the catalytic activity does not change. The GISAXS and GIXANES analysis, along with the stable reaction rate over the duration of the experiment points to the high stability and poison-resistance of the carbon nanotube supported platinum nanoparticles.

The evolution of the temperature ramp and the transient ion signals (m/z) of the reactant and products are shown in Figure 1 for all three catalyst samples. In the case of the Pt-MWNT sample (Fig. 1.a), product formation is observed at 200 °C, which increases significantly at 225 °C. The increase in product signals is accompanied by a decrease in the ion signal of the reactant. When the temperature starts to decrease at the end of the reaction, the product signals return to their base values, while the cyclohexane signal recovers to its original level before the reaction. For the Pt-MWNT-HNO sample (Fig. 1.b), the onset of product formation was observed already at 145 °C. The production of cyclohexadiene and benzene is constant with time at 225 °C, while there is a drop in cyclohexene production observed. In the case of the Pt-MWNT-HNO-hT sample (Fig. 1.c), there is an interesting feature observed: the peak in the cyclohexene transient at 185 °C during the temperature ramped up to and down from 225 °C. This feature only occurs with sample Pt-MWNT-HNO-hT. We hypothesize that this propensity is a consequence of the pre-treatment of the MWNT.

The per total Pt atom TOR values for cyclohexane consumption along with the TOR values of the created products over all three catalysts are reported in Figure 2. Taking into consideration the estimated uncertainties in the measurement of the ion signal (better than 10%) and in the determination of the metal loading, the per total Pt atom activity of all three samples is comparable. Cyclohexane TORs per total Pt atom were calculated to be 0.45, 0.50 and 0.40 s⁻¹ per total Pt atom for the untreated Pt-MWNT and for the treated Pt-MWNT-HNO and Pt-MWNT-HNO-HT samples, respectively, thus practically identical

within the estimated uncertainty of 10%. The per surface Pt atom based cyclohexane TORs, however, were calculated to be 1.72, 0.94 and 0.82 s⁻¹ per surface Pt atom for the Pt-MWNT, Pt-MWNT-HNO and Pt-MWNT-HNO-HT samples, respectively. The obtained TOR values are in good overall agreement with literature values which range from 0.1 to 5 molecules Pt atom⁻¹ s⁻¹ (7, 21-24) and in an excellent agreement (within less than a factor two) with TOR values reported on identical samples from Wang *et al.* who used a fix bed reactor. (12)

Although the per total Pt atom reactivity of the three samples is comparable, their selectivity differs considerably as shown in the histograms of Figure 2. The Pt-MWNT sample (Fig. 2a) predominantly produces cyclohexene (~0.3 molecules/total-Pt-atoms/s) and cyclohexadiene (~0.2 molecules/total-Pt-atoms/s), intermediate dehydrogenation products (25) with very little formation of benzene (~0.03 molecules/total-Pt-atoms/s). The Pt-MWNT-HNO sample (Fig. 2b), however, results in significant benzene formation (~0.1 molecules/total-Pt-atoms/s). This is accompanied by a drop in the formation of cyclohexene (~0.075 molecules/total-Pt-atoms/s). The results on the Pt-MWNT-HNO-HT sample (Fig. 2c), show that only extremely small amounts of cyclohexene (< 0.01 molecules/total-Pt-atoms/s) are produced. Interestingly, the formation of cyclohexadiene is comparable on all three catalysts (~0.15-0.2 molecules/total-Pt-atoms/s). This trend confirms that the pretreatment/functionalization of the nanotube support provides a very efficient handle to control catalytic performance of the MWNT-supported Pt nanocatalyst. The role of the annealed support is illustrated by the extremely strong temperature dependence of the selectivity of the Pt-MWNT-HNO-HT sample shown in Figure 2. The selectivities at 185 °C and 225 °C were diametrically different. At 185 °C, cyclohexene (~0.019 molecules/total-Pt-atoms/s) and cyclohexadiene (0.043 molecules/total-Pt-atoms/s) were the predominant products and no benzene was produced; while at 225 °C, the selectivity shifted completely to the unsaturated products, i.e. cyclohexadiene and benzene. (cf peaking of cyclohexene formation shown in Fig. 1c). The summation of the benzene, cyclohexene and cyclohexadiene TOR's does not fully match the cyclohexane consumption for the given samples. This is likely due to the presence of other reaction intermediates and/or products (i.e. cracking) which could not be unambiguously identified due the complex fragmentation pattern of the mass spectra. It is important to note that gas chromatography is much better suited to obtain a full mass balance as well as for the exact quantification of the amount of hydrogen produced. The applied mass spectrometry has its advantage while working with ultra-small amounts of nanocatalysts.

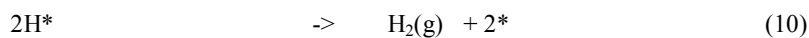
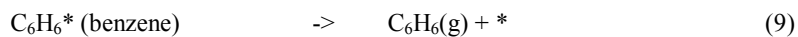
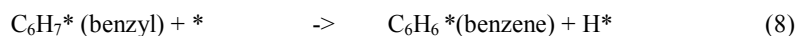
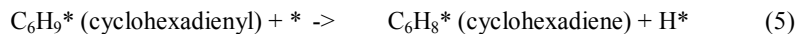
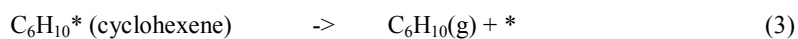
In order to understand the influence of Pt particle size on the reactivity and selectivity, an extensive set of first-principle density functional theory (DFT) calculations were carried out to determine the activation

barriers and overall reaction energies for the elementary steps involved in the dehydrogenation of cyclohexane to cyclohexene, cyclohexadiene and benzene products over CNT supported and unsupported Pt particles. Initial calculations were carried out at low coverages to understand the surface chemistry. In order to appropriately compare with experimental results, the calculations were subsequently performed at high hydrocarbon surface coverages. The (111) and (100) terrace, edge and corner sites that exist on both small 55 atom (Pt_{55}) and large 201 atom (Pt_{201}) cubo-octahedral Pt particles were explicitly examined as representative models of the actual supported Pt particles. All of the calculations reported herein were carried out within the generalized gradient approximation using the Perdew-Burke-Ernzerhof (PBE) (26, 27) form of the exchange correlation functional along with the projector augmented wave method (PAW) (28, 29) as implemented in the Vienna Ab initio Simulation Package (VASP) (30-33). More details on the method and its application are reported in the Supplemental Information.

The initial calculations were carried out on a cubo-octahedral Pt_{55} cluster anchored at a defect site within the outer wall of the (8,8) carbon nanotube as is shown in (Fig. S6a) to provide a representative model of supported Pt clusters. The same calculations were also carried out over the unsupported Pt_{55} cluster in order to establish the effects of the support. The adsorption energies, activation barriers and the reaction energies were calculated for the series of elementary C-H bond activation steps for the model reaction of propane to propylene on the (111) and (100) terrace, edge and corner sites on the supported and unsupported Pt_{55} clusters. The results shown in Fig. S7 indicate that the differences between the supported and unsupported cluster are very small (in general $< 10\%$). The only exceptions are for the Pt sites near the Pt-C interface, where the propane C-H bond activation energy is about 10 kJ/mol (35%) higher. This is likely due to steric hindrance at the Pt center from the CNT support and charge transfer that occurs from the CNT to the Pt. The latter is consistent with the results from a Bader (34) charge analysis which shows 0.14 electrons are transferred from defect CNT support to the Pt_{55} cluster. The changes that occur upon anchoring the Pt_{55} cluster to the inside wall of the defect (14,14) CNT were also analyzed for comparison with those where Pt is anchored outside. Bader charge analysis results shown in Fig. S6b indicate that 0.4 electrons are transferred from the support to the Pt_{55} cluster inside which is slightly higher than 0.14 electrons when Pt_{55} is anchored outside of the CNT. The increase in charge transfer results in a higher barrier to activate the C-H bond. This is consistent with recent experimental and other theoretical results that suggest that the clusters inside of nanotubes are less reactive than those outside (35) (36) (37) and results that show that small negatively charged Pt clusters are less active than neutral clusters in C-H bond activation of methane (38). Since the reactivity of the Pt clusters inside of the CNT is lower than those anchored to the outside and since the difference between the externally supported and

unsupported Pt clusters were very small, we simplified the subsequent calculations and analyzed only the unsupported Pt clusters. We should note that while EXAFS data suggest that ~80% of the Pt particles in the hT sample are inside the CNT, the more active Pt atoms may be the particles that reside outside of the CNT.

The initial model computational studies on the propane activation were extended to examine the activation and selectivity for the dehydrogenation of cyclohexane for different Pt particle sizes in order to compare with the experimental results. DFT calculations were therefore carried out to analyze the reaction pathways of the stepwise dehydrogenation of cyclohexane to cyclohexene, cyclohexadiene and benzene shown in Eqs. (1)-(10):



over both Pt₅₅ (~1.2 nm) and Pt₂₀₁ (~1.8 nm) nanoparticles (shown in [Fig. S4](#)) * refers to a Pt surface site.

The lowest energy paths on both Pt₅₅ and Pt₂₀₁ particles are summarized and compared together in [Figure 3](#). The elementary steps outlined in Eqs. 1-10 which comprise the mechanism are assumed to be the same on both Pt₅₅ and Pt₂₀₁ particles. On the Pt₅₅ cluster shown in Path B, the C-H bond activation steps that occur on the terrace sites of the (111) facets require the participation of coordinatively-unsaturated neighboring edge and corner Pt sites as C-H activation requires two metal atom centers. On the Pt₂₀₁

cluster shown in Path A, the reactions can all proceed solely on the more coordinatively-saturated terrace sites of the (111) surface.

The first step in the cycle involves the activation of one of the equatorial C-H bonds of cyclohexane at a Pt site to form bound cyclohexyl ($C_6H_{11}^*$) and atomic hydrogen (H^*) intermediates. The subsequent activation of the axial C-H bond of the cyclohexyl intermediate at C-2 occurs over an adjacent Pt site to form cyclohexene ($C_6H_{10}^*$) which binds to the Pt surface in a di- σ configuration and produces an additional H^* . The cyclohexene can either desorb into the gas phase or subsequently react via C-H activation at the C-3 site to form the 3-cyclohexenyl ($c-C_6H_9^*$) surface intermediate. The C-H bond of the $c-C_6H_9^*$ intermediate is subsequently activated to form 1,3-cyclohexadiene which can desorb or undergo further C-H activation to form the $C_6H_7^*$ benzyl intermediate. The benzyl intermediate can undergo one final C-H bond scission to form benzene which can desorb into the gas phase. The DFT-calculated energy diagram shown in [Figure 3](#) intuitively shows that all of these potential surface species are strongly bound to the 111 terraces of the clean Pt_{55} (shown in red) and that the barriers for the desorption of cyclohexene, cyclohexadiene and benzene on Pt_{55} are significantly higher than the barriers for C-H bond activation. The results, however, are different on the Pt_{201} cluster (shown in blue) as the barriers for desorption are now smaller than those for the activation of C-H activation over the dominant (111) surface planes. This indicates that the stepwise dehydrogenation of cyclohexane proceeds more readily on smaller Pt nano-particles than on the larger Pt particles, thus producing more benzene than it does on larger Pt nanoparticles.

In order to provide a more quantitative view of the size dependence of cyclohexane dehydrogenation, we calculated the barriers at all of the different surface sites (edges, corners, (111) terraces, (100) terraces) on both the Pt_{55} and the Pt_{201} particles to examine the differences that result from these two different size clusters. As an example, we examine all of the plausible elementary steps for surface cyclohexene during the stepwise dehydrogenation on different surface sites (including edges and corners) of (111) facet of Pt_{201} ([Fig. S8](#)) at both low and high surface coverages. The cyclohexene surface intermediate that forms can either desorb or undergo further dehydrogenation to form cyclohexadiene or benzene that can subsequently desorb. Thus the final product distribution critically depends on the partitioning between two competing processes: cyclohexene C-H bond activation and cyclohexene desorption. Assuming first-order kinetics, we calculated the activation barriers, the changes in entropy and the rates for desorption and dehydrogenation of the surface bound cyclohexene and compared the transient dynamics for desorption with the dynamics for dehydrogenation.

The activation energies, activation entropies as well as the reaction rates for the desorption and dehydrogenation of cyclohexene on all of the different sites at the (111) facets of Pt₂₀₁ are summarized in [Table S3](#). As might be expected, cyclohexene adsorbs more strongly while C-H bond activation is much more favorable on the coordinatively unsaturated corner and edge sites. The calculations were carried out at both low coverage (bare particle) as well as at high coverage (benzene covered) to appropriately model the surface environment. . At the higher benzene surface coverages, cyclohexene dehydrogenation becomes more difficult whereas cyclohexene desorption becomes easier than that at lower coverages. The increased C-H activation barriers and decreased barriers for desorption for cyclohexene are due to their weaker interactions with the metal surface that result from lateral repulsive interactions and metal atom sharing between surface species that occur at high coverages. Similar effects also enhance the rates of cyclohexadiene desorption over that of dehydrogenation at the higher coverages.

On bare Pt particles, the cyclohexene desorption rate is significantly lower than its C-H bond activation rate, which indicates most of the adsorbed cyclohexene will be further dehydrogenated at low coverage. The results from calculations carried out using the more realistic high surface coverage model, however, show that the cyclohexene desorption rate from the (111) sites is significantly greater than its dehydrogenation rate ($r_{\text{des}}/r_{\text{act}} > 10$), i.e. desorption is favored over dehydrogenation. On the other hand, if C-H activation occurs on the edges or corners, the cyclohexene desorption rate is comparable to or smaller than its dehydrogenation rate ([Fig. S8](#)). Similar computational analyses carried out on the (100) facets of the Pt cluster indicate that there are no surface site combinations that would favor cyclohexene desorption over cyclohexene C-H activation on this surface, regardless of the surface coverage. The results are consistent with previous experimental findings that indicate that cyclohexene dehydrogenation to form benzene occurs much more readily on Pt (100) than on Pt (111). (39)

In order to provide a more direct comparison with the experimental results we can calculate the selectivity, i.e. the rate of cyclohexene desorption versus the rate of cyclohexene dehydrogenation ($r_{\text{des}}/r_{\text{CH-act}}$), as a function of specific Pt particle size by multiplying the number average weights (n_i) for specific coordination sites (i.e. corner, edge, (111) terrace, (100) terrace) by their respective rates for desorption (r_i^{des}) and rates for C-H activation ($r_i^{\text{CH-act}}$) as shown in Eq. 11 for each particle size. (see [Tables S3 and S4](#))

$$\frac{r_{des}}{r_{CH-act}} = \frac{\sum_{i=1}^{N_{sites}} n_i r_i^{des}}{\sum_{i=1}^{N_{sites}} n_i r_i^{CH-act}} \quad (11)$$

$$\frac{r_{des}}{r_{CH-act}} = \frac{\sum_{i=1}^{N_{sites}} n_i r_i^{des}}{\sum_{i=1}^{N_{sites}} n_i r_i^{CH-act}}$$

This assumes that the intrinsic barriers or rates for desorption r_i^{des} and C-H activation r_i^{CH-act} do not change with particle size. As such, any changes that result are due to the differences in the relative distribution of different sites. The results depicted in [Figure 4](#) show a sharp increase in the proportion of the more coordinatively saturated (111) surface sites that favor desorption over dehydrogenation with Pt particle size when the average diameter is smaller than 4 nm. This increase, however, grows much more slowly and asymptotes out as the particle diameter increases beyond 4 nm. If we extrapolate the curve in [Figure 4](#) down to the size of the Pt₅₅ (~1.2 nm) and Pt₂₀₁ (~1.8 nm) clusters, the proportion of (111) facet sites which favor desorption is at least two times greater for the Pt₂₀₁ particle than the Pt₅₅ particle. As such the rates for desorption would be two times higher than the rates of C-H activation on the Pt₂₀₁ cluster over that on the Pt₅₅ cluster.

These results are consistent with the experimentally results reported in Figures 1 and 2 which show a significant increase in the selectivity to benzene over cyclohexene as the cluster size is reduced below 2 nm. Pt nanoparticles less than 2 nm are predominantly comprised of edge and corner sites which strongly bind surface intermediates and activate C-H bonds; as such they predominantly result in formation of cyclohexadiene and benzene. Pt particles that are larger than 2 nm are comprised of the more coordinatively-saturated (111) terrace sites which result in weak adsorption energies and high C-H activation barriers and favor the desorption of cyclohexene over C-H activation. The larger Pt particles are therefore much more selective to cyclohexene formation than the smaller particles.

The experimental and theoretical results reported herein show that the selectivities for conversion of cyclohexane to cyclohexene, cyclohexadiene and benzene are directly related to the size of the Pt clusters formed as a result of the specific synthesis. The untreated Pt-MWNT catalysts were comprised of larger particles which showed higher selectivities to cyclohexene whereas the nitric acid treated and high temperature annealed sample (Pt-MWNT-HNO-hT) resulted in smaller particles and thus higher

selectivities to benzene. More generally the results indicate that different syntheses can be used to functionalization different carbon substrates and engineer the defect site density in order to strongly anchor and control the size of the supported metal nanoparticles and thus tune and control catalytic activity as well as the catalytic selectivity.

Acknowledgments.

The work at Yale University and the University of Virginia was supported by the AFOSR MURI grant FA9550-08-0309. The work at the Argonne National Laboratory was supported by the US Department of Energy, Materials Sciences and BES-Scientific User Facilities under Contract DE-AC-02- 06CH11357 with UChicago Argonne, LLC, Operator of Argonne National Laboratory. The computational research was performed using Environmental Molecular Science Laboratory, a national scientific user facility sponsored by the Department of Energy's Office of Biological and Environmental Research and located at Pacific Northwest National Laboratory. The authors thank Donald Graczyk for performing the quantitative analysis of the metal loading of the samples.

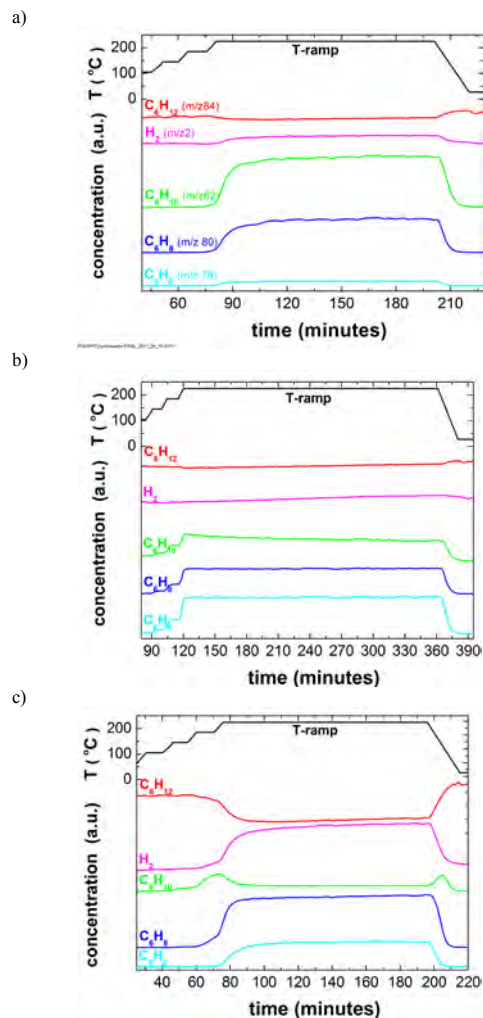


Figure 1. Temperature programmed reaction results for the dehydrogenation of cyclohexane (C_6H_{12} , $m/z=84$) on Pt-MWNT (a), Pt-MWNT-HNO (b) and Pt-MWNT-HNO-hT sample (c) using 4000 ppm cyclohexane (C_6H_{12} , $m/z=84$), seeded in He. Main products identified were cyclohexene (C_6H_{10} , $m/z=82$), cyclohexadiene (C_6H_8 , $m/z=80$) benzene (C_6H_6 , $m/z=78$) and hydrogen (H_2 , $m/z=2$). Concentrations were monitored as a function of temperature using a mass spectrometer. The ion signals of the products were scaled and offset for better viewing. The upper panel shows the applied

temperature as function of time.

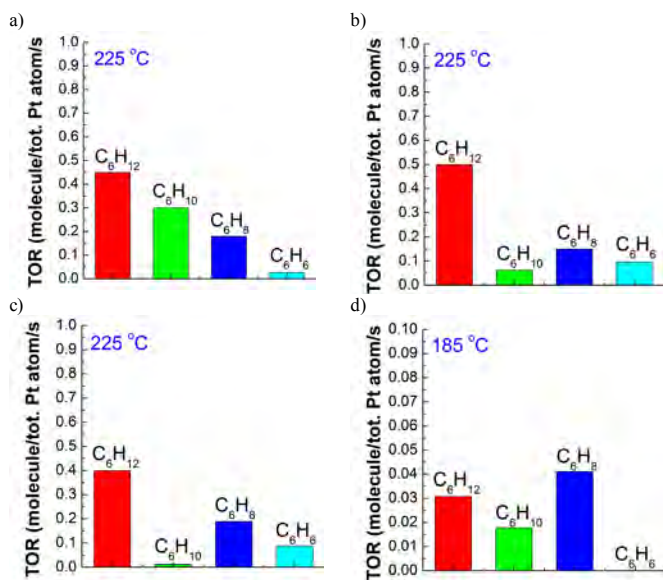


Figure 2. Turnover rates (TOR) per total Pt atom histograms of the reactant cyclohexane (C_6H_{12}) and carbonaceous products cyclohexene (C_6H_{10}), cyclohexadiene (C_6H_8) and benzene (C_6H_6) on Pt-MWNT (a), Pt-MWNT-HNO (b) and Pt-MWNT-HNO-hT sample (c) at 225 °C and TOR histogram of the reactant and products for the Pt-MWNT-HNO-hT sample at 185 °C (d). Note the different scale in (d), chosen for better visibility. See [Table S1](#) for more details.

Formatted Table

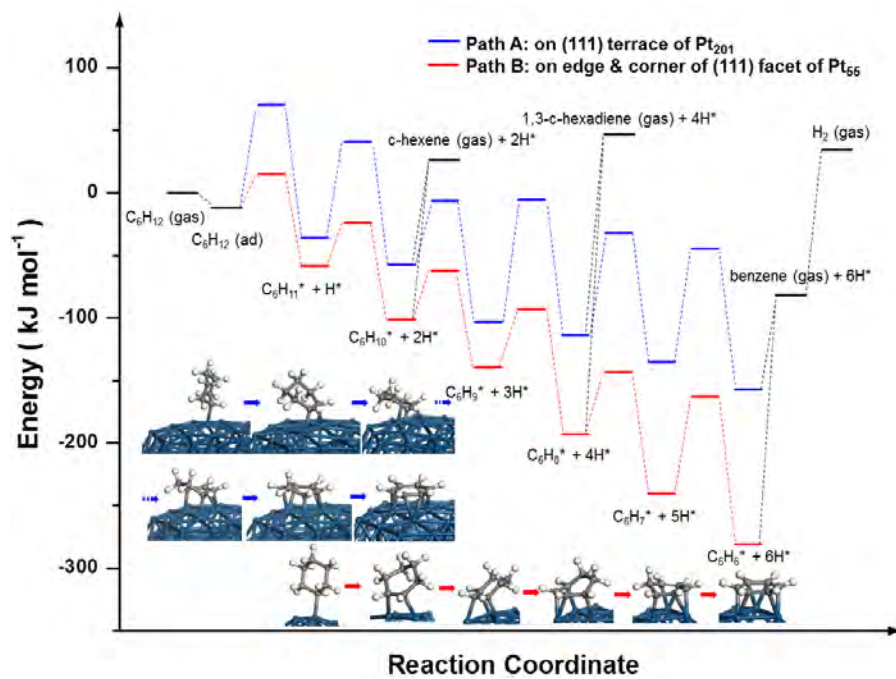


Figure 3. DFT calculated potential energy diagram for plausible reaction pathways of cyclohexane stepwise dehydrogenation to benzene on the bare 55 and 201 atom Pt clusters (Pt₅₅ and Pt₂₀₁). In Path A, all the reaction energies were calculated on the (111) terraces of Pt₂₀₁. In Path B, all of the energies are based on the center, edge and corner sites of (111)-like facet of the Pt₅₅ cluster. (zero energy reference for both clusters refer to the free-standing gas-phase cyclohexane and the bare Pt cluster). The adsorption energy of hydrogen atom was calculated to be 384.3 kJ mol⁻¹ on the Pt₂₀₁ cluster and used in all of the reaction energy calculations included.

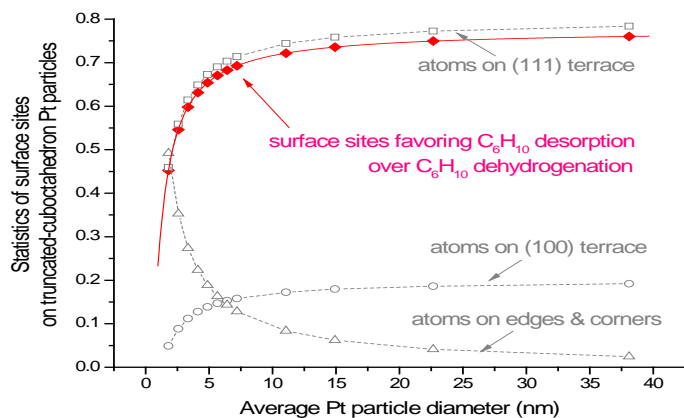


Figure 4. The fraction of surface sites that favor desorption over dehydrogenation of cyclohexene on different sizes of truncated cubo-octahedral Pt particles (red full circles). Grey curves indicate the fraction of surfaces atoms with different coordination numbers. Note the dramatic difference in the ratio between the faction of terrace vs edge and coner atoms in the size range of 1 and 2.5 nm investigated in this study.

References

1. D. T. Wickham, J. R. Engel, B. D. Hitch, M. E. Karpuk, Initiators for endothermic fuels. *Journal of Propulsion and Power* **17**, 1253 (Nov-Dec, 2001).
2. X. H. Peng, J. Y. Chen, J. A. Misewich, S. S. Wong, Carbon nanotube-nanocrystal heterostructures. *Chemical Society Reviews* **38**, 1076 (2009).
3. R. Narayanan, M. A. El-Sayed, Shape-Dependent Catalytic Activity of Platinum Nanoparticles in Colloidal Solution. *Nano Letters* **4**, 1343 (2004/07/01, 2004).
4. F. Maillard *et al.*, Size effects on reactivity of Pt nanoparticles in CO monolayer oxidation: The role of surface mobility. *Faraday Discussions* **125**, 357 (2004).
5. W. G. Dukek, Ed., *Kirk-Othmer Encyclopedia of Chemical Technology*, (Wiley, New York, 1991).
6. M. C. Yang, K. C. Chou, G. A. Somorjai, The structures and reactions of linear and cyclic C-6 hydrocarbons adsorbed on the Pt(111) crystal surface by sum frequency generation vibrational spectroscopy pressure, temperature, and H-2 coadsorption effects. *Journal of Physical Chemistry B* **108**, 14766 (Sep, 2004).
7. D. W. Blakely, G. A. Somorjai, Dehydrogenation and Hydrogenolysis of Cyclohexane and Cyclohexene on Stepped (High Miller Index) Platinum Surfaces. *Journal of Catalysis* **42**, 181 (1976).
8. M. Che, C. O. Bennett, The Influence of Particle-Size on the Catalytic Properties of Supported Metals. *Advances in Catalysis* **36**, 55 (1989).
9. R. M. Rioux, B. B. Hsu, M. E. Grass, H. Song, G. A. Somorjai, Influence of Particle Size on Reaction Selectivity in Cyclohexene Hydrogenation and Dehydrogenation over Silica-Supported Monodisperse Pt Particles. *Catalysis Letters* **126**, 10 (2008).
10. S. Vajda *et al.*, Subnanometre platinum clusters as highly active and selective catalysts for the oxidative dehydrogenation of propane. *Nature Materials* **8**, 213 (Mar, 2009).
11. X. Wang, N. Li, J. A. Webb, L. D. Pfefferle, G. L. Haller, Effect of surface oxygen containing groups on the catalytic activity of multi-walled carbon nanotube supported Pt catalyst *Applied Catal. B* **101**, 21 (2010, 2010).
12. X. Wang, N. Li, L. D. Pfefferle, G. L. Haller, Metal nanoparticles inside multi-walled carbon nanotubes: A simple method of preparation and of microscopic image analysis *Microporous and Mesoporous Materials* **176**, 139 (2013).
13. G. Y. Gao *et al.*, Simple synthesis of Pt nanoparticles on noncovalent functional MWNT surfaces: Application in ethanol electrocatalysis. *Journal of Power Sources* **173**, 178 (Nov, 2007).
14. Y. Y. Shao, G. P. Yin, H. H. Wang, Y. Z. Gao, P. F. Shi, Multi-walled carbon nanotubes based Pt electrodes prepared with in situ ion exchange method for oxygen reduction. *Journal of Power Sources* **161**, 47 (Oct, 2006).
15. X. M. Wang, N. Li, L. D. Pfefferle, G. L. Haller, in *Symposium on Catalysis for Hydrogen Energy Production and Utilization*. (Elsevier Science Bv, Gyeongju, SOUTH KOREA, 2008), pp. 160-165.
16. R. M. J. Fiedorow, S. E. Wanke, Sintering of Supported Metal-Catalysts .1. Re-Dispersion of Supported Platinum in Oxygen. *Journal of Catalysis* **43**, 34 (1976).
17. T. Tanabe, Y. Nagai, K. Dohmae, H. Sobukawa, H. Shinjoh, Sintering and redispersion behavior of Pt on Pt/MgO. *Journal of Catalysis* **257**, 117 (Jul, 2008).
18. S. Vajda *et al.*, Combined temperature-programmed reaction and in situ x-ray scattering studies of size-selected silver clusters under realistic reaction conditions in the epoxidation of propene. *Journal of Chemical Physics* **131**, 4 (Sep, 2009).

19. S. A. Wyrzgol *et al.*, Combined TPRx, in situ GISAXS and GIXAS studies of model semiconductor-supported platinum catalysts in the hydrogenation of ethene. *Physical Chemistry Chemical Physics* **12**, 5585 (2010).
20. S. Lee, B. Lee, S. Seifert, S. Vajda, R. E. Winans, Simultaneous measurement of X-ray small angle scattering, absorption and reactivity: A continuous flow catalysis reactor. *Nuclear Instruments and Methods in Physics Research Section A: Accelerators, Spectrometers, Detectors and Associated Equipment* **649**, 200 (2011).
21. N. Kariya *et al.*, Efficient hydrogen production using cyclohexane and decalin by pulse-spray mode reactor with Pt catalysts. *Applied Catalysis a-General* **247**, 247 (Jul, 2003).
22. M. A. Aramendia *et al.*, Dehydrogenation of cyclohexane over Pt/SiO₂-AlPO₄ catalysts .1. Influence of the catalyst particle size. *Reaction Kinetics and Catalysis Letters* **62**, 23 (Sep, 1997).
23. S. Hodoshima, H. Arai, Y. Saito, Liquid-film-type catalytic decalin dehydrogeno-aromatization for long-term storage and long-distance transportation of hydrogen. *International Journal of Hydrogen Energy* **28**, 197 (Feb, 2003).
24. Y. G. Wang, N. Shah, G. P. Huffman, Pure hydrogen production by partial dehydrogenation of cyclohexane and methylcyclohexane over nanotube-supported Pt and Pd catalysts. *Energy & Fuels* **18**, 1429 (Sep-Oct, 2004).
25. J. C. Hemminger, C. L. Pettiettehall, D. Parker, R. T. McIver, Surface Intermediates and Coverage Dependent Kinetics of the Dehydrogenation of Cyclohexane to Benzene on Pt(111). *Abstracts of Papers of the American Chemical Society* **201**, 215 (Apr, 1991).
26. J. P. Perdew, K. Burke, M. Ernzerhof, Generalized Gradient Approximation Made Simple. *Phys. Rev. Lett.* **77**, 3865 (1996).
27. J. P. Perdew, K. Burke, M. Ernzerhof, Erratum: Generalized Gradient Approximation Made Simple. *Phys. Rev. Lett.* **78**, 1396 (1997).
28. P. E. Blöchl, Projector augmented-wave method. *Phys. Rev. B* **50**, 17953 (1994).
29. G. Kresse, D. Joubert, From ultrasoft pseudopotentials to the projector augmented-wave method. *Phys. Rev. B* **59**, 1758 (1999).
30. G. Kresse, J. Hafner, Ab initio molecular dynamics for liquid metals. *Phys. Rev. B* **47**, 558 (1993).
31. G. Kresse, J. Hafner, Ab initio molecular-dynamics simulation of the liquid-metal-amorphous-semiconductor transition in germanium. *Phys. Rev. B* **49**, 14251 (1994).
32. G. Kresse, J. Furthmüller, Efficiency of ab-initio total energy calculations for metals and semiconductors using a plane-wave basis set. *Comput. Mat. Sci.* **6**, 15 (1996).
33. G. Kresse, J. Furthmüller, Efficient iterative schemes for ab initio total-energy calculations using a plane-wave basis set. *Phys. Rev. B* **54**, 11169 (1996).
34. G. Henkelman, A. Arnaldsson, H. Jónsson, A fast and robust algorithm for Bader decomposition of charge density. *Computational Materials Science* **36**, 354 (2006).
35. X. Pan, X. Bao, The Effects of Confinement inside Carbon Nanotubes on Catalysis. *Accounts of Chemical Research* **44**, 553 (2011/08/16, 2011).
36. Z. Li, Z.-X. Chen, G.-J. Kang, X. He, Does confinement effect always enhance catalytic activity? A theoretical study of H₂ dissociation on CNT supported gold clusters. *Catalysis Today* **165**, 25 (2011).
37. D. H. Ess, R. J. Nielsen, W. A. Goddard Iii, R. A. Periana, Transition-State Charge Transfer Reveals Electrophilic, Ambiphilic, and Nucleophilic Carbon–Hydrogen Bond Activation. *Journal of the American Chemical Society* **131**, 11686 (2009/08/26, 2009).
38. U. Achatz *et al.*, Methane activation by platinum cluster ions in the gas phase: effects of cluster charge on the Pt₄ tetramer. *Chemical Physics Letters* **320**, 53 (2000).
39. M. C. Tsai, E. L. Muetterties, Coordination chemistry of benzene, toluene, cyclohexadienes, cyclohexene, and cyclohexane on platinum(100). *The Journal of Physical Chemistry* **86**, 5067 (1982).

Supporting Online Material for

Particle Size Dependent Control of Catalytic Selectivity in the Dehydrogenation of Cyclohexane over Stable Multiwall Nanotube Supported Pt Particles.

Marcel Di Vece^{1,€,@}, Qiang Qian^{2,€}, Sungsik Lee^{3,€}, Chunrong Yin^{4,€,#}, Xiaoming Wang^{1,€, &},
Byeongdu Lee³, Sönke Seifert³, Randall E. Winans³, Gary L. Haller¹, Lisa D. Pfefferle¹,
Matthew Neurock^{3,§}, and Stefan Vajda^{1,4,5*}

¹*Department of Chemical Engineering, School of Engineering & Applied Science,
Yale University, Hillhouse Avenue, New Haven, CT 06520, USA*

²*Department of Chemical Engineering, University of Virginia,
102 Engineers' Way,
Charlottesville, VA 22904, USA*

³*X-Ray Sciences Division, Argonne National Laboratory,
9700 South Cass Avenue,
Argonne, IL 60439, USA*

⁴*Materials Science Division, Argonne National Laboratory,
9700 South Cass Avenue,
Argonne, IL 60439, USA*

⁵*Nanoscience and Technology Division, Argonne National Laboratory,
9700 South Cass Avenue, Argonne, IL 60439, USA*

€ Equally contributing (first) authors

@ Present address: Faculty of Science, Debye Institute for Nanomaterials Science Utrecht University, P.O. Box 80.000, NL-3508 TA Utrecht, The Netherlands

& Present address (XW): BASF Corporation, 25 Middlesex/Essex Turnpike, Iselin, NJ 08830, USA

Present address: Department of Chemical Engineering, Carnegie Mellon University, 5000 Forbes Avenue Pittsburgh, PA 15213, USA

§ Corresponding author: mn4n@virginia.edu (MN)

*Also corresponding author: vajda@anl.gov (SV)

This PDF file includes:

Materials and Methods

Figures S1 to S8

Tables S1 to S4

References

Material and Methods

Pretreatment of multi-walled carbon nanotube (MWNT) and Pt particle decoration

The MWNT (10-20 nm outer diameter, and >95% purity, as provided by the vendor) used were purchased from Cheap Tubes Inc. In order to functionalize the surface, the MWNT were refluxed in concentrated nitric acid (69 wt%, from J. T. Baker) at the boiling point for four hours. A fraction of the MWNTs was then further annealed in a He atmosphere at 1000 °C to remove most of the oxygen containing groups. The Pt particle decorated MWNTs were prepared by incipient wetness impregnation of a Pt precursor. Tetra-amine platinum(II) nitrate (from Sigma-Aldrich) was dissolved in water and then added to the MWNT supports dropwise until incipient wetness, and then dried at 60 °C overnight. The catalysts obtained on untreated MWNTs, nitric acid-treated and annealed MWNTs were labeled as Pt-MWNT, Pt-MWNT-HNO and Pt-MWNT-HNO-hT, respectively. In all these catalysts, the Pt loading was 8 wt%. The samples were characterized with various techniques such as transmission electron microscopy (TEM), X-ray absorption (near edge X-Ray absorption fine structure - NEXAFS, extended X-ray absorption fine structure - EXAFS) and nitrogen physisorption to measure the size, dispersion and oxidation state of the Pt particles as described in detail in Wang et al. ([1](#))

The combined TPRx/GISAXS/GIXAS experiments

For the combined TPRx/GISAXS/GIXAS experiments, the catalyst samples were dispersed in ethanol and subsequently sonicated to enhance solubility. The solution was drop casted on 15x18 mm² silicon wafers precoated with an ultrananocrystalline diamond film (UNCD, ADT 25 DoSi Aqua), after which the solvent evaporated in the ambient. The UNCD coated chips were chosen with the goal to provide an inert carbon-based support.

The TPRx/GISAXS/GIXAS experiments were performed at the 12-ID-C of the advanced Photon Source, in an in house built reaction cell equipped with Kapton windows to facilitate X-ray transmission. The cell was mounted on a computer controlled goniometer. The X-ray beam was scattered off the surface of the sample at near the critical angle ($\alpha_c = 0.15$) of the substrate. A 1024x1024 pixel two-dimensional MarCCD detector was used for recording the GISAXS images from the sample. The two-dimensional X-ray images

were analyzed by taking cuts in the q_{xy} direction for horizontal information. Scattering vectors q are calculated from $(4\pi/\lambda) \sin\theta$ where θ is the scattering half angle and λ is the wavelength of the X-rays (2-5) GIXAS spectra were detected in fluorescence mode, using a four-element Vortex detector.

For background correction of the X-ray and TPRx data, “blank” samples, i.e. on UNCD chip dispersed MWNTs of all three types (untreated, HNO and HNO-hT) without the added platinum were measured as well.

Catalytic reactions

The reaction cell was first evacuated to about 10^{-1} mbar, after which cyclohexane at a concentration of 4000 ppm in helium was introduced at a flow of 30 sccm and 1200 mbar pressure for the entire experiment. The temperature of the catalyst was controlled using a ceramic heater (Momentum Performance Materials Inc.) allowing heating of samples up to 600 °C. The sample temperature was measured with a K-type thermocouple attached to the edge of the heater surface. After 15 minutes of the gas inlet, the temperature of the sample was ramped in steps of 40 °C with 15 min intervals from room temperature to 225 °C. After several hours of reaction at 225 °C, the temperature was continuously decreased to room temperature in 20 minutes. To monitor product formation and the depletion of reactants, a mass spectrum was recorded every 52 seconds, which enabled monitoring of the evolution of cyclohexane, cyclohexene, cyclohexadiene, benzene and hydrogen as a function of temperature and time. The products were analyzed using a differentially pumped mass-spectrometer (Pfeiffer Vacuum Prisma Plus QMS 200). For quantitative analysis and calculation of turn-over-rates (TOR), the measured mass peak intensities of the products and reactants were first translated into concentration using calibrated gas mixtures (Air Gas), then the turn-over rates calculated based on Pt loading and gas flow parameters. In order to determine the Pt loading, the Pt nanoparticles on MWNTs were dissolved in HCl-HNO₃ at 140° C overnight. The solution was then analyzed with an inductively coupled plasma optical emission spectrometer (ICP-OES), which provides the exact amount of metal loading.

Monitoring the Size and Shape of Platinum particles

In situ GISAXS (6) was used to monitor the size and shape of the catalyst during the course of the reaction using X-rays of 11.619 keV energy; GIXANES to monitor the oxidation state of platinum. The GISAXS

images were recorded in 10 minute intervals. GIXANES spectra collected at each temperature. With the goal to eliminate the strong surface scattering arising from the UNCD support and to improve the determination of Pt particle sizes, transmission small angle X-ray scattering (SAXS) was performed at the 12-ID-B beamline of the Advanced Photon Source, on the MWNT-supported Pt catalysts, using photons with 17.9 keV energy. The samples were loaded into a quartz capillary with ends plugged with quartz wool. The capillary was mounted in a flow cell/furnace unit under helium flow. SAXS data were taken at room temperature and after heating the samples to 225 °C for 20 minutes.

To determine the sintering-resistance of the Pt nanoparticles and to investigate the effect of the cyclohexane dehydrogenation reaction on morphology of the Pt nanoparticle-MWNT composites, GISAXS images were recorded during the course of the reaction. In [Figure S1a](#) a typical GISAXS image of the Pt-MWNT sample is shown. The clear intensity changes and high count are evidence of a large amount of scatterers, i.e. MWNT and Pt. In [Figure S1b](#), a horizontal cut of [Figure S1a](#) was taken from the two-dimensional images of a blank MWNT sample and the Pt-MWNT sample, showing a clear difference around 0.06 \AA^{-1} indicating the presence of different size scatters. The size corresponding to the knee in [Figure S1b](#) of pure MWNT is $10.2 \pm 1.0 \text{ nm}$, while the size for Pt-MWNT, Pt-MWNT-HNO (not shown) and Pt-MWNT-HNO-hT is $11.0 (\pm 1.0) \text{ nm}$, $11.8 (\pm 1.0)$ and $11.9 (\pm 1.0)$ respectively. The latter diameter originates from the decoration of MWNT with Pt particles, which extend the diameter slightly as compared to pure MWNT. [Figure S1c](#) shows particle size distribution obtained from transmission SAXS on the Pt-MWNT sample, corrected for the scattering of the blank MWNT support. The obtained Pt cluster size of $2.1 \pm 0.7 \text{ nm}$ is an excellent agreement with the particle size obtained for this sample by EXAFS and TEM, $2.2 \text{ nm} \pm 1.2 \text{ nm}$ and $2.3 \text{ nm} \pm 1.4 \text{ nm}$, respectively. (1) During reactions up to 225 °C, no sintering of Pt particles or change of the size of the support was observed by GISAXS, nor by SAXS when heated under He. (A set of SAXS data obtained for the samples is shown in [Figure S2](#).) This points to the high stability of both the Pt particles and the used MWNT supports under applied conditions.

In [Figure S3](#) the GIXANES (Pt L3 edge) spectra recorded at room temperature before the reaction of the Pt-MWNT and Pt-MWNT-HNO-hT are shown. The spectra are background corrected and normalized, corresponding well to metallic Pt (7). It is clear that the spectra are overlapping and no difference both in the white line and absorption edge is present. Analysis of GIXANES spectra during the reactions (not

shown) revealed no changes, i.e. oxidation or carbide formation during the reaction is absent. This, along with the stable reaction rate over the duration of the experiment points to the high stability and poisoning-resistance of the investigated MWNT-supported Pt nanocatalysts.

Computational methods

All of theoretical calculations were carried out using periodic density functional theory (DFT) methods implemented in the Vienna *ab initio* Simulation Package (VASP). (8-11) The generalized gradient approximation (GGA), in the form of Perdew-Burke-Ernzerhof (PBE) (12, 13) was used to model exchange and correlation corrections. The interactions between the valence electrons and the core were described with the projector augmented wave method (PAW) (14, 15). The kinetic-energy cutoff for plane wave basis set was set at 400 eV, which was sufficient to obtain well-converged energies. The Brillouin zone sampling was restricted to the Γ -point. All of the structures were optimized until the displacement forces on every atom in the unit cell were converged to within 0.05 eV/Å. Eight to sixteen images were used to interpolate between reactants and products to establish the minimum energy reaction pathway (MEP). All of these images along the reaction coordinate were optimized via nudged elastic band (NEB) (16) algorithm until the tangential and normal forces on all of the atoms were converged to less than 0.2 eV/Å. The results from the NEB simulations were used to define an initial guess of the transition state for the Dimer (17) method. The dimer method was subsequently used to walk the initial dimer transition state complex up along the reaction coordinate in order to converge the transition state structure to a point where the forces on each of the atoms are converged to within 0.05 eV/Å.

The binding energy of adsorbate A on the platinum cluster was determined by equation (1).

$$E_{\text{ads}}(A) = E(A^*) - E(\text{bare cluster}) - E(A, \text{gas phase}) \quad (1)$$

where $E(A^*)$, $E(\text{bare cluster})$ and $E(A, \text{gas phase})$ refer to the total energies of A adsorbed onto the Pt surface, the bare Pt cluster, and the gas phase A species.

The reaction energy for each of the dehydrogenation steps take on the form of $A^* \rightarrow B^* + H^*$ and were calculated as:

$$E_{\text{rxn}}(A \rightarrow B) = E(B^*) + E_{\text{ads}}(H) - E(A^*) \quad (2)$$

where $E(B^*)$, $E(A^*)$ and $E_{\text{ads}}(\text{H})$ refer to the binding energy of A, binding energy of B, and the binding energy of atomic hydrogen on the Pt cluster.

Platinum Cluster Models

A cuboctahedral 55 atom Pt cluster (Pt_{55}) was used to model the ~ 1.2 nm platinum nano-particles. Larger platinum particles with diameter around 1.8 nm were modeled by a truncated cubo-octahedral 201 Pt cluster (Pt_{201}). [Figure S4](#) shows the optimized structures for these two Pt clusters. The number of different surface atom sites and their probabilities for the Pt_{55} and Pt_{201} clusters are summarized in [Table S2](#). It is worth noting that on the Pt_{55} cluster all the atoms of the (111)-like facet are actually edge or corner sites with lower coordination numbers than on actual extended (111) surfaces, and only the center atom of the (100)-like facet has the same coordination number with (100) single crystal surface. This is the result of the finite size of the small Pt_{55} cluster. The geometries of the Pt clusters were optimized with all the atoms fully relaxed. In the calculations of adsorption energies, only the top two layers of the cluster were relaxed, the Pt atoms in the layers below the top two were held fixed to their initially optimized distances. The Pt_{55} and Pt_{201} clusters were oriented within the unit cell such that facet of interest was perpendicular to the z-axis; the size of unit cells for the Pt_{55} and Pt_{201} clusters were $22 \times 22 \times 22 \text{ \AA}^3$ and $28 \times 28 \times 28 \text{ \AA}^3$, respectively. Several tests confirmed the unit cells were large enough to obtain energies that did not change to within 0.001 eV with changes in cell size.

The bare particle models, which represent low coverage case, may not appropriately describe the real catalytic environment, where the surfaces are likely covered by co-adsorbed hydrocarbon intermediates and hydrogen. Without loss of generality, we mimic the local high coverage of co-adsorbed hydrocarbon species on Pt_{201} by surrounding one adsorbed C6 molecule with six co-adsorbed benzene species, which results in a surface coverage of about one C6 molecule per four Pt atoms, beyond which multilayer adsorption is observed in experiments ([18](#)). (see [Figure S5](#))

Computational Kinetic Model: Assumptions and Justifications

We assume at the reaction temperature of 225 °C, cyclohexane stepwise dehydrogenation is almost irreversible. This assumption is supported by previous studies using sum frequency generation (SFG)

vibrational spectroscopy under actual high-pressure reaction conditions, which show that on both of Pt(111) and Pt(100) cyclohexene tend to dehydrogenate at a higher temperature of about 200 °C, whereas hydrogenation of cyclohexene is favored at a lower temperature of about 127 °C. (19)

By assuming first-order kinetics, the desorption reaction rate of cyclohexene is

$$r_{des} = k_{des} [C_6H_{10}^*],$$

where k_{des} is the rate constant and $[C_6H_{10}^*]$ is the surface concentration of cyclohexene. We assume that the unimolecular dehydrogenation of cyclohexene is pseudo-first-order with respect to the surface concentration of cyclohexene and zero-order in the concentration of available free sites. This assumption is supported by previous experimental observations. Thermal desorption spectra indicate hydrogen is readily desorbed from Pt(111) surfaces below 127 °C. (20) With hydrogen absent in the reactant gases at the temperature of 225 °C, the surface is predominantly covered by hydrocarbon intermediates with little hydrogen. Due to facile diffusion in the adlayer, once that hydrogen adatoms are formed on the Pt surface, they rapidly find one another and associatively desorb as H₂ before hydrocarbons leave the surface. Therefore only a very few free Pt sites need to be present in the adlayer to allow for dehydrogenation. (21-23) Hence, the reaction rate equation for dehydrogenation of cyclohexene is

$$r_{act} = k_{act} [C_6H_{10}^*],$$

According to transition state theory, the reaction rate constant is

$$k_i = \nu_i e^{-\frac{\Delta E_i}{k_B T}},$$

where ΔE is the energy difference between transition state and initial state (or the desorption energy in the expression of desorption rate constant), ν is the Arrhenius pre-exponential factor for the elementary step. Using Vineyard's formula (24, 25) the pre-exponential factor for cyclohexene dehydrogenation on (111) terrace of bare Pt₂₀₁ cluster was calculated to be $2.7 \times 10^{13} \text{ s}^{-1}$, which is in good accordance with the typical pre-exponential factor ($10^{13} \text{ s}^{-1} = k_B T/h$) for unimolecular surface decomposition (26). While the pre-exponential factor for desorption is usually on the order of 10^{15} s^{-1} . (18) The ratio between desorption reaction rate and dehydrogenation reaction rate can then be calculated as

$$\frac{r_{des}}{r_{act}} = \frac{\nu_{des}}{\nu_{act}} e^{-\frac{E_{des}-E_{act}}{k_B T}}.$$

Figures S1 to S8

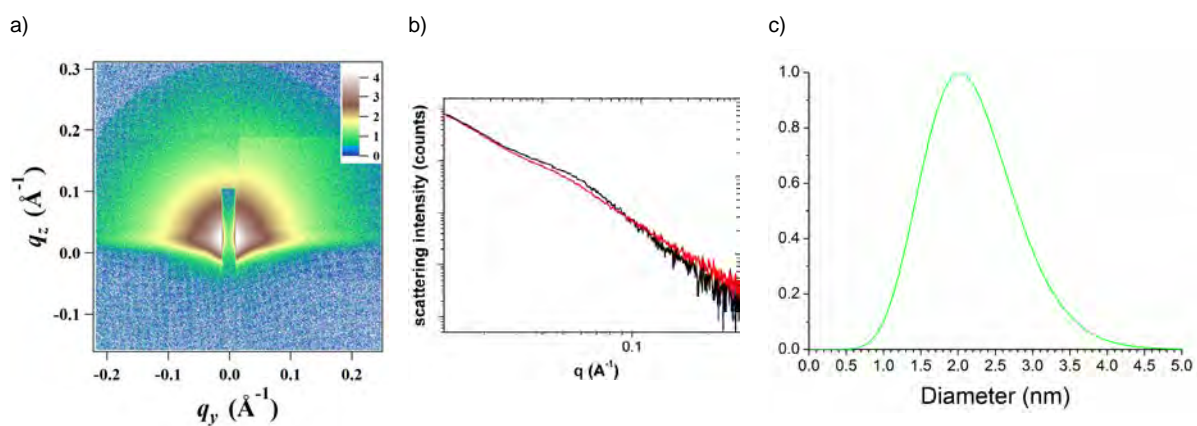


Figure S1. (a) Typical GISAXS pattern of Pt particles on MWNT at room temperature under 1 bar He with 4000 ppm cyclohexane. (b) GISAXS cut parallel to the surface for the blank MWNT (black line) and Pt-MWNT (red line) sample. (c) Pt particle size distribution obtained from the analysis of the SAXS scattering data. q denotes scattering vector.

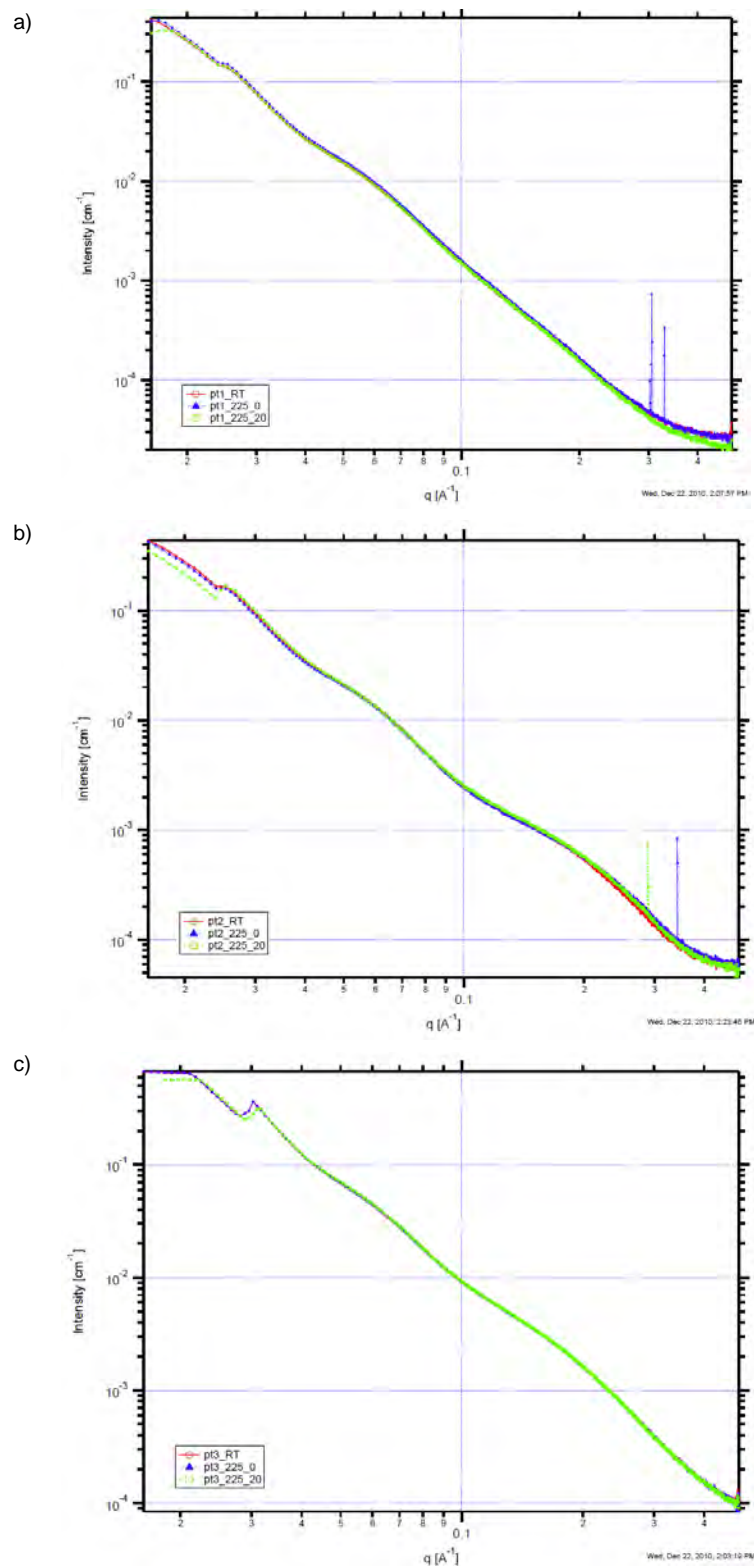


Figure S2. Cuts of transmission SAXS data collected on Pt-MWNT (a), Pt-MWNT-HNO (b) and Pt-MWNT-HNO-hT sample (c) under 4000 ppm cyclohexane, seeded in He, at three temperatures: at 20 °C (RT, red circles), 225 °C (225_0, blue triangles) and at 20 °C after cooling back from 225 °C (225_20, green squares). The identical patterns for the individual sample confirm sintering resistant particles.

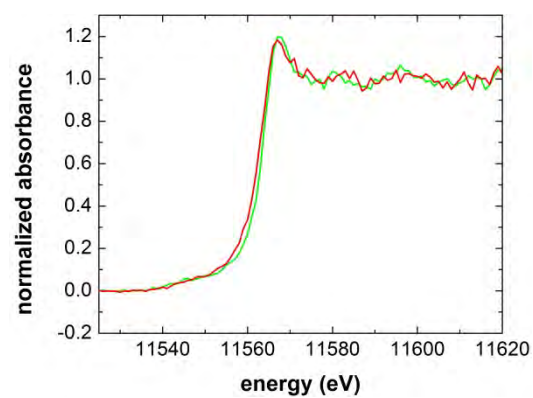


Figure S3. GIXANES (Pt L3 edge) spectra recorded at room temperature before the reaction of the Pt-MWNT (green) and Pt-MWNT-HNO-hT (red). The spectra are background corrected and normalized.

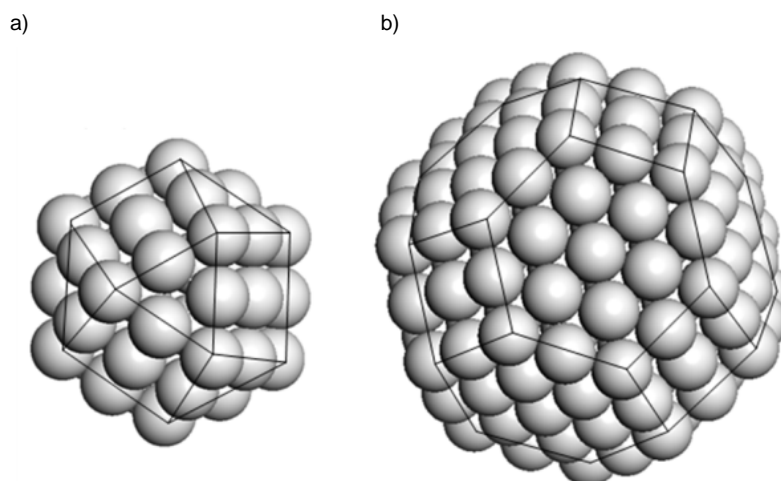


Figure S4. DFT-optimized structures of: (a) the cubo-octahedral Pt_{55} and (b) the truncated cubo-octahedral Pt_{201} clusters.

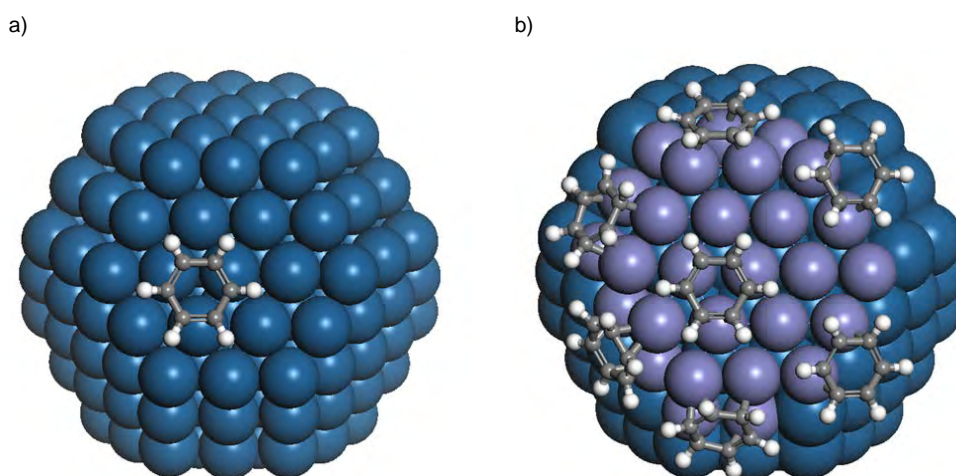
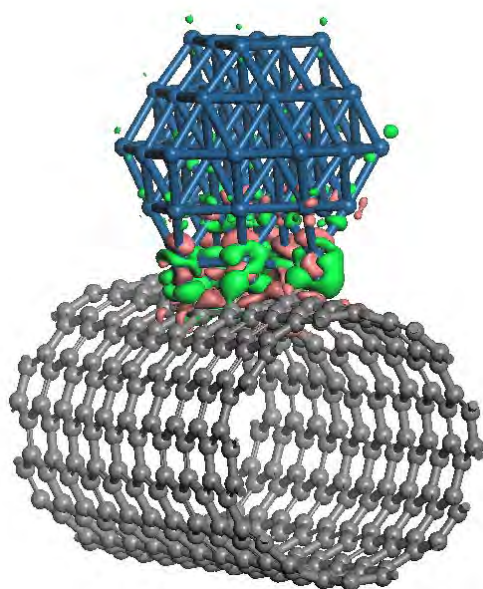


Figure S5. The low coverage model for the bare Pt_{201} particle (a) and high (local) coverage model of the benzene-covered Pt_{201} particle (b). (The local hydrocarbon covered surface Pt atoms are shown in purple). The coverage in this model is approximately 1 C6 molecule per 4 Pt atoms.

a)



b)

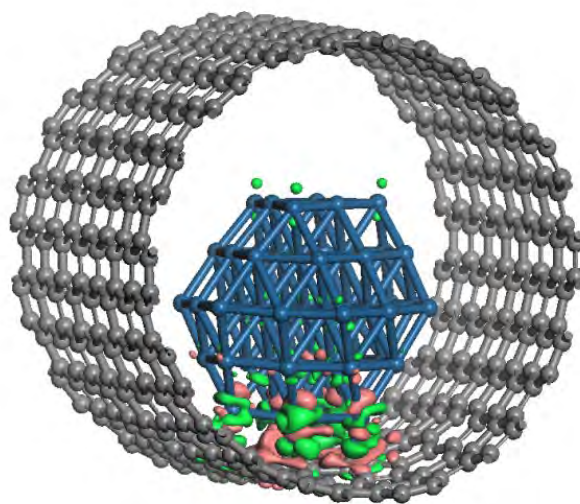
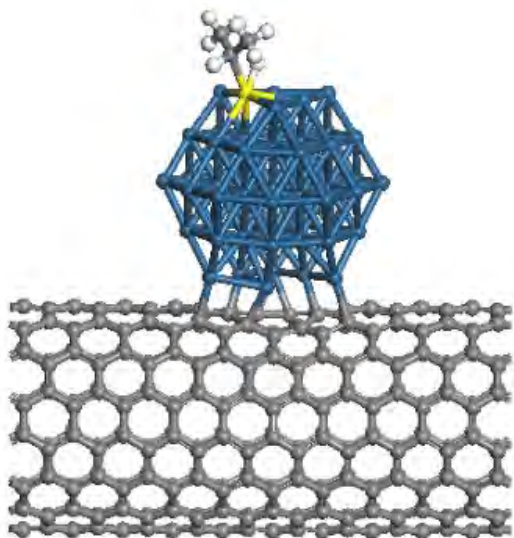
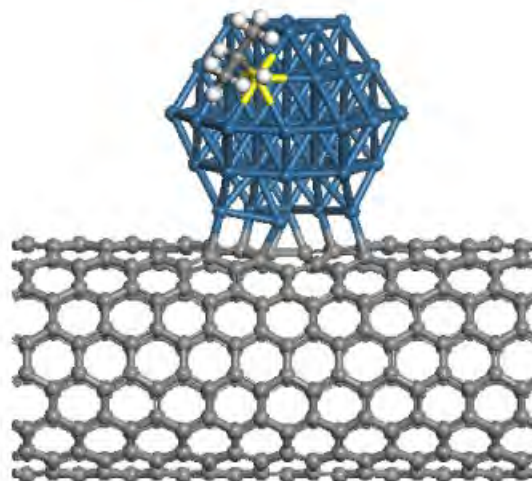


Figure S6. The charge density difference maps for the Pt₅₅ cluster bound: (a) outside of the (8,8) CNT with a carbon defect and (b) inside a (14,14) CNT with a carbon defect for isovalues of $\pm 0.02 e/\text{\AA}^3$. The green color denotes an accumulation of electron density whereas the red color denotes depletion of electron density, with respect to the free-standing Pt particle and CNT.

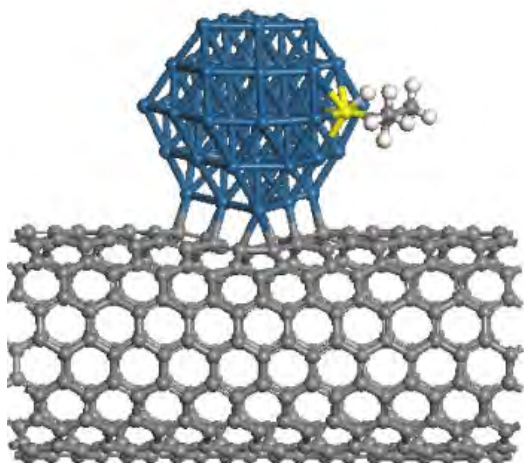
a)



b)



c)



d)

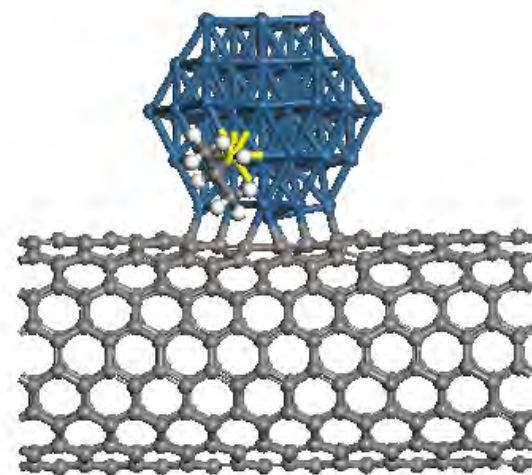


Figure S7. C-H bond activation of propane at different edge sites of Pt₅₅ supported on the outside wall of CNT(8,8) with defects. (a) edge site at Layer 1, $E_{\text{act}} = 33 \text{ kJ mol}^{-1}$; (b) edge site at Layer 2, $E_{\text{act}} = 29 \text{ kJ mol}^{-1}$; (c) edge site at Layer 3, $E_{\text{act}} = 31 \text{ kJ mol}^{-1}$; (d) edge site at Layer 4, $E_{\text{act}} = 40 \text{ kJ mol}^{-1}$. (The propane activation energy at an edge site of a free-standing Pt₅₅ cluster is 30 kJ mol^{-1} .)

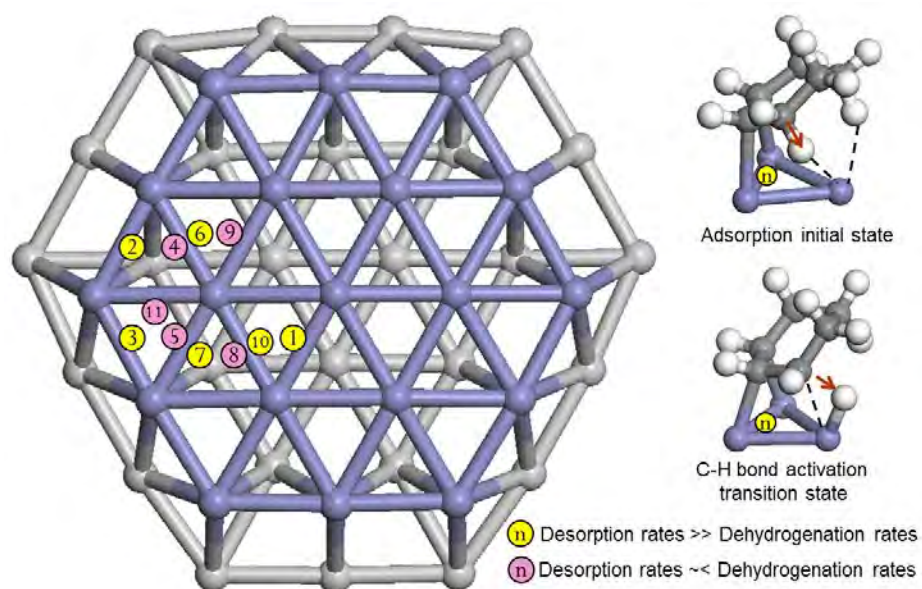


Figure S8. Surface site combinations for C-H bond activation of adsorbed cyclohexene: two Pt sites are involved in the di- σ adsorption configuration and one Pt site is involved in the C-H bond activation, which forms a triangle site combination. A site combination is denoted by circled number placed on the inner side of the Pt-Pt bridge involved in adsorption. With high surface coverage, cyclohexene desorption rate is much larger than its dehydrogenation rate when the C-H bond activation occurs on terrace sites (site combinations are numbered yellow circle). Otherwise, the site combinations are numbered in purple circle. (for details see [Table S3](#))

Table S1 to S4

Table S1 Turnover frequency (TOR) in cyclohexane molecules consumed per total and per surface Pt atom per second at 225 °C.

Sample	Reactant		
	C ₆ H ₁₂		
	Conversion	TOR	
	[%]	[molecules × Pt atoms ⁻¹ s ⁻¹]	
		^a Total Pt-atom based	^b Surface Pt-atom based
Pt-MWNT	0.07	0.45	1.72
Pt-MWNT-HNO	0.04	0.50	0.94
Pt-MWNT-HNO-hT	0.40	0.40	0.82

^a Turnover frequency (TOR) in cyclohexane molecules consumed per Pt atom per second at 225 °C, calculated on basis of the total Pt loading of the sample. The metal loading of the Pt-MWNT, Pt-MWNT-HNO and Pt-MWNT-HNO-hT samples was 6.98 μm, 3.28 μg and 43.5 μg, respectively, determined by inductively coupled plasma mass spectrum analysis (ICP-MS).

^b Turnover frequency (TOR) in cyclohexane molecules consumed per Pt atom per second at 225 °C, calculated on basis of the number of surface Pt atoms estimated for spherical Pt particles with average sizes reported by Wang et al as 2.3, 1.1, 1.2 nm for the Pt-MWNT, Pt-MWNT-HNO and Pt-MWNT-HNO-hT samples, respectively (1) and based on Pt-Pt distance of 0.392 nm. A subtraction of estimated number of for reactant molecules inaccessible Pt atoms located at the base of the Pt particle on the MWNT support was not performed.

Table S2. Summary of surface atoms on Pt₅₅ and Pt₂₀₁ clusters

Pt cluster	Number of surface atoms	corner		edge		(100)-like facet		(111)-like facet	
		count	%	count	%	count	%	count	%
Pt ₅₅	42	12	28.6	24	57.1	6	14.3	0	0.0
Pt ₂₀₁	122	24	19.7	36	29.5	6	4.9	56	45.9

Table S3. Energetics and reaction rates for desorption and dehydrogenation reactions of cyclohexene at various surface sites on (111) facet of Pt₂₀₁ particle (with low coverage and high coverage)

Pt ₂₀₁ particle (111) facet		Cyclohexene desorption energy E _{des} (kJ mol ⁻¹)		Cyclohexene C-H activation energy E _{act} (kJ mol ⁻¹)		Desorp. rate vs. dehydro. rate $r_{des}/r_{act}^{\ddagger}$	
surface sites*	site count	low coverage	high coverage †	low coverage	high coverage †	low coverage	high coverage
1 (TT-T)	12	83.6	54.1	64.0	69.4	0.899	3914.1
2 (EC-T)	6	107.9	82.9	69.7	79.4	0.010	43.0
3 (CE-T)	6	108.9	84.4	80.6	94.4	0.109	1092.0
4 (TE-C)	6	86.2	61.0	31.1	35.2	0.000	0.2
5 (ET-C)	6	75.3	52.2	35.6	39.3	0.007	4.5
6 (ET-T)	6	77.2	51.9	57.1	65.0	0.801	2338.7
7 (TE-T)	6	74.6	49.3	63.1	71.9	6.317	22818.0
8 (TT-E)	3	88.9	63.7	44.5	50.6	0.002	4.2
9 (TT-E)	3	84.0	58.8	38.4	43.6	0.002	2.6
10 (TT-T)	6	86.6	61.5	68.5	78.1	1.273	5401.1
11 (TC-E)	12	87.8	64.2	27.2	32.8	0.000	0.1

* surface sites see Figure S8. (XY-Z) denotes a surface sites combination containing two di-σ adsorption sites and one C-H activation site, which form a triangle. T - terrace site; E - edge site; C - corner site

† For the high coverage model (benzene covered particle), 4 adsorption sites were calculated (numbers in **bold** type), data for the rest adsorption sites (numbers in *Italian* type) were estimated by linear fitting to data obtained from low coverage model (bare particle).

‡ Prefactor for desorption = 10¹⁵ s⁻¹; prefactor for dehydrogenation = 10¹³ s⁻¹

Table S4. Statistics of surface sites for different sizes of truncated cubo-octahedral Pt particles

Truncated cubo-octahedron			surface sites favoring cyclohexene desorption on (111) facet	Total adsorption sites on (111) facet	Fraction of surface sites that favors cyclohexene desorption †
m value *	Average diameter (nm)	Particle size (atoms)	$18(m-2)^2 + 6(3m-5)$	$18(m-1)^2$	
3	1.80	201	42	72	0.453
4	2.57	586	114	162	0.546
5	3.34	1289	222	288	0.598
6	4.11	2406	366	450	0.631
7	4.88	4033	546	648	0.654
8	5.65	6266	762	882	0.670
9	6.43	9201	1014	1152	0.683
10	7.20	12934	1302	1458	0.693
15	11.06	46929	3282	3528	0.722
20	14.93	115274	6162	6498	0.736
30	22.65	403014	14622	15138	0.750
50	38.11	1918694	42342	43218	0.760

* m is the number of atoms lying on an equivalent edge (corner atoms included)

† fraction of surface sites favoring cyclohexene desorption over cyclohexene dehydrogenation on the whole cubo-octahedron particle including (111) facets and (100) facets; no site from (100) facets favors the desorption of cyclohexene. For cubo-octahedrons, the ratio of total surface area of (111) facets to (100) facets are $2\sqrt{3} : 1$, which was used in the calculations of this column.

References

1. X. Wang, N. Li, J. A. Webb, L. D. Pfefferle, G. L. Haller, Effect of surface oxygen containing groups on the catalytic activity of multi-walled carbon nanotube supported Pt catalyst *Applied Catal. B* **101**, 21 (2010).
2. B. Lee *et al.*, Anomalous grazing incidence small-angle x-ray scattering studies of platinum nanoparticles formed by cluster deposition. *Journal of Chemical Physics* **123**, 7 (Aug, 2005).
3. R. E. Winans *et al.*, Thermal stability of supported platinum clusters studied by in situ GISAXS. *Journal of Physical Chemistry B* **108**, 18105 (Nov, 2004).
4. S. A. Wyrzgol *et al.*, Combined TPRx, in situ GISAXS and GIXAS studies of model semiconductor-supported platinum catalysts in the hydrogenation of ethene. *Physical Chemistry Chemical Physics* **12**, 5585 (2010).
5. S. Lee, B. Lee, S. Seifert, S. Vajda, R. E. Winans, Simultaneous measurement of X-ray small angle scattering, absorption and reactivity: A continuous flow catalysis reactor. *Nuclear Instruments and Methods in Physics Research Section A: Accelerators, Spectrometers, Detectors and Associated Equipment* **649**, 200 (2011).
6. G. Renaud, R. Lazzari, F. Leroy, Probing surface and interface morphology with Grazing Incidence Small Angle X-Ray Scattering. *Surface Science Reports* **64**, 255 (Aug, 2009).
7. A. Jentys, B. J. McHugh, G. L. Haller, J. A. Lercher, Temperature-Programmed Reduction of Silica-Supported Pt/Ni Catalysts Studied by Xanes. *Journal of Physical Chemistry* **96**, 1324 (Feb, 1992).
8. G. Kresse, J. Hafner, Ab initio molecular dynamics for liquid metals. *Phys. Rev. B* **47**, 558 (1993).
9. G. Kresse, J. Hafner, Ab initio molecular-dynamics simulation of the liquid-metal-amorphous-semiconductor transition in germanium. *Phys. Rev. B* **49**, 14251 (1994).
10. G. Kresse, J. Furthmüller, Efficiency of ab-initio total energy calculations for metals and semiconductors using a plane-wave basis set. *Comput. Mat. Sci.* **6**, 15 (1996).
11. G. Kresse, J. Furthmüller, Efficient iterative schemes for ab initio total-energy calculations using a plane-wave basis set. *Phys. Rev. B* **54**, 11169 (1996).
12. J. P. Perdew, K. Burke, M. Ernzerhof, Generalized Gradient Approximation Made Simple. *Phys. Rev. Lett.* **77**, 3865 (1996).
13. J. P. Perdew, K. Burke, M. Ernzerhof, Erratum: Generalized Gradient Approximation Made Simple. *Phys. Rev. Lett.* **78**, 1396 (1997).
14. P. E. Blöchl, Projector augmented-wave method. *Phys. Rev. B* **50**, 17953 (1994).
15. G. Kresse, D. Joubert, From ultrasoft pseudopotentials to the projector augmented-wave method. *Phys. Rev. B* **59**, 1758 (1999).
16. H. Jónsson, G. Mills, K. W. Jacobsen, in *Classical and Quantum Dynamics in Condensed Phase Simulations*, B. J. Berne, G. Ciccotti, D. F. Coker, Eds. (World Scientific, 1998), pp. 385-404.
17. H. Graeme, J. Hannes, A dimer method for finding saddle points on high dimensional potential surfaces using only first derivatives. *The Journal of Chemical Physics* **111**, 7010 (1999).
18. O. Lytken *et al.*, Energetics of Cyclohexene Adsorption and Reaction on Pt(111) by Low-Temperature Microcalorimetry. *Journal of the American Chemical Society* **130**, 10247 (2008).
19. K. R. McCrea, G. A. Somorjai, SFG-surface vibrational spectroscopy studies of structure sensitivity and insensitivity in catalytic reactions: cyclohexene dehydrogenation and ethylene hydrogenation on Pt (1 1 1) and Pt (1 0 0) crystal surfaces. *Journal of Molecular Catalysis A: Chemical* **163**, 43 (2000).
20. B. Poelsema, K. Lenz, G. Comsa, The dissociative adsorption of hydrogen on Pt(111): Actuation and

- acceleration by atomic defects. *Journal of Chemical Physics* **134**, 074703 (2011).
21. M. B. Hugenschmidt, A. L. Diaz, C. T. Campbell, Interaction of cyclohexadiene with platinum(111) studied by BPTDS and HREELS. *The Journal of Physical Chemistry* **96**, 5974 (1992).
 22. J. M. Campbell, S. Seimanides, C. T. Campbell, Probing ensemble effects in surface reactions. 2. Benzene adsorption on clean and bismuth-covered platinum(111). *The Journal of Physical Chemistry* **93**, 815 (1989).
 23. C. T. Campbell *et al.*, Probing ensemble effects in surface reactions. 1. Site-size requirements for the dehydrogenation of cyclic hydrocarbons on platinum(111) revealed by bismuth site blocking. *The Journal of Physical Chemistry* **93**, 806 (1989).
 24. G. H. Vineyard, Frequency factors and isotope effects in solid state rate processes. *Journal of Physics and Chemistry of Solids* **3**, 121 (1957).
 25. C. Wert, C. Zener, Interstitial Atomic Diffusion Coefficients. *Physical Review* **76**, 1169 (1949).
 26. M. Boudart, G. Djega-Mariadassou, *Kinetics of Heterogeneous Catalytic Reactions*. (Princeton University Press, Princeton, NJ, 1984).